STM, LEED and Photoemission Studies of the Sn/Cu(100) Surface Alloys

A thesis Submitted to

Dublin City University

For the degree of

Master of Science

By

Rory Sweeney B.Sc.
School of Physical Sciences
Dublin City University

Research Supervisors:
Dr. A. A. Cafolla
Dr. E. McLoughlin

August 2009

Declaration

I hereby certify that this material, which I now submit for assessment on the programme of study leading to the award of Master of Science is entirely my own work, that I have exercised reasonable care to ensure that the work is original, and does not to the best of my knowledge breach any law of copyright, and has not been taken from the work of others save and to the extent that such work has been cited and acknowledged within the text of my work.

……

Rory Sweeney, August 2009

ID No.: 51337980

Acknowledgements

I am very grateful for having the opportunity to undertake this Masters research and I would like to acknowledge and thank all those who made this possible:

First and foremost I would like to thank my supervisors; Dr Tony Cafolla and Dr Eilish McLoughlin. Especially Dr. Cafolla without his constant assistance and guidance this research would never have been competed. I need to thank Prof. John Costello and the School of Physical Sciences in Dublin City University for their support. I wish to thank Dr Sergey Krasnikov for all the wonderful help at every step.

I have also to thank my friends in the office; Barry, Patrick and Stephen for their help and support and simply for making every day fun.

Finally special thanks must go to my parents, family and Maeve for all of their wonderful support the entire time.

Contents

List of Tables

List of Figures

Abstract

The primary focus of this thesis is the study of bimetallic ordered surface alloys. Cu-based bimetallic catalysts show very useful properties, particularly in respect to their industrial applications, such as metal selectivity, structural stability and catalytic activity in comparison to their single-metal counterparts. Since most microelectronic assemblies utilize Pb-Sn solders for interconnection and modern environmental regulations have targeted the elimination of Pb usage, this makes research for "Pb-free" solders an important issue for microelectronics assembly. Thus the Cu-Sn bimetallic system is a technologically important system which merits detailed investigation.

The Sn/Cu(100) surface system has five reported submonolayer surface phases. Four phases were originally reported by Argile and Rhead in the early 1980's and a fifth phase was reported by Martinez-Blanco *et al.* in 2006. This thesis has been motivated by this report of a new surface phase. The original four phases have already been studied using Low Energy Electron Diffraction (LEED) by McLoughlin *et al.* This thesis reviews these studies and completes them by analysing LEED images and integral order beam I(V) spectra obtained for the most recently reported phase.

The surface structures of all five phases are studied using Scanning Tunnelling Microscopy (STM) and surface structure models for all the phases are proposed. Photoemission Spectroscopy (PES) and High-Resolution Core-Level Spectroscopy (HRCLS) studies were carried out using synchrotron radiation in the Institute for Storage Ring Facilities in Aarhus (ISA). PES is used to measure changes in the work functions and valence band spectra while HRCLS is used to examine differences in the Cu 3p and Sn 4d core level spectra for all five phases.

Chapter 1: Introduction

Studies have shown the electronic structure of thin films grown on metal surfaces to be strongly influenced be the intermixing, alloying, dealloying and strain-induced reconstructing at the metal surface [Rodriguez 1996]. The ordering of alkali and transition metals on the copper surfaces has been extensively studied both experimentally and theoretically in recent years. This is due to the fact that Cu-based bimetallic catalysts show very useful properties, particularly in respect to their industrial applications, such as metal selectivity, structural stability and catalytic activity in comparison to their single-metal counterparts [Campbell 1990] [Somorjai 1996].

Since most microelectronic assemblies utilize Pb-Sn solders for interconnection and modern environmental regulations have targeted the elimination of Pb usage, this makes research for "Pb-free" solders an important issue for microelectronics assembly. Thus the Cu-Sn bimetallic system is a technologically important system which merits detailed investigation.

Two main structures for bimetallic alloy films have been reported: (i) a surface alloy with a mixed adsorbate/substrate top layer [1] and (ii) a top layer consisting of substrate atoms with the adsorbate atoms subsurface occupying the second layer [2]. Theoretical study has shown that surface alloy formation is generally expected in systems that are dominated by atomic size mismatch [3] [4]. Tersoff et al. [3] concluded that the ratio of the metallic radii of the adsorbate and substrate atoms can be used to predict surface alloy formation.

The following observations of the different behaviours of adsorbates grown on the Cu{100} surfaces are in good agreement with this conclusion. For elements with an atomic radii ratio < 1.25, there are two types of behaviour dependent on whether the element is miscible or immiscible in the bulk phase with copper. For immiscible elements such as Ni and Ir, alloy formation occurs at low coverages, < 1ML, with the adsorbate atoms located subsurface. For miscible elements Mn, Pd, Pt and Au, surface alloys form over a coverage range, 0 - 0.6ML. These alloy structures are based on a ratio of 1:2 adsorbate atoms to topmost layer atoms of the substrate. For elements, Ag, Li, In, Bi and Pb where the ratio of atomic radii is between 1.13 and 1.37 surface alloy structures form at coverages < 0.4ML. Increasing the coverage causes the adsorbate atoms to dealloy to form overlayer structures. The atomic radii ratio for Sn/Cu of 1.27 is

within this range. Finally for adsorbates with larger atomic radii ratios, > 1:37, for example Na and K, overlayer structures are reported for all coverages [5].

The large lattice mismatch between tin and copper contributes to a well defined complex series of ordered phases formed by the deposition of Sn on room temperature Cu(001). Previous low energy electron diffraction (LEED) [6] [7] [8] and He ion scattering studies (HAS) [9] of the Sn/Cu(100) system have identified five room temperature Sn surface structures. Four phases were originally reported by Argile and Rhead [6] in the early 1980's and a fifth phase was reported by Martinez-Blanco *et al.* [8] in 2006. These phases were observed for Sn coverage of Cu(100) between 0.2 ML and 0.7 ML. No ordered structures have been reported with Sn coverage in excess of 0.7 ML.

The primary focus of this thesis is the study of the Sn/Cu(100) bimetallic ordered surface structures. The original four phases have already been studied using Auger electron spectroscopy (AES) and low energy electron diffraction (LEED) by McLoughlin *et al.* [5]. This thesis reviews these studies and complements them by further analysis of LEED patterns and I(V) spectra

The development of the scanning tunnelling microscope (STM) has enabled the imaging and detailed study of surface on an atomic level. The five surface structure phases of the Sn/Cu(100) system are studied using STM and surface structure models for all the phases are proposed.

The results of photoemission spectroscopy (PES) and high-resolution core-level spectroscopy (HRCLS) studies, carried out using synchrotron radiation in the Institute for Storage Ring Facilities in Aarhus (ISA), are also reported. PES is used to measure changes in the work functions and valence band spectra while HRCLS is used to examine differences in the Cu 3p and Sn 4d core level spectra for all five phases.

The different experimental techniques used in this thesis along with their theoretical bases are presented in chapter 2. Specifically, low energy electron diffraction (LEED), scanning tunnelling microscopy (STM) and photoemission spectroscopy (PES) are discussed. The components and operating procedures including the ultra high vacuum (UHV) chambers are discussed. The synchrotron radiation used in the PES studies is introduced. Finally, software which aided the analysis of data detailed in the relevant section is described.

In chapter 3 the Sn/Cu(100) surface alloy is examined and five submonolayer surface structures are discussed. The relevant previous studies of each surface phase are

reviewed. Each phase is then studied using LEED patterns, I(V) LEED analysis and STM imaging. Using these results surface structure models for each phase are proposed.

In chapter 4 synchrotron radiation is used to examine the Cu 3p and Sn 4d core levels as a function of the different phases. Valence band spectra are taken for each phase.

Finally chapter 5 discusses the conclusions that emerged from these studies. Some suggestions as to the possible directions that future work could take are outlined.

Chapter 2: Theoretical Background/Experimental Techniques

2.1 Surface Sensitivity

The number of atoms in the surface layer of a typical solid is ~ 10^{15} cm^{-2} or 6 - 7 orders of magnitude lower than the total number of atoms in any macroscopic sample, any technique used in experimental surface science must be one that interacts strongly with the first few atomic layers only.

The surface sensitivity of an analytical technique depends on the depth of origin of the detected species within the material. An electron travelling through a solid will have a certain inelastic mean free path (IMFP), which is the average length that the electron can travel without an energy loss due to a collision.

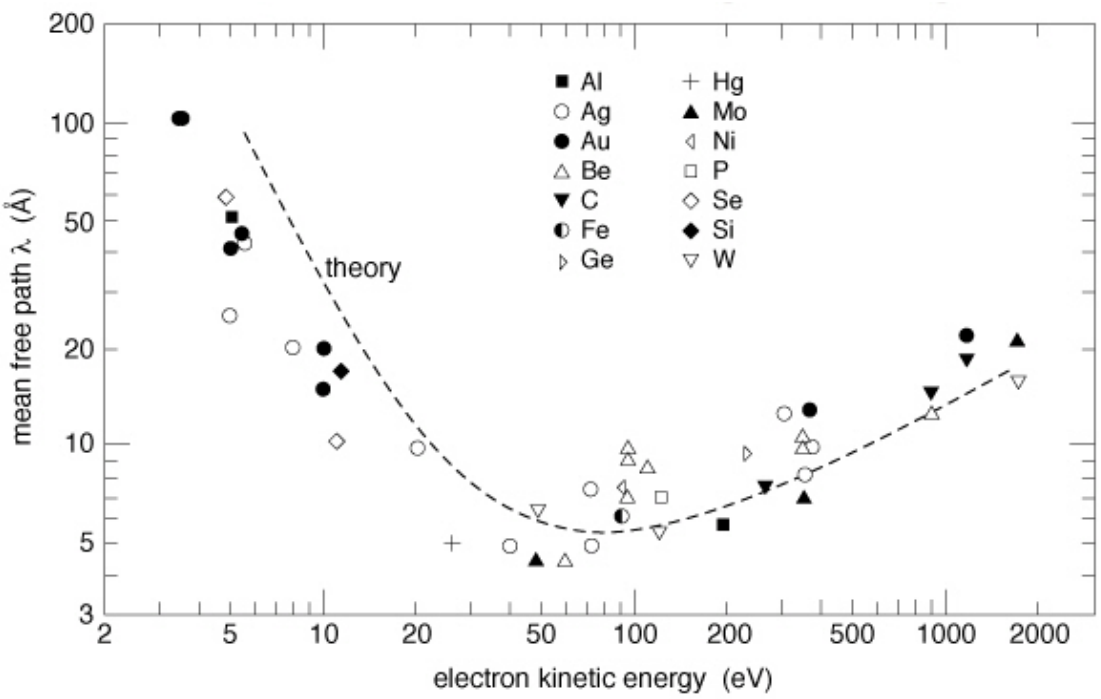

Figure 2.1: The Inelastic Mean Free Path (IMFP) of an electron propagating a solid.

Figure 2.1 shows the IMFP of an electron travelling through a solid as a function of its kinetic energy [10]. The dashed curve is a theoretical calculation of the IMFP independent of the material. The data points are measurements taken from specific solids. It can be seen that these data points all fall around the curve and therefore the IMFP is independent of the solid. The broad minimum of this curve shows the surface sensitivity of electrons. Electrons with energies in the range 30 – 300 eV have an IMFP

< 10Å. Electrons observed with kinetic energies in this range that have left the solid without suffering inelastic scattering have originated from the first few atomic layers and hence makes electron based analytical techniques highly surface sensitive. For example in Photoemission Spectroscopy (PES) photons which bombard the surface typically penetrate several microns into the solid, but the resultant unscattered electrons originate from within 1 – 8 nm of the surface or the first few atomic layers. Electrons generated deeper in the solid may escape but in propagating to the surface they will have collided with other atoms and will have lost energy through inelastic collisions. These electrons contribute a secondary electron background to the photoemission spectrum.

2.2 Low Energy Electron Diffraction (LEED)

Low energy electron diffraction (LEED) was first discovered by Davidson and Germer in 1927. They observed that electrons with energies between 15 and 200 eV incident on a nickel crystal resulted in variations in the angular distribution of the elastically backscattered electrons which were consistent with electron diffraction [11]. Since then the diffraction of electrons from a crystal surface is a standard method for determining the structure of crystal surfaces. The incident electron may have low energy ~10-500 eV and impinge at normal or close to normal incidence on a crystal (LEED) or high energy ~10-20 keV and impinge at grazing incidence (RHEED).

The wavelength, λ of the electron is related to its energy by

$$\lambda = \left(\frac{150.6}{E(eV)} \right) \text{Å} \qquad \textbf{2.1}$$

where E is the energy of the incident electron beam. Low energy electrons have wavelengths of approximately 0.1 - 0.01 nm, which are of the same order of magnitude as the inter-atomic spacing at the surface of a single crystal. The elastically scattered electrons produce a diffraction pattern, from which the two dimensional periodicity of the surface can be deduced. Nearly all of the elastic collisions that lead to diffraction peaks take place in the first or second atomic layers closest to the surface. For this reason LEED is a surface sensitive technique.

Variations in the unit cell dimensions induced by adsorption or reconstruction of the surface can also be observed in LEED. From the variations of the spot intensities

with beam energy the complete surface geometry can be determined, this technique is referred to as I(V)-LEED.

Any plane of atoms in a crystal structure can be defined by three coordinates called Miller indices, (h, k, l), which have a reciprocal relationship to the real intercepts of the plane with the axes of the crystal. Similarly the wavelength of light, a real space distance, also has a reciprocal relationship to the wavevector, k where ($k=2\pi/\lambda$). The wavevector is a measure of the momentum of the incident and diffracted beams of electrons.

2.2.1 Ewald Sphere Construction

The conditions for elastic scattering are shown with the construction of a Ewald Sphere. This is shown in reciprocal space for a cubic lattice in Figure 2.2(a), where the distance between adjacent lattice points is $2\pi/a$, where a is the distance between points in the real space lattice. A wavevector k_0 is drawn on the diagram with its tip pointing towards the origin of reciprocal space, (000), to represent the wavevector of the incident electron beam. The Ewald sphere maps the magnitude of the incident wavevector to the reciprocal space lattice centered at the point P.

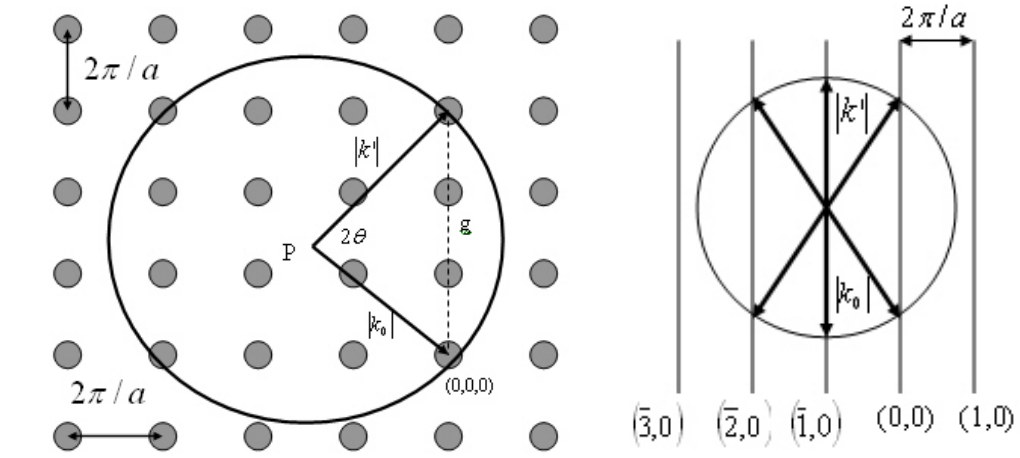

(a) (b)

Figure 2.2: Ewald Sphere constructions for (a) 3D and (b) 2D reciprocal space

If any of the reciprocal lattice points are intersected by the sphere then the condition for elastic scattering is satisfied (i.e. there is a change in momentum of the beam but there is no change in energy) with the scattered beam having a wavevector k. The condition for constructive interference for the elastically scattered electron is that

the change in the electron wavevector must be equal to a reciprocal lattice vector given by g_{hkl} [12]

$$k' - k_0 = g_{hkl} \quad \textbf{2.2}$$

From Figure 2.2 (a) it can be seen that

$$\sin\theta = \frac{|g|/2}{|k_0|} \quad \textbf{2.3}$$

And using Pythagoras

$$|g| = 2\pi\sqrt{h^2 + k^2 + l^2}/a \quad \textbf{2.4}$$

Equation 2.4 can be rearranged to form the Bragg condition for diffraction

$$n\lambda = 2d\sin\theta \quad \textbf{2.5}$$

LEED is a direct representation of the surface reciprocal lattice and is a simplified 2D version of the 3D case just presented. This means the requirements for diffraction are much less stringent as only the component of the wavevector parallel to the surface must be conserved when investigating a 2D surface. Constructing an Ewald sphere in two dimensions does not reproduce the same construction as in three dimensions. It can be shown that instead of showing reciprocal lattice points, in two-dimensions a diagram would show reciprocal lattice rods as in Figure 2.2(b). This arises because if the surface forms a completely two-dimensional net the period distance normal to the surface is infinite. The Bragg diffraction condition can now be satisfied over a wide range of energies and geometries. Diffraction occurs at all energies provided the corresponding rod lies within the Ewald Sphere.

2.2.2 LEED Analysis

LEED is a technique widely used for checking the cleanliness and ordering of crystal surfaces. Adsorbed species will influence the diffraction spots and with qualitative analysis of the spot positions in the diffraction pattern the symmetry and alignment of the adsorbate with respect to the substrate structure may be determined. There are two types of symmetry operators required to discuss the symmetry properties of two dimensional structures, point symmetries and line symmetries. Point symmetry refers to the rotational symmetry which may exist about some point or points in the unit cell. Line symmetry indicates the existence of lines or planes about which the cell has mirror reflection symmetry or glide-reflection symmetry [13]. Mirror reflection

symmetry occurs when the mirror image of the initial geometrical configuration of the unit cell is regenerated on the opposite side of the plane. Glide-reflection symmetry requires a combination of both reflection and translation along the mirror plane to bring the unit cell into coincidence with the initial geometrical configuration of the unit cell. These glide-reflection symmetries result in systematic absences of Bragg reflections in the LEED pattern [14].

The arrangements of adsorbates in a particular domain or phase can have at most the symmetry indicated by the LEED pattern. This is because the diffraction pattern is a composition of the individual patterns from different surface arrangements within the coherence length of the electron beam. The coherence length, typically 5 -10 nm, is limited by the energy spread of the incident beam and its angular divergence [12]. This also sets the maximum long range order of the surface that can be probed using LEED. Only structures ordered over lengths comparable to the coherence length contribute to the LEED pattern. This means that if there is a preferential formation of a particular domain or phase on the surface, the Bragg spots associated with that structure will have a greater intensity. Spots arising from the periodicity of the bulk planes are called integral order spots and spots arising from the different periodicity of the surface are called fractional order spots. Ordered domains or phases at lengths below the coherence will produce weaker Bragg spots and a higher background over the diffraction pattern.

2.2.3 Experimental Details

The LEED experiments presented in this thesis were performed in three different titanium sublimation pumped ultra high vacuum systems. The I(V) LEED spectra were recorded using a rear view Vacuum Generator (VG) LEED system in a dedicated UHV chamber shown schematically in Figure 2.4. The electrons are thermally emitted from a heated tungsten filament and collimated by the Wehnelt lens, which has a small negative bias with respect to the filaments. A set of lenses are used to focus the electron beam. This beam backscatters from the sample surface, passes through a set of grids, which functions to select only the electrons which are elastically scattered from the surface and are then accelerated to a fluorescent screen (Figure 2.3). When they strike the screen, they cause the phosphor to glow, revealing the diffraction pattern. These images are stored at different electron energies with the help of a CCD camera and a dedicated PC. The cleanliness of the Cu(100) crystal surface was checked using Auger Electron Spectroscopy (AES). It was deemed clean when no contaminants (e.g. oxygen

at 509eV and carbon at 262eV) could be observed above the AES noise level and a sharp p(1×1) LEED pattern with low background intensity was observed. A similar VG LEED system was used in the photoemission experiments performed at the Institute for Storage Ring Facilities in Aarhus (ISA). A third rear view Omicron Spectaleed system [15] was used to determine the different Sn/Cu{100} phases in the STM system. This system had a Lanthanum Hexaboride Filament (LB_6), which produces good emission characteristics at low power inputs. It yields a higher emission current and lower energy spread than the thoriated tungsten filament in the VG LEED system.

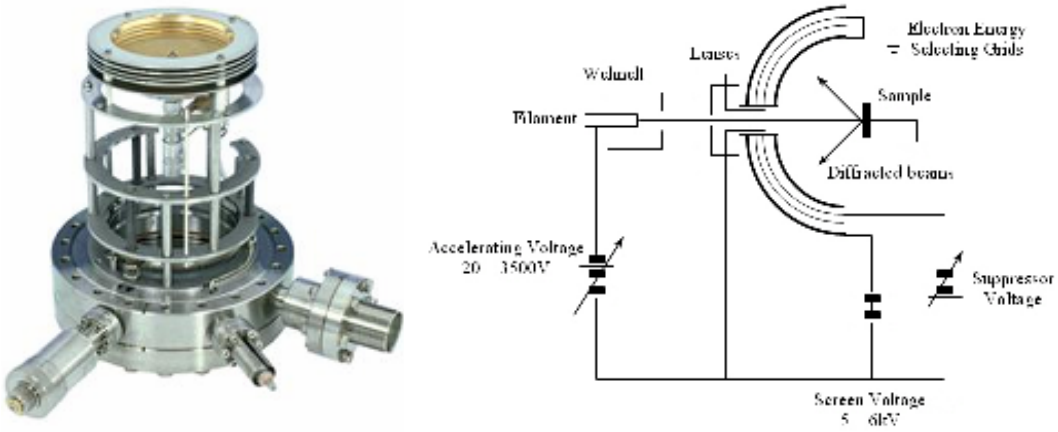

Figure 2.3: Picture and schematic of LEED system [15]

All I(V) LEED data were taken using the EE2000 Smartool software program [16]. This program permits the measurement of different spot intensities by controlling the electron beam energy. Modelling of LEED patterns was carried out using the LEED pattern simulator LEEDpat [17]. This program is designed to help in the interpretation of experimentally observed LEED spot patterns for well-ordered surfaces especially in the presence of superlattices. In particular it allows the determination of which 2D surface lattices are compatible with an observed LEED pattern. Providing extensive 2D symmetry information, it can show all rotational, mirror and glide symmetries that are compatible with the observed pattern. Rotational domains and glide plane extinction of spots are taken into account. While LEEDpat does not itself predict structural models or determine atomic positions, it does allow the user to narrow down possible structural models of the surface and to propose atomic positions in the actual structure.

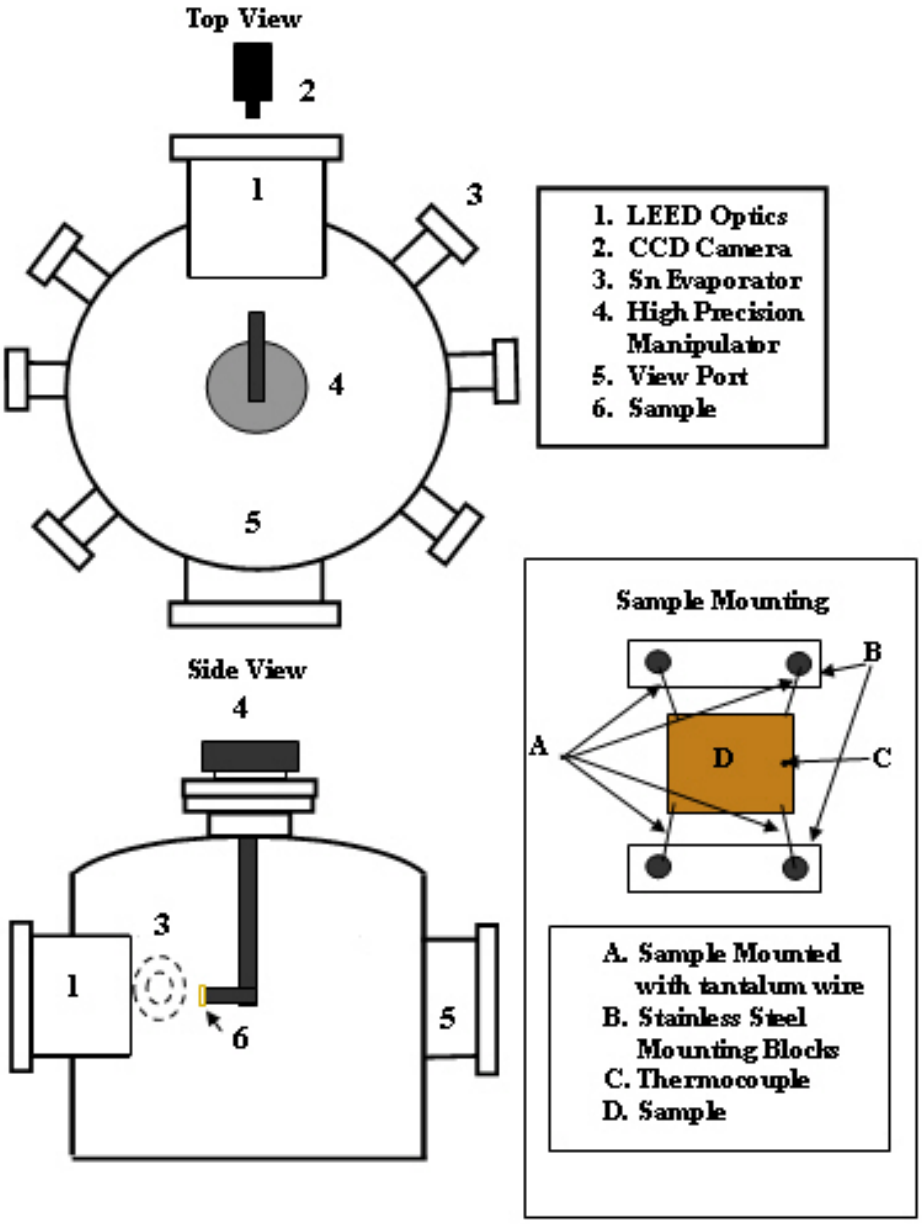

Figure 2.4: Schematic diagram of the dedicated LEED UHV system and sample mounting set-up

2.2.4 Sample Mounting

In both the LEED and the photoemission experiments the crystal sample was mounted to the high precision manipulator by suspending the sample between two stainless steel blocks with 0.25mm diameter tantalum wire secured through four mounting holes in the crystal (Figure 2.4). Sample heating was achieved by passing direct current through the tantalum support wires. A chromel-alumel thermocouple was placed through a fifth 0.25mm diameter hole, to the side of the sample. This allowed direct measurement of the sample temperature.

2.3 Scanning Tunnelling Microscopy (STM)

Scanning Tunnelling Microscopy (STM) was developed by G. Binnig, H. Rohrer, and co-workers at the IBM Zurich Research Laboratory in 1981[18] [19] [20]. STM is a practical application of the principle of quantum mechanical tunnelling, which describes how electrons can tunnel through a potential energy barrier. In the STM technique an atomically sharp conducting tip is brought to within a few Ångströms of a conducting sample surface. The vacuum gap between the two conducting materials forms the potential energy barrier. When a potential difference is applied electrons can tunnel between the sample and the tip, resulting in a tunnel current. This tunnel current depends exponentially on the width of the vacuum gap between the tip and the sample. By raster scanning the tip over the sample surface and measuring the tunnel current an image of the surface topography with atomic resolution can be formed. These images are used to investigate the cleanliness and the structure of the sample surface on an atomic scale. By varying the potential bias or separation or both, the local density of electronic states can be probed.

2.3.1 Basic Tunnelling Theory

A simple one-dimensional model is adequate to illustrate the basic concepts of STM. The classical momentum ρ of an electron with mass m, energy E, propagating in a potential U(z) is given by:

$$\rho = \sqrt{((E - U(z))/2m)} \qquad \textbf{2.6}$$

Provided the electron has a nonzero momentum it can move within the region but it cannot penetrate a potential barrier if its energy is smaller than the potential energy, U, of the barrier.

The equivalent quantum mechanical expression for the state of the same electron is Schrödinger's equation, where the electron is described by a wave function $\Psi(z)$, which satisfies Schrödinger's equation [21]

$$-\frac{\hbar^2}{2m}\frac{d^2}{dz^2}\Psi(z) + U(z) = E\Psi(z) \qquad \textbf{2.7}$$

Where $\hbar = h/2\pi$ and h is Planck's constant. The vacuum forms a potential barrier between the two conducting surfaces, when they are sufficiently close together as shown in Figure 2.5. In this case the two conductors are the tip and the sample surface. A rectangular potential barrier is used to illustrate the interaction between of an electron

with the barrier. By solving the Schrödinger's wave equation, an electron can be described as a travelling wave outside the potential barrier

$$\Psi(x) = \Psi(0)e^{\pm ikx} \quad \text{where } k = \frac{\sqrt{2mE}}{\hbar} \qquad 2.8$$

and within the barrier

$$\Psi(x) = \Psi(0)e^{\pm \kappa x} \quad \text{where } \kappa = \frac{\sqrt{2m(\Phi - E)}}{\hbar} \qquad 2.9$$

This predicts an exponential decaying solution for the electron wave function within the classically impenetrable barrier [21]. A solution of the form depicted in Figure 2.5 shows that there is a finite probability of finding the electron both outside and within the barrier. This phenomenon is called quantum mechanical tunnelling and it depends exponentially on the thickness of the barrier [22].

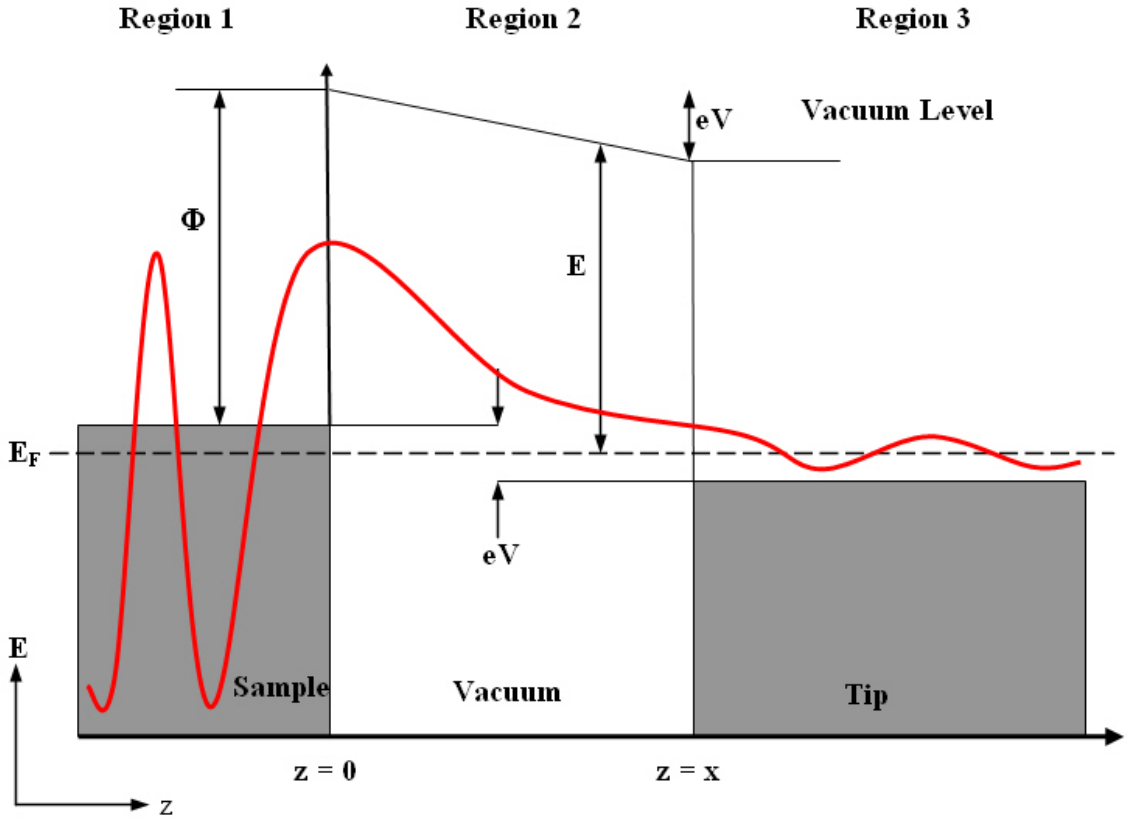

Figure 2.5: Schematic diagram of a one-dimensional tunnel junction under an applied bias voltage *V*.

The tunnelling probability is proportional to the ratio of the probabilities of finding the particle on either side of the barrier, i.e. the ratio of the squares of the wave function at these points:

$$|\Psi(d)|^2 = |\Psi(0)|^2 e^{-2\kappa d} \quad \textbf{2.10}$$

If the vacuum level is taken as the zero point for energy, then the Fermi level is $E_F = -\Phi$, where Φ is the work function. The work functions of the tip and the sample are assumed to be equal. The height of the potential barrier is determined by the work function of the tip and sample. In the absence of a bias voltage electrons can tunnel in either direction so there is no net tunnel current. In the STM a bias voltage V can be applied to the sample, then electrons within the energy range $E_F - eV \le E \le E_F$ produce a net tunnelling current. For small bias voltages, eV<<Φ, only electrons about the Fermi energy are probed. The probability of an electron in the n^{th} energy state tunnelling through a barrier of with z is

$$P \propto \left|\Psi_n(0)\right|^2 e^{-2\kappa d} \quad \textbf{2.11}$$

where $\kappa = \frac{\sqrt{2m\Phi}}{\hbar}$ is the inverse decay length for all tunnelling electrons [21] [23]. The total tunnel current I, which is proportional to the probability of electrons tunnelling through the barrier, from the sample to the tip is calculated by summing over all the possible states in the energy range, $E_F - eV \le E \le E_F$ [23].

$$I(v) \propto \sum_{E_n = E-\varepsilon}^{E} |\Psi_n(0)|^2 e^{-2\kappa z} \quad \textbf{2.12}$$

For small bias voltage the density of states of a metal is constant between E_F–eV and E_F and the current can be written in terms of the local density of states (LDOS) of the sample at the Fermi level. At a location z and energy E, the LDOS $\rho(z = 0, E = E_F)$ of the sample is defined as [24] [25]

$$\rho(z, E) \equiv \lim_{\varepsilon \to 0} \frac{1}{\varepsilon} \sum_{E_n = E-\varepsilon}^{E} |\Psi_n(z)|^2 \quad \textbf{2.13}$$

for sufficiently small energy, ε. The tunnel current at the tip can be written in terms of the LDOS of the sample [23]

$$I(V) \propto V \rho_s(0, E_F) e^{-2\kappa z} \quad \textbf{2.14}$$

The sensitivity of the tunnel current to any change in z of the tip to the sample, results in the very sensitive resolution of the STM in the direction normal to the surface, typically a vertical resolution of 0.001 nm is attainable with the STM [12].

2.3.2 STM Analysis

Proper analysis of STM images requires some careful consideration. The contour map of the surface produced by the STM is both electronic and topographic in origin as it depends on the overlap of the wave functions of the tip and surface and follows a height contour of constant electron density. Simple interpretation in terms of atomic height although intuitively plausible can also be extremely misleading [26]. The STM data was analysed with the software package WSxM (version 3.0 Beta, development 12.0) [27].

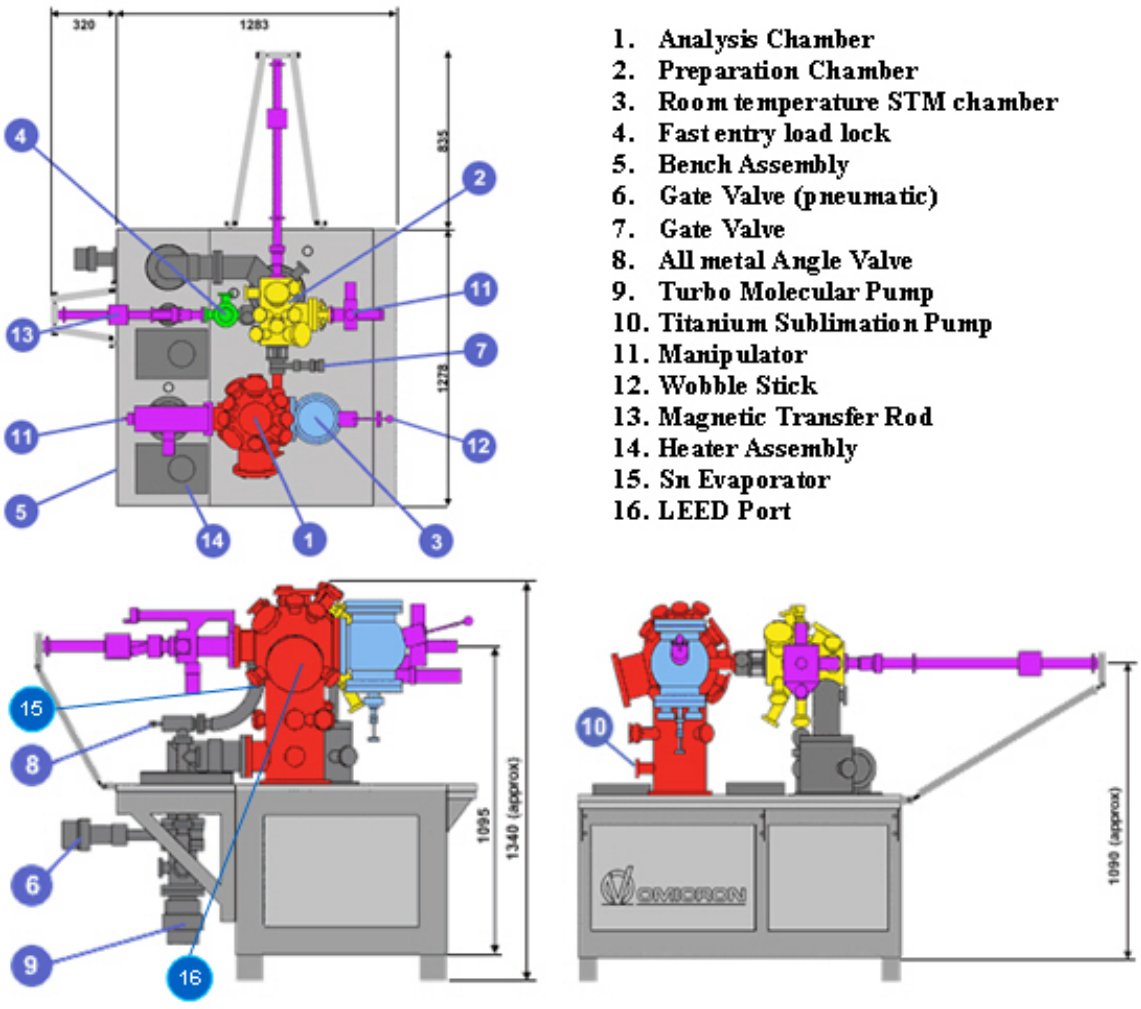

Figure 2.6: Diagram of the Omicron UHV system [15]: the preparation chamber (yellow), the analysis chamber (red), the fast entry load lock (green) and the STM chamber (light blue).

2.3.3 STM Experimental Details

The STM experiments presented in this thesis were all performed under UHV using an Omicron Variable-Temperature STM. The UHV system consists of three vacuum chambers: a sample preparation chamber, an analysis chamber and an STM chamber. Samples and tips can be introduced through a fast-entry load lock attached to the preparation chamber. The layout of the system is shown in Figure 2.6.

The sample holder is manufactured from tantalum (Ta) with a keyhole at the front so that it can be captured by a sample transfer mechanism and transported within the UHV system (Figure 2.7). Two strips of Ta were folded into incisions along the two sides of the crystal and spot welded to the sample holder to secure the Cu(100) crystal.

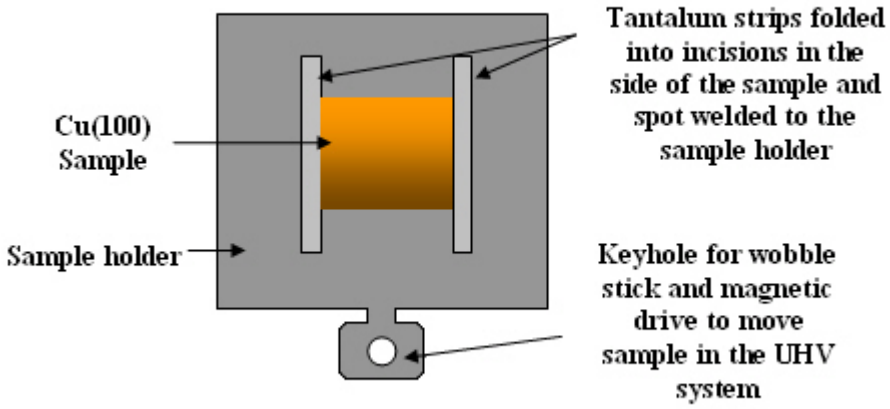

Figure 2.7: Diagram of tantalum sample holder.

The STM operates by measuring a small tunnel current (~0.1-10nA) between the sample and tip spaced a few angstroms apart with a potential difference (1mV to ~5V) applied between them. The tip is made from wire of tungsten (W) or platinum iridium alloy (Pt/Ir). The wire is electronically etched in an electrochemical bath, for example sodium hydroxide (NaOH), to produce an atomically sharp tip. The W tips build up an oxide layer in air and need to be cleaned and reformed in situ by nanostructuring. This involves applying a high voltage (~10V) to the tip thus creating a high electric field between the tip and surface. There are two modes of operation of the STM: constant current mode or constant height mode, both shown in Figure 2.8. In constant height

mode the tip is scanned across the surface at a constant height while the tunnel current varies with tip-sample separation. This method allows rapid scanning but it can only be performed on atomically flat surfaces to avoid the tip crashing into step edges or other protrusions. Since the tunnel current varies by an order of magnitude for a tip sample separation of 1 Å, this mode requires a tunnel current amplifier with a large input dynamic range. In constant current mode, the tunnel current is kept constant by a feedback system. The tip traces out the shape of the surface as it scans across the sample. The changes in the tip displacement provide an image of the surface. Due to the stepped nature of the Cu crystal surface, the STM experiments in this thesis were performed in the constant current mode.

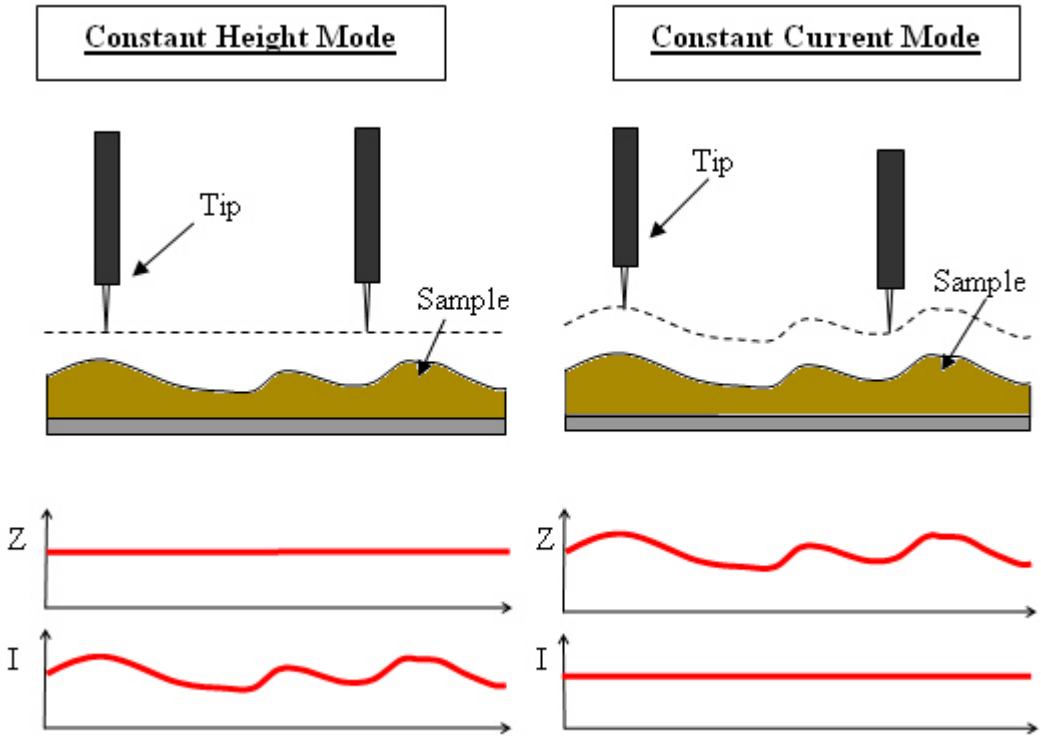

Figure 2.8: Illustration of the two scanning modes of the STM: constant height mode and constant current mode. Where z is the vertical displacement of the tip and I is the measured tunnelling current.

A hollow cylindrical piezoelectric transducer allows the controlled vertical (z) and lateral (x, y) positioning of the tip over the sample surface. The tip is held in a magnetic holder at the top of the piezo tube. By convention the z-axis is taken as normal to the sample surface and the surface itself is then the x-y plane. The outer surface of

the tube is divided into four electrodes with a single inner electrode. Lateral movement is achieved by applying equal and opposite voltages to two opposing outer electrodes while keeping the other two outer electrodes grounded or at a constant voltage. The vertical movement is achieved by applying the same voltage to the four outer electrodes and grounding the inner electrode.

In constant current mode the height of tip is controlled by an electronic feedback system which acts to maintain a constant tunnel current (Figure 2.9). The tunnel current is amplified by passing it through an amplifier placed as close as possible to the tip inside the vacuum system. The amplified current is then converted into a voltage which is linearised in a logarithmic amplifier in the feedback loop to improve the dynamic range of the feedback and extract the distance dependence. The output signal from the log-amp is compared with the preset tunnel current in the comparator, the difference signal is fed back to the z-piezo high voltage amplifier and the tip is moved accordingly to bring the tunnel current back to the preset value thus maintaining a constant tunnelling current. The time constant of the feedback loop limits the maximum scan rate.

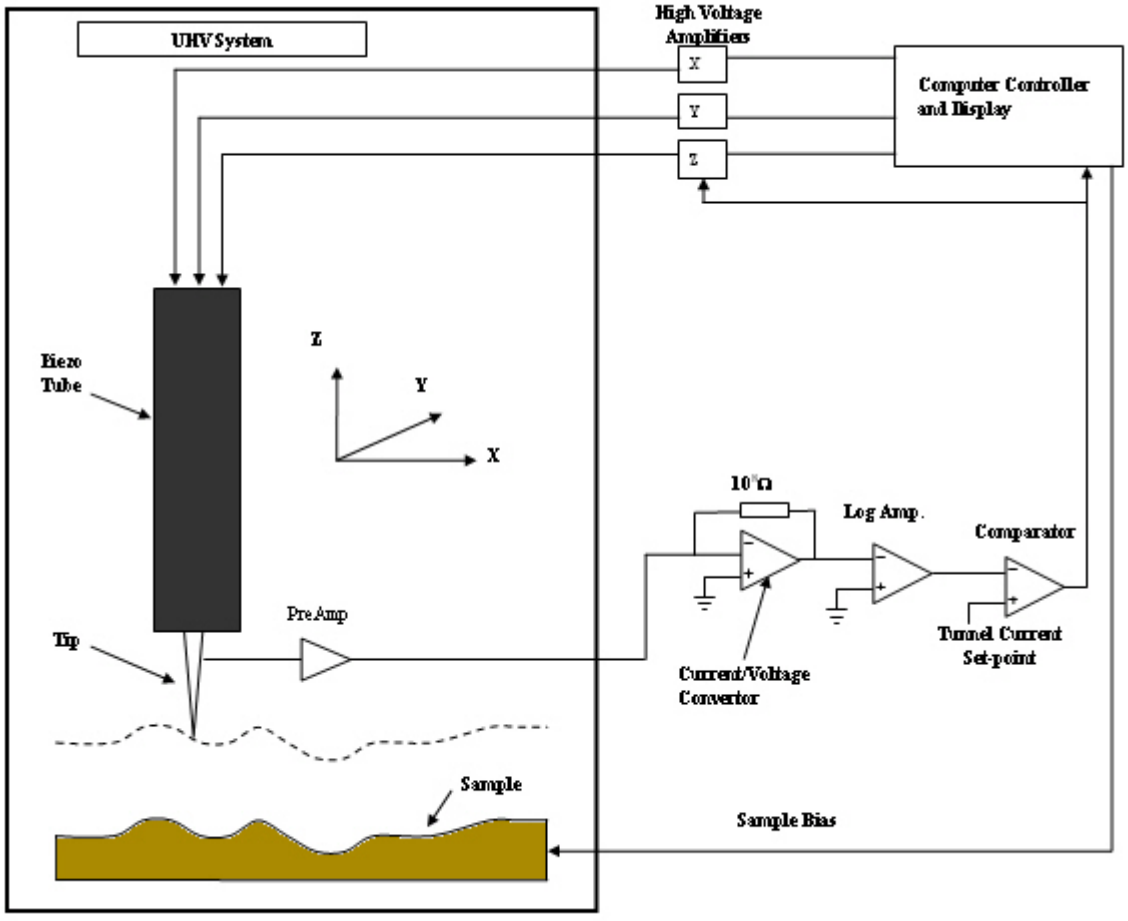

Figure 2.9: Schematic diagram of feedback system for operating the STM in constant current mode

The typical corrugation amplitude on an atomic surface is of the order of Ångströms or less. Considering that the typical floor vibrations are at least six orders of magnitude greater in amplitude than the surface corrugation any disturbance from external vibrations is detrimental to the atomic resolution, therefore vibration isolation is critical for the STM system. Passive damping is achieved by through viscoelastic materials between the system and the floor and metal springs combined with an eddy-current damping system consisting of copper elements and permanent magnets of the Omicron VT-STM.

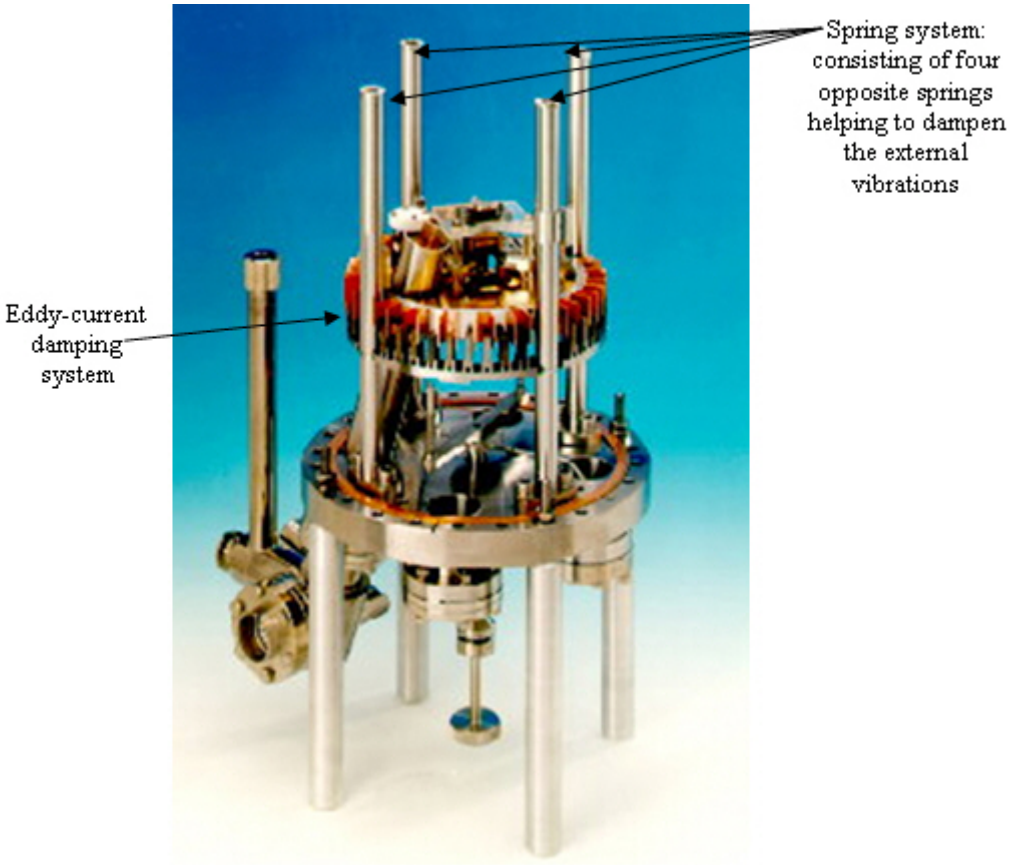

Figure 2.10: Image showing the damping system for the Omicron VT-STM system [15].

2.4 Photoemission Spectroscopy

Photoemission spectroscopy (PES) relies on the principle of the photoelectric effect, which was explained by Einstein in 1905. A sample bombarded with photons

will emit electrons with a kinetic energy, E_{kin}, relative to the vacuum level (Figure 2.11) given by:

$$E_{kin} = h\nu - E_B - \Phi \qquad \textbf{2.15}$$

Where hν is the incident photon energy, E_B is the binding energies of the electron relative to the Fermi level and Φ is the work function of the sample. The use of photoemission to study the chemical and electronic structure of solids was developed as an analytical tool by Seigbahn [28] in the 1950's and 1960's. Accurate measurements of the electron binding energies provide information about the electronic structure of a sample. In this work photoemission is used: (1) to examine the Cu 3p and Sn 4d core level spectra in Sn/Cu(100) surface alloys (these measurements use high resolution core-level spectroscopy (HRCLS)), and (2) to measure changes in the work function and valence band spectra for all five submonolayer surface phases of the Sn/Cu(100) surface alloy system.

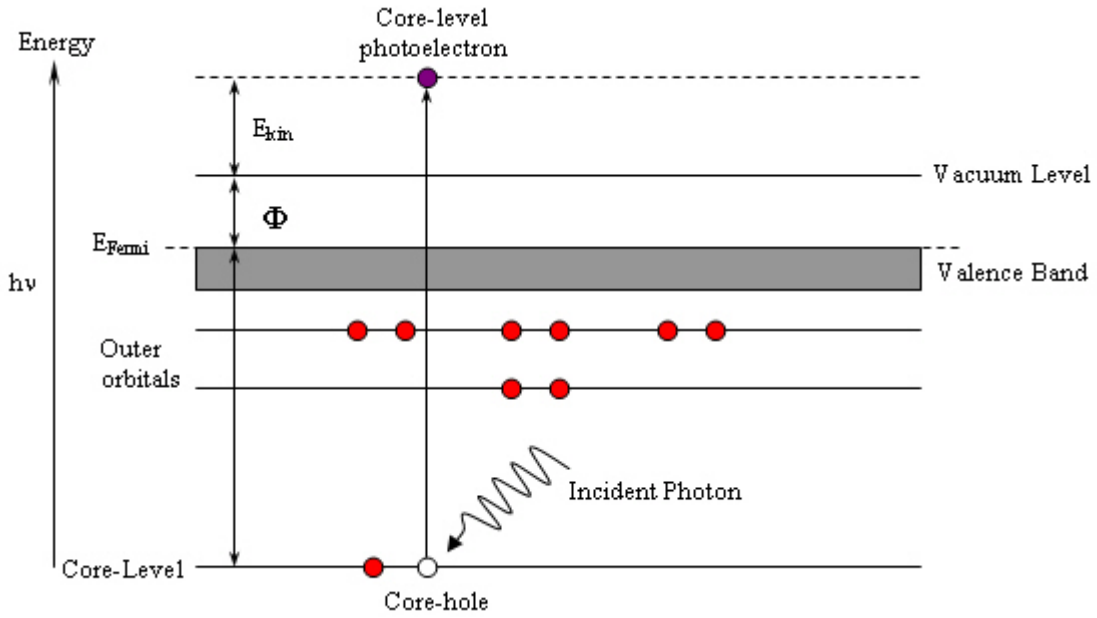

Figure 2.11: Schematic diagram of the photoemission process.

With the correct choice of experiment parameters photoemission techniques can be used to analyse the near surface region of the sample. As seen in section 2.1, electrons with kinetic energies in the range 30 – 150 eV have an IMFP < 1.0 nm, which is the average length an electron can travel without energy loss due to a collision. This means that electrons observed with kinetic energies in this range that have left the solid

without suffering inelastic scattering have originated from the first few atomic layers. Synchrotron radiation sources provide a continuous range of photon energies which can be tuned over a range of photon energies. In particular, in photoemission experiments the photon energy can be selected to maximise the surface sensitivity.

2.4.1 Core-Level Spectroscopy

Core level spectra are obtained when electrons from deep lying atomic orbitals are excited by incident photons, resulting in the emission of photoelectrons. These spectra display features produced by both elastically and inelastically scattered electrons within the sample. Some of the excited core level photoelectrons are involved in collisions giving rise to an inelastically scattered background in the spectra. This background increases on the low kinetic energy side of the peak. The core level photoelectrons elastically scattered in the surface region produce sharp intense peaks in the spectra. Since each element has a characteristic core level spectrum, it is possible to use HRCLS to chemically identify the elements of the sample. Similarly atoms in different chemical environments give rise to core-level shifts in binding energy [29].

2.4.2 Analysis of Core Level Spectra

A model lineshape is usually fitted to each component in a core level spectrum in order to extract information about the binding energies, relative intensities and line widths of the different components. The width of the peak is associated with the finite lifetime of the core hole. This line shape is Lorentzian in nature and has a natural broadening associated with it. This can be calculated from the Heisenberg uncertainty relationship [12]:

$$\Gamma = \frac{h}{\tau} \qquad \textbf{2.16}$$

Where Γ is the intrinsic width of the peak in eV, h is Planck's constant in eV-seconds and τ is the core-hole lifetime in seconds. Since the lifetime of the core-hole is dictated by how quickly another electron can fill the hole, it is evident that the core-hole lifetime of inner shell electrons in general will be shorter than those of more loosely bound electrons due to a greater probability of an electron from the outer shell electron filling the core-hole. Additionally core-holes formed in atoms with a larger number of shells have shorter lifetimes due to increased probability of an outer shell electron filling the core-hole.

In practice the overall shape of the photoemission peak is a convolution of the intrinsic Lorentzian lineshape of the core-level and a Gaussian component. This additional Gaussian broadening is caused by the finite instrumentation resolution and the energy spread of the incident radiation. In the case of conventional X-ray photoemission spectroscopy (XPS) studies, the energy spread of the incident X-rays results in the instrumental broadening dominating over the intrinsic Lorentzian lineshape of the peaks so, the peaks become essentially Gaussian in nature. However, the much narrower intrinsic lineshape of the incident radiation obtained from synchrotron light sources allows for much higher resolution studies of surfaces by greatly reducing the Gaussian component in the measured lineshape. As mentioned in section 2.4.1 various processes result in energy loss resulting in a tail on the low kinetic energy side of the peak. These energy loss processes can be intrinsic, due to excitations taking place during the photoionisation process, or extrinsic, due to inelastic scattering of the photoelectron after the photoionisation process. When the escape depth of the photoelectron is small and the energy range is narrow the intrinsic losses will dominate and these can be accurately modelled.

2.4.3 The Doniach-Sunjic Lineshape

In metals, by far the most important intrinsic loss process is the creation of low energy electron-hole pairs. As the conduction electrons adjust themselves to screen the core hole, they will be scattered off the other electrons in the Fermi sea leaving it in an excited state. A theoretical line-shape that takes this process into account along with the finite lifetime of the core-hole has been derived by S. Doniach and M. Sunjic [30].

$$D(E) = \frac{\Gamma(1-\alpha)\cos\left[\frac{\pi\alpha}{2} + (1-\alpha)\arctan\left(-\frac{E-E_B}{\gamma}\right)\right]}{\left(1+\frac{(E-E_B)^2}{\gamma^2}\right)(1-\alpha)/2} \qquad \textbf{2.17}$$

where γ is the Lorentzian lifetime width and α is the asymmetry parameter.

2.4.4 The Voigt Lineshape

The Doniach-Sunjic lineshape was not available in the AAnalyzer fitting program and instead the spectra were fitted using a Voigt lineshape. The Voigt lineshape is a convolution of a Gaussian and a Lorentzian lineshape [31].

$$I(E) = \int_{-\infty}^{+\infty} \frac{\left(\frac{1}{2}\omega_L\right)^2}{\left(\frac{1}{2}\omega_L\right)^2 + \left(E - E_0\right)^2} \exp\left[-\frac{1}{2}\left(\frac{\sqrt{8}\ln 2.\,\tilde{E} - E}{\omega_G}\right)^2\right] d\tilde{E} \qquad \textbf{2.18}$$

where I is the intensity measured at the energy E, ω_L and ω_G are the full width at half maximum (FWHM) of the Lorentzian and Gaussian respectively. E_0 is the peak position of the Voigt function and $\tilde{E}$ represents the energy values over which the integration is carried out.

AAnalyzer [32] and WinSpec [33] curve fitting programs were used for fitting all the core level spectra in this thesis. These programs allow the user to input multiple peaks of various different types in addition to a choice of different backgrounds in order to fit the experimentally obtained lineshapes.

2.4.5 Peak Shifts

Atoms at the surface of a sample are bonded to their neighbours in a way that differs from that of atoms in the bulk sample. This is due to the missing next atomic layer and results in a differing chemical environment to that experienced by atoms in the bulk. The atoms in the surface layers often rearrange themselves or reconstruct to minimise the overall energy of the system. Surface reconstructions frequently result in the introduction of a new component to the photoemission spectra. However, there are many other effects that result in the emergence of new core level components, which must also be considered for the correct interpretation of data [34].

(a) Initial state effects

Both initial and final states effects contribute to the observed binding energy $E_{B,}$ of a core level. The initial state is simply the ground state atom prior to the emission of a photoelectron. It can be seen that a change in the initial state energy $E_i(n)$ will result in a charge in the E_B of the core level. The initial state energy of an atom is changed by the formation of chemical bonds with other atoms. It is found that for many samples, the final state effects have similar magnitudes irrespective of the initial state energy. In these cases it can be shown that the change in E_B of the core level is equal to the change in magnitude of the orbital energy ε_k yielding the formula

$$\Delta E_B = -\Delta\varepsilon_k \qquad \textbf{2.19}$$

The formation of a bond that results in charge transfer from the investigated atom to its bonding partner will result in an increase in the E_B of the atom relative to its unbonded

state, while charge transfer from the bonding partner to the investigated atom will result in a decrease in the E_B relative to its unbonded state.

(b) Final state effects

Within an individual atom involved in the photoemission process, the predominant final state effect in evidence is a relaxation effect. The formation of a core hole in an atom by the emission of a photoelectron will result in a rearrangement of the remaining electrons in the order to minimise the energy of the ionised atom. In all cases this results in a reduction of E_B of the measured photoelectron. Additional extra-atomic relaxation is also observed in many cases as the surrounding atoms contribute to the minimisation of the energy of the ionised atom. This extra-atomic contribution to the effective screening of a core hole can be observed with the deposition of an adsorbate onto a metallic surface. The formation of a core hole in the adsorbate by the photoemission process results in a screening effect, which reduces the measured E_B of the core level from which the electron was emitted. Extra-atomic screening effects by metallic surfaces have been observed for the physisorption of xenon on Au(110) surface [35] and additionally for organics deposited on metal surfaces.

2.4.6 The Photoionisation Cross Section

Consider the photoionisation process $\Psi_i \rightarrow \Psi_f$, where Ψ_i denotes the initial state and Ψ_f denotes the final state consisting of the photoelectron and the ionised atom. The transition probability per unit time can formally be written as:

$$P_{i\rightarrow f} = \frac{2\pi}{\hbar}\rho(E)\left|\langle \Psi_i | V | \Psi_f \rangle\right|^2 \qquad \textbf{2.20}$$

Where $\rho(E)$ is the energy density of final states and V is the perturbation of the atomic Hamiltonian, representing the action of the photons. This equation is called the Fermi Golden Rule. The photoionisation cross section is then calculated by integrating Equation 2.20 over all possible final states to obtain the total transition probability per unit time, which is then divided by the photon flux. The availability of a variable photon energy source, synchrotron radiation, is of crucial importance in obtaining high resolution core level spectra by tuning the source to the photon energy to the maximum photoionisation cross section

2.4.7 Valence Band Spectroscopy

As discussed in section 2.4.1 core level spectra result from photoelectrons emitted from deep lying energy level, which are comprised of relatively sharp intense peaks that can be used to identify different chemical environments. As schematically shown in Figure 2.11 the valence band region of the photoemission spectrum is the region close in energy to the Fermi level, and therefore corresponds to emission from outer atomic orbitals with relatively low E_B. However this region of the spectrum is of great interest because the orbitals that make up this region are the atomic orbitals generally involved in bond formation and in defining the electronic behaviour of the material. Therefore a large amount of information can be deduced from valence band investigations of samples.

2.4.8 Evaluating Valence Band Spectra

While HRCLS studies are essential for building up a picture of the elements present in the sample in addition to information regarding the chemical environment of the different elements present, valence band analysis provides information that cannot be obtained from a core level study and so is essential for a thorough investigation of molecular thin films and submonolayer surface alloys.

2.4.9 Work Function Measurement

Theoretically the work function consists of contributions from a bulk component and a surface component given by:

$$\Phi_{total} = \Phi_{bulk} + \Phi_{surf} \qquad \textbf{2.21}$$

The bulk component depends exclusively on the bulk properties of the material and is not altered by adsorption of molecules on the surface. The surface component of the work function is due to the difference in the electrostatic potential inside and outside the metal surface. Experimentally the work function of the sample can be calculated from the cut-off energy of the secondary electron tail and is usually obtained in conjunction with the valence band spectra for metal/metal interfaces. A bias V_{Bias} is usually applied to the sample to avoid the effects of low energy transmission of the analyser. The work

function of the sample can then be calculated from the width of the spectrum, accounting for the bias:

$$\Phi = h\nu - (E_{Fermi} - (\Phi_{Biased} - V_{Bias})) \quad \textbf{2.22}$$

where hν is the incident photon energy, Φ_{Biased} is the measured cut-off and V_{Bias} is the bias applied to the sample [29].

2.4.10 Synchrotron Radiation

The availability of a variable photon energy source is of crucial importance in obtaining high resolution core level spectra and ensuring the surface sensitivity of the experiment. Synchrotron radiation sources are continuously tuneable and produce X-ray radiation which is of the order of 10^6 times more intense than that obtained from conventional X-ray sources.

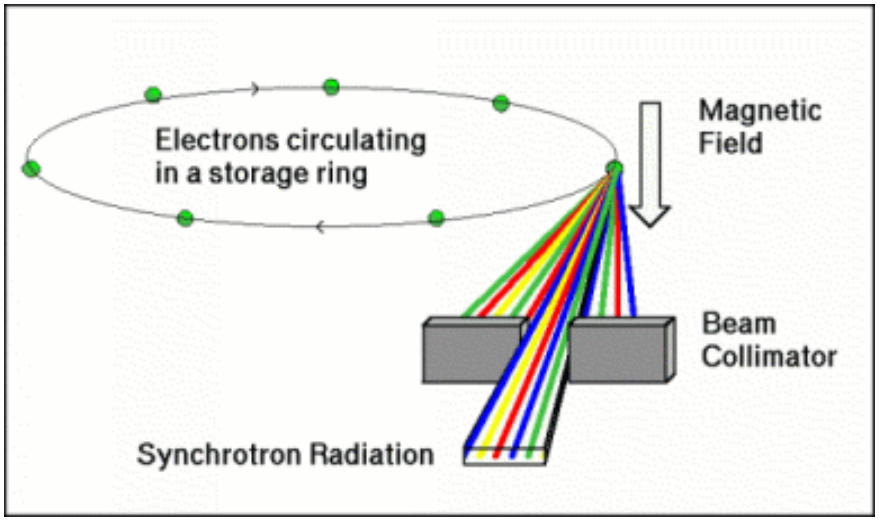

Figure 2.12: Diagram showing the emission of synchrotron radiation by high speed electrons undergoing acceleration due to magnetic field of a bending magnet.

Synchrotron radiation is emitted when charged particles moving at relativistic speeds are forced to follow curved trajectories, i.e. accelerated. Synchrotron Radiation was first visually observed in 1948 from the General Electric synchrotron in the USA during investigations into the design and construction of accelerators suitable for the production of very high-energy electrons. Since then many accelerators have been built and optimised for synchrotron radiation production, which has turned this interesting energy loss mechanism into a valuable research tool.

The Photoemission studies described in this thesis used synchrotron radiation produced by the electron storage ring at the Institute for Storage Ring Facilities in Aarhus (ISA). The storage ring is 40m in circumference with four straight sections, and four dipole, bending magnets as shown in the schematic diagram of the ASTRID Synchrotron (Figure 2.13). It is a dual purpose ring used for the storage of both ions and electrons, but for this work only the storage of electrons is of interest. The electron energy is E = 580MeV and the electron current is typically 150mA right after injection. Although the storage ring itself is under ultra high vacuum, electrons are removed by collisions with gas molecules, so the beam current decays. The lifetime of the beam is approximately 20 hours at 100mA. At the ISA, a new beam is injected every 24 hours during normal operation.

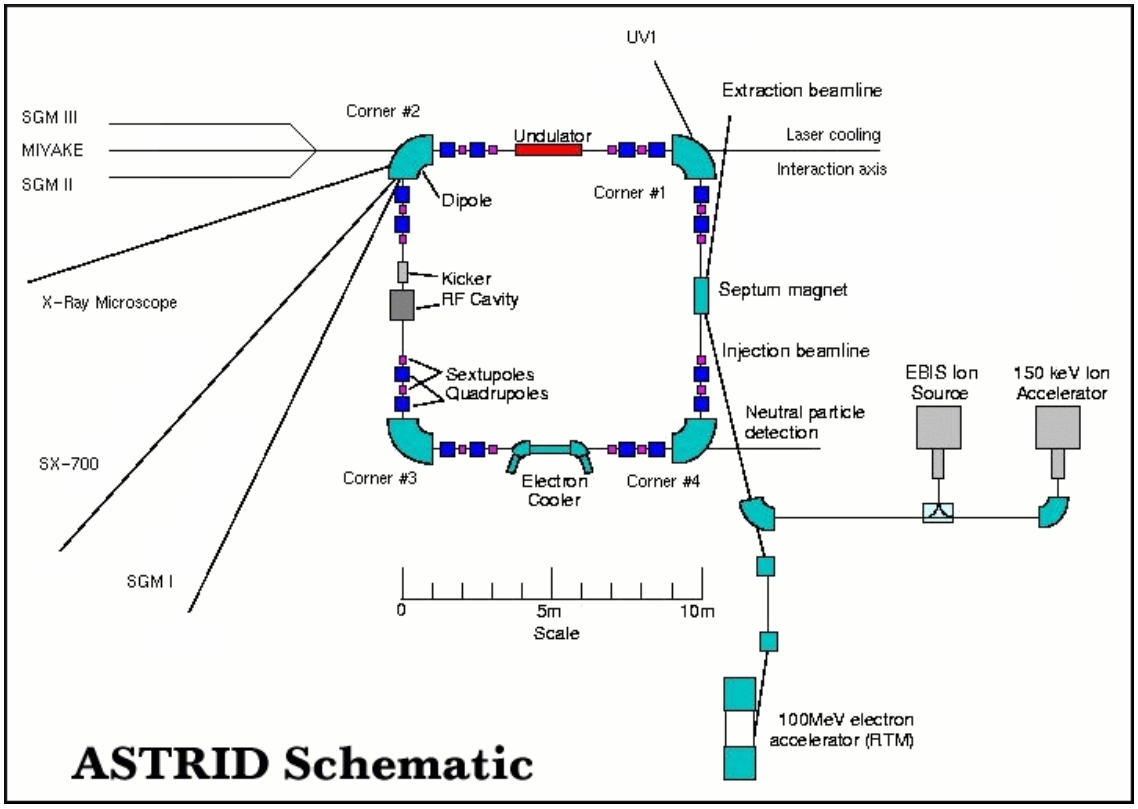

***Figure 2.13*:** Schematic diagram of ASTRID Synchrotron in the ISA [36] 36

As the electrons pass the bending magnets, they will follow a circular path with a radius of curvature ρ = 1.25m and emit electromagnetic radiation like any charged particle undergoing acceleration (Figure 2.12). The radiation emitted is extremely intense and collimated, and extends over a broad wavelength range from the infrared through the visible and ultraviolet, into the soft and hard x-ray regions of the electromagnetic spectrum. The specific radiation frequencies required for different

experiments are selected using a monochromator. The radiation is almost 100% linearly polarized in the plane of the storage ring in contrast to the unpolarised light from conventional ultraviolet and X-ray sources, which allows for orientation experiments such as near edge X-ray adsorption fine structure (NEXAFS). The electrons in the ring are "bunched", so the radiation is emitted in short pulses, of the order 10^{-9}s, which is useful in timing experiments [36].

2.4.11 Monochromator and Grating

PES and HRCLS experiments require well-defined photon energies. Therefore the "white" radiation from the synchrotron must pass through a monochromator before entering the experimental chamber. This experiment was performed on the SGM1 beamline in the ISA. The SGM1 beamline combines a spherical grating monochromator containing three gratings as shown in Figure 2.14. The polychromatic light enters the SGM1 through the entrance slit. A rotatable spherical grating monochromatises and focuses the light. A plane folding mirror ensures that the focal point of the monochromatic beam coincides with the exit slit within the entire energy range. The monochromatic beam leaving the monochromator is divergent and is therefore refocused by a toroidal focusing mirror just before it enters the analysis chamber.

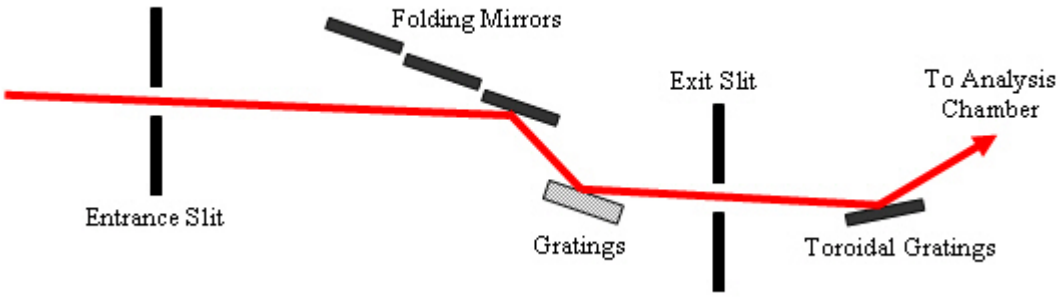

Figure 2.14: Schematic of the SGM1 monochromator.

Due to the coma aberration of the spherical grating, its usable range is limited as compared to a plane grating. To extend the energy range, the monochromator has a set of three gratings and mirrors, where each pair is optimised for a particular energy range, 25-80, 80-250 and 250-400eV. The energy resolution of the SGM1 monochromator for all three grating-mirror settings is shown in Figure 2.15.

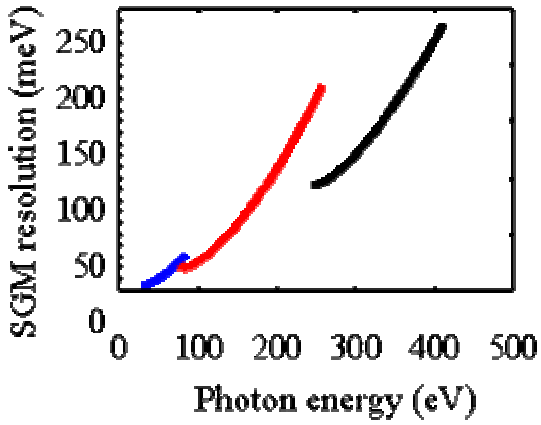

Figure 2.15: Energy resolution of the SGM1 monochromator with a typical working setting of 50μm slits [36].

2.4.12 The Electron Energy Analyser

The ejected photoelectrons are measured with a SCIENTA spectrometer and CCD camera-based multichannel detector system. This allows for fast acquisition of spectra with a high-energy resolution, typically 40meV. This energy resolution is a significant improvement over that available with many conventional laboratory based XPS sources. The spectrometer uses a hemispherical electron energy analyser. The analyser consists of five cylindrical or conical elements, as shown in Figure 2.16, which perform the functions of focusing the electrons onto the entrance slit before entering the hemispherical analyser, so that the transmission through the analyser is optimised, and retards or accelerates the electrons to a kinetic energy equal to HV, the pass energy of the hemispherical analyser, which is proportional to the voltage difference between the two concentric spheres. If an electron obtains a kinetic energy equal to HV it will pass through the analyser and be detected. The associated electron binding energy is then determined as:

$$E_B = h\nu - \left(R + HV + e\Phi_{an}\right) \qquad \textbf{2.23}$$

Where R is the effective retarding voltage and $e\Phi_{an}$ is the spectrometer work function. The detector system consists of a field termination net, which ensures a homogenous termination of the analyser field, two micro-channel plates that multiply each incoming electron ~10^7 times, a fluorescent screen toward which the electrons are accelerated to produce light flashes and a CCD camera to detect those flashes. The video data is processed by a dedicated microprocessor and the spectrum is transferred to a PC for further analysis.

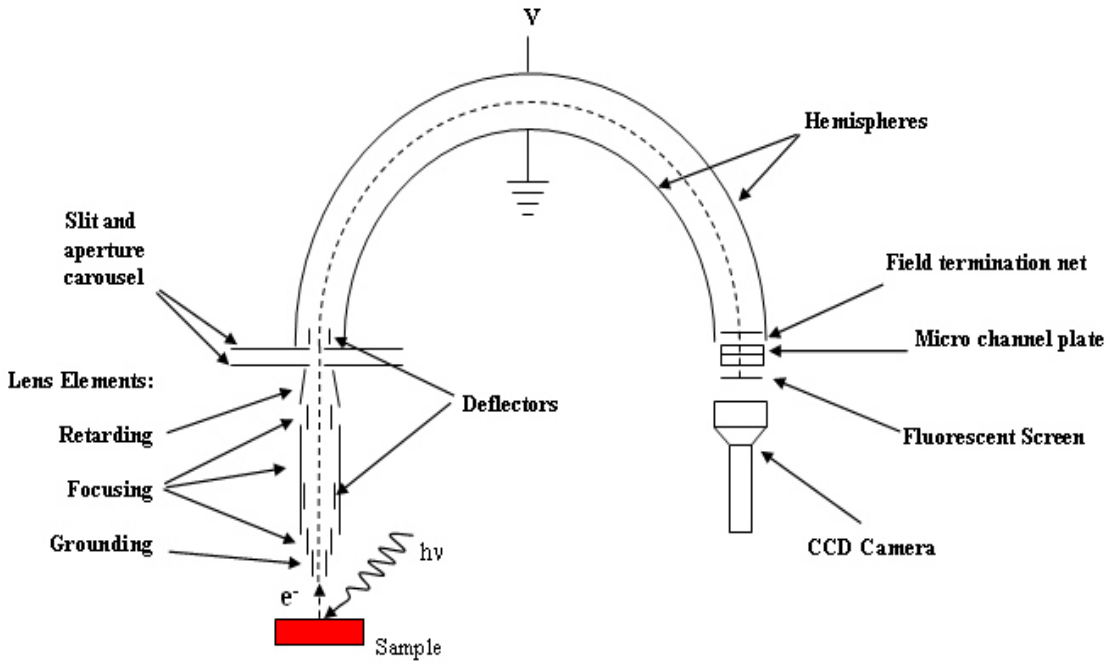

Figure 2.16: Schematic of the SCIENTA spectrometer and hemispherical electron analyser set up.

2.4.13 Experimental Setup

The PES and HRCLS experiments described in this thesis were performed on the SGM1 beamline at the ISA. This experimental station is designed primarily for surface sensitive experiments due to the 30-400eV energy range. The layout of the experimental chamber is shown in Figure 2.17. The end-station consists of two μ-metal UHV chambers, mounted on top of each other, the upper chamber is used for surface preparation, and the lower chamber is used for the photoemission experiments. μ-metal is a nickel-iron alloy which has high magnetic permeability and is used for effective shielding of the experiment from external magnetic fields. The two chambers are separated by a gate valve, this is to allow the preparation chamber to be pumped and baked separately from the analysis chamber and the bulky SCIENTA analyser. A base pressure of 10^{-10}mbar is readily achieved on this system after a 24-hour bakeout. The preparation chamber is equipped with an Ar+ gas sputter gun, LEED optics, a mass spectrometer, a quartz crystal monitor and a gas inlet system. The sample manipulator has x, y, z movement as well as polar rotations. A specially designed and built Knudsen cell Sn evaporator was mounted on the chamber for Sn deposition. The photoemission

experiments presented in this thesis were preformed with the samples in normal emission (NE) positions. In the normal emission sample position the surface of the sample is pointed in the direction of the analyser and the incident synchrotron radiation makes an angle of 35° with the surface normal.

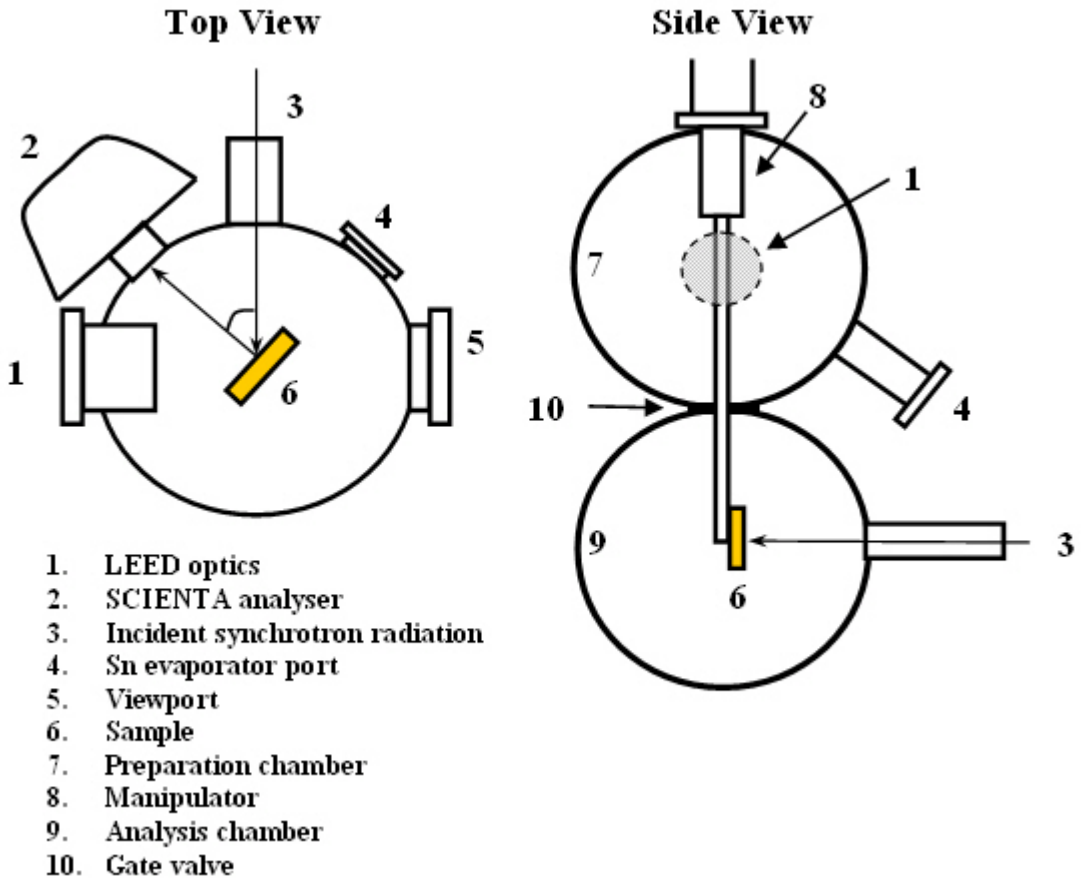

Figure 2.17: Schematic diagram of the experimental UHV chambers of the SGM1 beamline in the ISA.

Chapter 3: LEED and STM Study of Sn/Cu(100) Surface Phases

3.1 Introduction

In this chapter all of the previous research on the bimetallic alloys formed by the deposition of Sn on the Cu(100) surface is reviewed. The Sn/Cu(100) system is examined by LEED and STM providing further insight into Sn adsorption on the Cu(100). The surfaces sub-monolayer phases which are consistent with adsorbate induced reconstruction/surface alloy formation are presented. Previously proposed models, based on I(V) LEED, for each of the phases are reviewed with new LEED and STM results. Argile and Rhead [6] originally reported four submonolayer phases for the Sn/Cu(100) system: Phase I with Sn coverage ~ 0.18ML, Phase II with Sn coverage ~ 0.33ML, Phase III with Sn coverage ~ 0.5ML and Phase IV with Sn coverage ~ 0.625ML. These results were revised by McLoughlin [5] using Auger electron spectroscopy (AES), monitoring the LEED spot profiles as a function of evaporation time and double scattering LEED pattern simulations. This analysis indicated that Phases I-IV reached maximal perfection at Sn coverages of ~ 0.21, 0.37, 0.5 and 0.70 ML respectively. A new phase appearing between Phase II and Phase III was recently reported by Martinez-Blanco et al. [8] based on LEED measurements. This new phase is observed over a very narrow range of Sn coverage at ~0.45 ML. The LEED images exhibit diffracted beams which are not consistent with diffraction spots present in either Phase II or Phase III. This new phase has been designated as Phase IIH or higher Phase II.

3.2 Clean Cu

3.2.1 Sample Preparation

The structure of the bulk copper crystal is face centred cubic (fcc). The p(1x1) unit cell of the surface is shown in Figure 3.1 with an interatomic spacings of 0.255nm along the [011] and [01$\bar{1}$]directions. The interplanar distance between the {100} planes is 0.181nm, which is equal to half the lattice constant of 0.361nm of the face centred crystal.

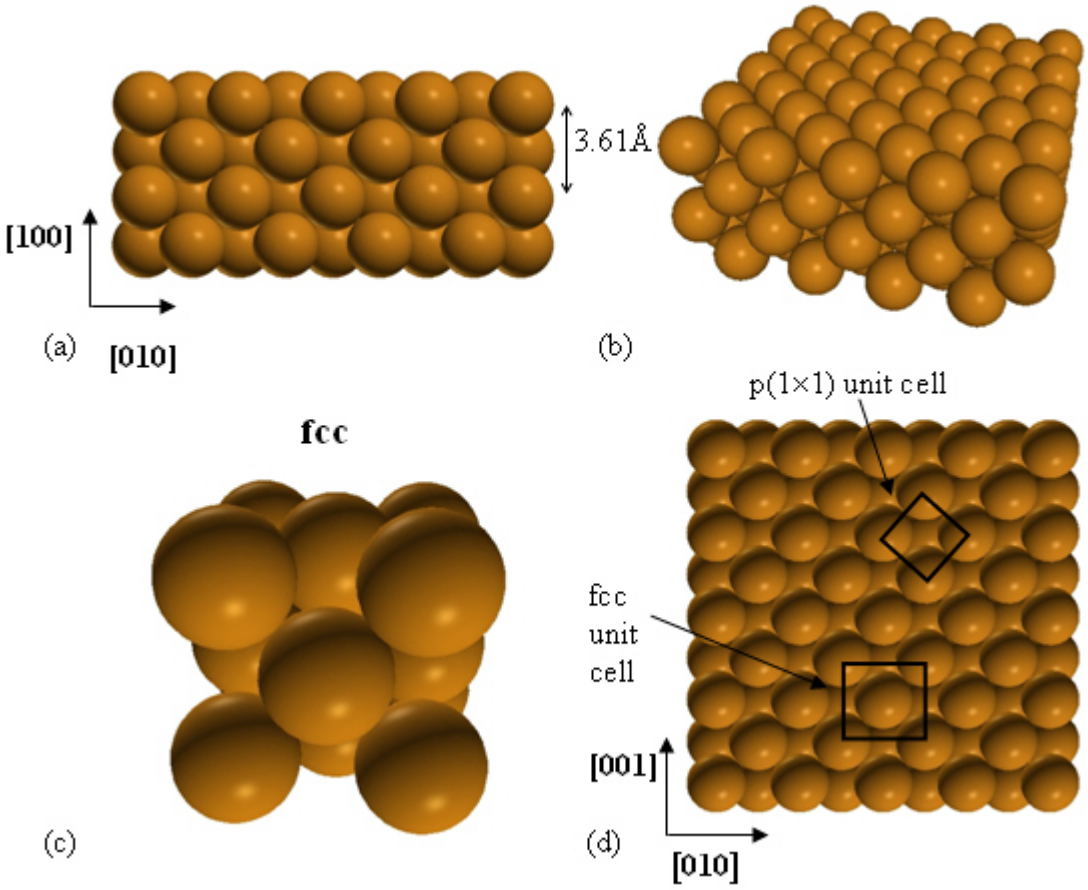

***Figure 3.1*:** The clean Cu(100) crystal structure. (a) Front view (001) plane showing the 3.61Å lattice constant, (b) perspective view, (c) fcc crystal structure and (d) Cu(100) crystal surface with fcc and p(1 × 1) unit cells shown.

For I(V) LEED experiments a single crystal copper sample, supplied by Surface Preparation Laboratory (SPL), of dimensions 10 × 10 × 1.5mm was oriented in the {100} direction to an accuracy of better than 0.5°. Four 0.25mm diameter holes were spark eroded into the corners of the crystal to aid sample mounting and to allow direct sample heating. A fifth 0.25mm hole was drilled in the side of the crystal for positioning of a chromel-alumel thermocouple for temperature measurement. The crystal was mounted on a high precision manipulator with polar rotation and surface tilt by suspending it between two stainless steel blocks with 0.25mm diameter tantalum wire secured through the four corner mounting holes. Temperatures of up 1000K were attained by passing a direct current through the tantalum support wires.

For LEED and STM experiments two strips of Ta were folded into incisions along the two sides of the crystal and spot welded to the Ta sample holder to secure the Cu(100) crystal (Figure 2.7).

The sample was cleaned by repeated cycles of argon ion bombardment at 2kV and annealing to 800K. The sample was deemed clean when no contaminants (e.g. oxygen at 509eV and carbon at 262eV) could be observed above the AES noise level and a sharp p(1 × 1) LEED pattern with low background intensity was observed. LEED I(V) spectra from the atomically clean surface were compared with accepted spectra in literature, compiled by Jona *et al.* [37]. Jona *et al.* tested the reproducibility of equivalent I(V) curves. They concluded that although equivalent I(V) curves may look very similar to one another, a quantitative analysis revealed that the energy scale might be shifted by as much as 10eV from experiment to experiment: the peak positions may fluctuate by ± 2.5eV and the peak intensities may vary by as much as 70%. Sn depositions were carried out using a water cooled Knudsen cell evaporator (WA technology).

3.2.2 LEED

The integral order I(V) spectra for the clean Cu(100) crystal are shown in Figure 3.2. The energy scale of the I(V) spectra is uncorrected for the effect of the inner potential [38]. The (1,0) integral beam represents the average of the symmetrically equivalent (1,0), (0,1), $(\bar{1},0)$ and the $(0,\bar{1})$ beams. Similarly the (1,1), (2,0) and (2,1) spectra represent averages of the symmetrically equivalent integral beams. It has been shown that such averaging reduces errors associated with the data-collection process such as incident beam misalignment [39].

The LEED I(V) data is used to check the cleanliness of the sample. In addition, for the different phases of the Sn/Cu(100) submonolayer surface alloys it is compared to theoretical models of these systems for structure determination. The equivalent beams in the different phases can also be compared to give additional information about the nature of the surface structure.

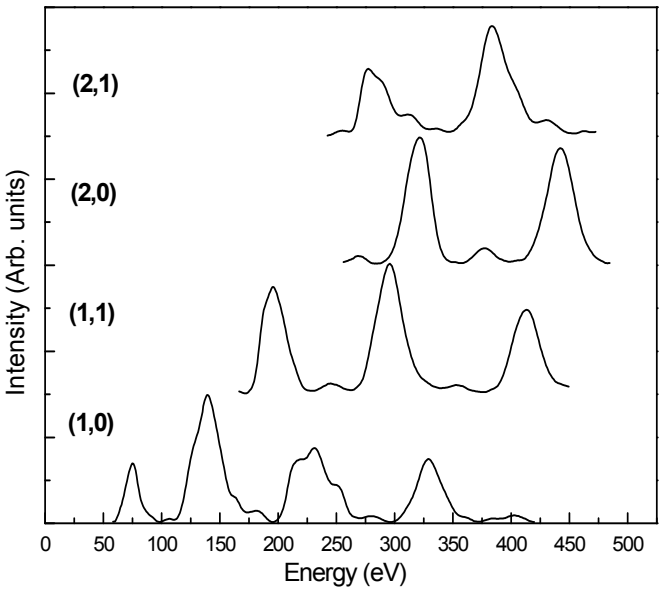

***Figure 3.2*:** LEED integral order I(V) profiles for the clean Cu(100) surface

(a) (b) (c)

Figure 3.3: LEED diffraction patterns for the clean Cu {100} surface at (a) 80.6eV, (b) 120.8eV and (c) 292.1eV.

Figure 3.3 shows the p(1×1) LEED diffraction patterns for the clean Cu(100) crystal. Using line profiles to measure the distance between the diffraction spots of the clean Cu diffraction pattern taken at various energies it is possible to calibrate the beam energy.

3.2.3 STM

The clean Cu(100) surface was the hardest surfaces to image with atomic resolution with the STM. Despite the multiple damping systems of the STM, well resolved images were only obtained when the air conditioning in the laboratory was

turned off. The STM images in Figure 3.4 clearly show the p(1 × 1) surface structure of the Cu(100) crystal surface.

(a) 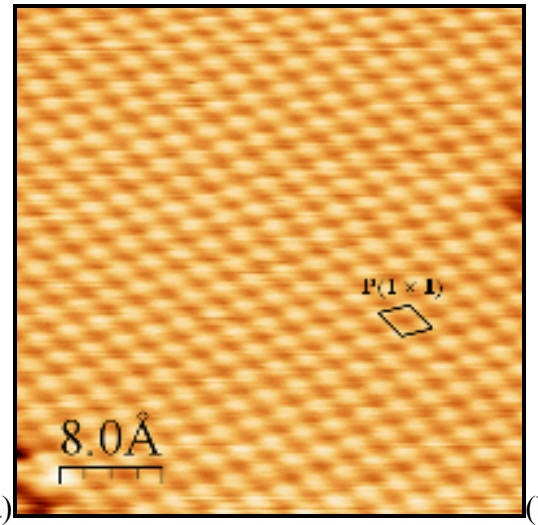

(b) 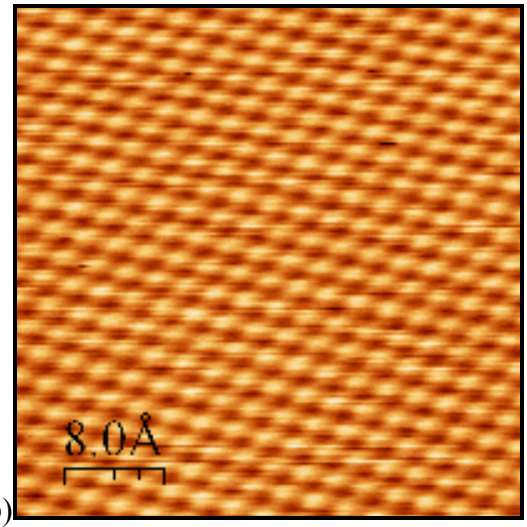

Figure 3.4 STM images of the clean Cu(100) crystal surface. (a) & (b) V_s = 0.01V, I_t = 5.8nA, 4nm^2.

The Fourier transform of the clean Cu(100) STM image is shown in Figure 3.5. The reciprocal lengths of 4.29 ± 0.1 nm^{-1} and 4.71 ± 0.1 nm^{-1} are recorded along the [011] and [01$\bar{1}$] directions respectively. These reciprocal lengths correspond to real space lengths of 0.237 ± 0.005 nm and 0.260 ± 0.005 nm. These measurements agree with the copper unit cell of length 0.255 nm.

(a) 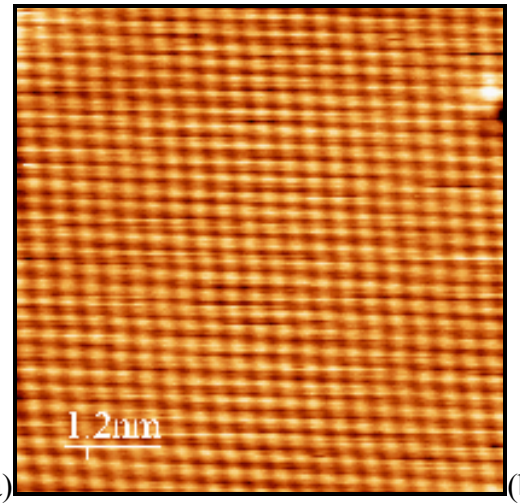

(b) 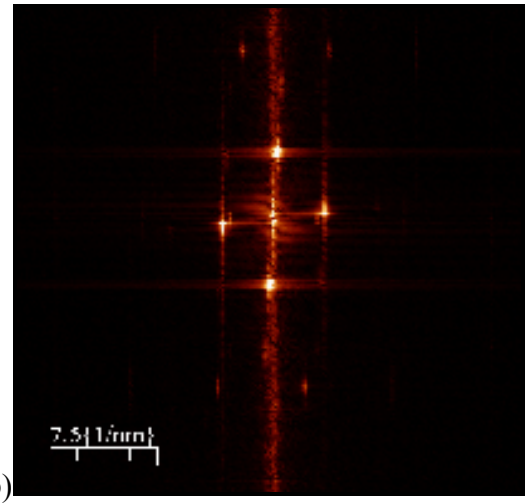

Figure 3.5: STM image of the clean Cu(100) surface, (a) V_s = 0.01V, I_t = 7.11nA, 6nm^2 and corresponding (b)Fourier transform, 4.29 ± 0.1 nm^{-1} and 3.87 ± 0.1 nm^{-1} recorded along the [011] and [01$\bar{1}$] directions.

3.2.4 Adsorption Sites

Figure 3.6 shows the possible sites for Sn adsorption on clean Cu(100) using the 12-fold metallic radii values 1.623Å for Sn and 1.278Å for Cu [Alcock 1990]. The metallic radius is defined as half the internuclear distance between neighbouring metal atoms in a metallic crystal. The 12-fold metallic radius is the average radius for the 12 nearest atoms in cubic close-packed metals. The surface alloy site (a) occurs where the Sn atom substitutes with the copper atom in the top layer lattice site positions. Site (b) the Sn atom occupies the four-fold hollow overlayer site at a height 0.227nm above the first layer copper atoms. Site (c) shows the Sn atom occupying a copper bridge site at a height dz of 0.26nm above the first layer copper atoms. Site (d) is a Sn atom atop a copper atom at a spacing of 0.29nm above the first layer copper atoms.

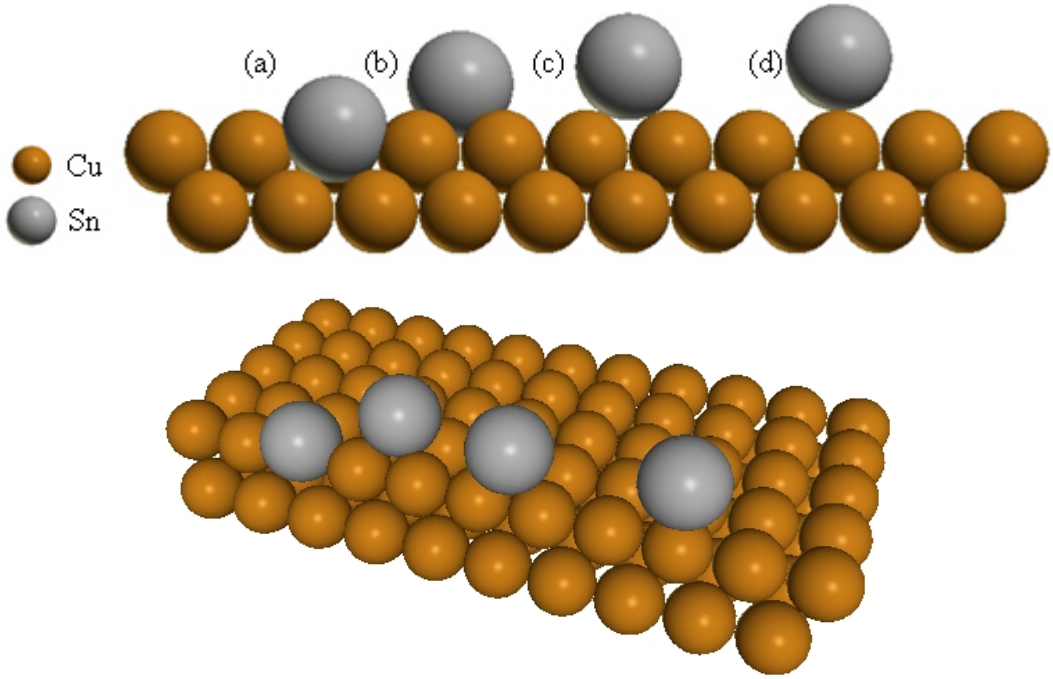

Figure 3.6: Possible sites for Sn adsorption on the clean Cu(100) surface. (a) Surface alloy, (b) four-fold hollow overlayer site, (c) bridge site and (d) atop the Cu atom.

3.3 Sn/Cu(100) Phase I:

3.3.1 Literature Review

Phase I, was first described by Argile and Rhead [6] as a “complex” diffraction pattern, and no model was proposed for the observed structure. However, the existence of antiphase domain wall boundaries was proposed based on the observed splitting of

the fractional order spots. The existence of several subdomains of the same structure within an area, smaller than the coherence length of the electron beam will result in spot splitting. When the subdomains form antiphase boundaries which are parallel and regularly spaced, a splitting of beams will take place in a direction determined by the orientation of the boundaries [14]. McLoughlin *et al.* [7] noted the diffraction pattern was based on a modified p(2 × 2) structure; the half order spots are split along the a_1 and a_2 reciprocal lattice vectors of the (1 × 1) substrate in the [011] and [$01\bar{1}$] directions; the four equivalent (1/2, 1/2) reflexes are split into four satellite spots while the (±1/2, n) and the (n, ±1/2) spots are split into two spots. Measurements taken from LEED images of the splitting of all beams relative to the reciprocal lattice vectors of the substrate indicate that the domain wall structure adopts a periodicity of 1/11th (0.09 ± 0.01) of the substrate reciprocal space lattice. This splitting is independent of both the beam energy and the Sn coverage up to the completion of phase 1.

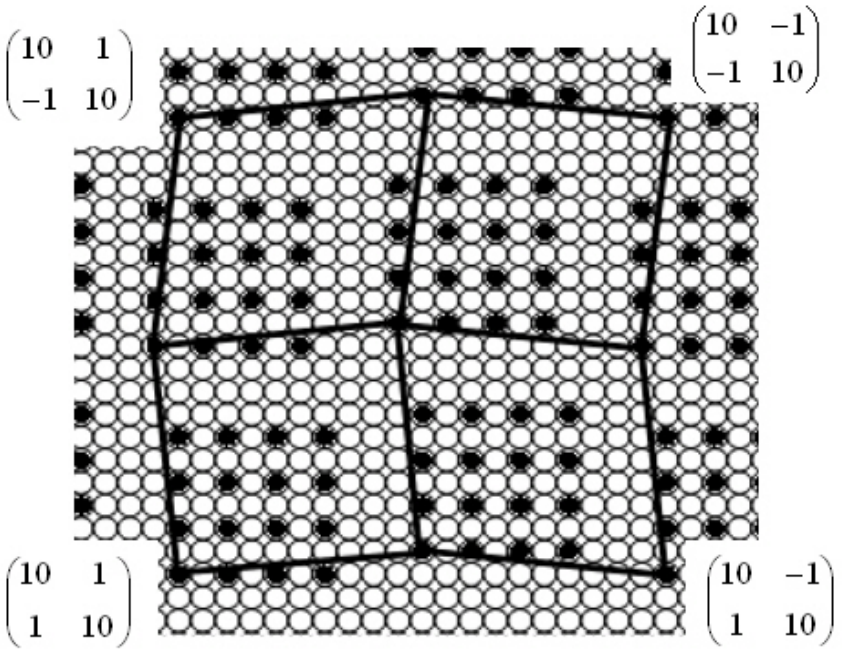

Figure 3.7: $\begin{pmatrix}10 & 1\\ 1 & 10\end{pmatrix}$"pinwheel" structure model for the Sn/Cu(100) Phase I model developed by Cafolla *et al.* [40]. Cu atoms are represented by the open circles and Sn atoms are represented by the filled in circles.

Cafolla *et al.* [40] developed a model based on a "pinwheel" structure consisting of four different superlattices separated by antiphase domain walls in both the [011] and

$[01\bar{1}]$ directions as shown in Figure 3.7. Each superlattice structure consists of nine p(2 × 2) cells. This "pinwheel" structure is expressed in terms of four different superlattices with different matrices based on combinations of a single matrix, in this case a $\begin{bmatrix} n & 1 \\ 1 & n \end{bmatrix}$ matrix, where n is an integer multiple of the substrate lattice spacing. Best agreement between simulated LEED patterns and experimentally observed LEED patterns was produced for n=10 $\begin{pmatrix} n & 1 \\ 1 & n \end{pmatrix}$ superlattice structure model. In this model the p(2 × 2) domains are separated by three rows of copper. Further STM study showed these domains separated by one, three or five rows of copper atoms in both the [011] and $[0\bar{1}\bar{1}]$ directions. These domains typically contained 16 Sn atoms arranged in a 4 × 4 square array although larger and smaller domains were observed.

3.3.2 LEED Results

The Phase I diffraction pattern is shown in Figure 3.8. The characteristic pattern of four equivalent (1/2, 1/2) reflexes split into four satellite spots and the (±1/2, n) and (n, ±1/2) spots split into two spots, is apparent. The integral and fractional order I(V) beam spectra for Phase I are shown in Figure 3.9. The I(V) data is collected for comparison with known spectra. A total of three fractional order beams and three integral order beams were measured. The I(V) data was measured in 1eV steps at normal incidence.

(a) 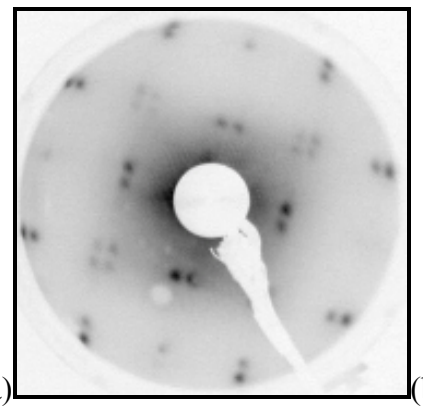 (b) 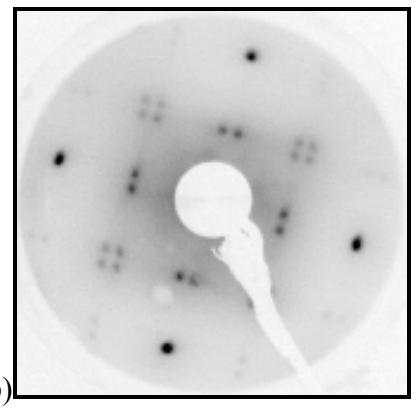

Figure 3.8: LEED diffraction patterns of the Sn/Cu(100) Phase I recorded at (a) 54eV and (b) 61eV respectively.

I(V) spectra from the (1/2, 1/2) beams were measured by recording individual spectra of the four (1/2, 1/2) spots and then taking an average of these spectra to represent the (1/2, 1/2) beam. The four individual beams and their average show very similar characteristics from 80-200eV. The split (1/2, 0) and (1/2, 0) beams also display similar characteristics from 50-200eV and the average beams are shown in Figure 3.9.

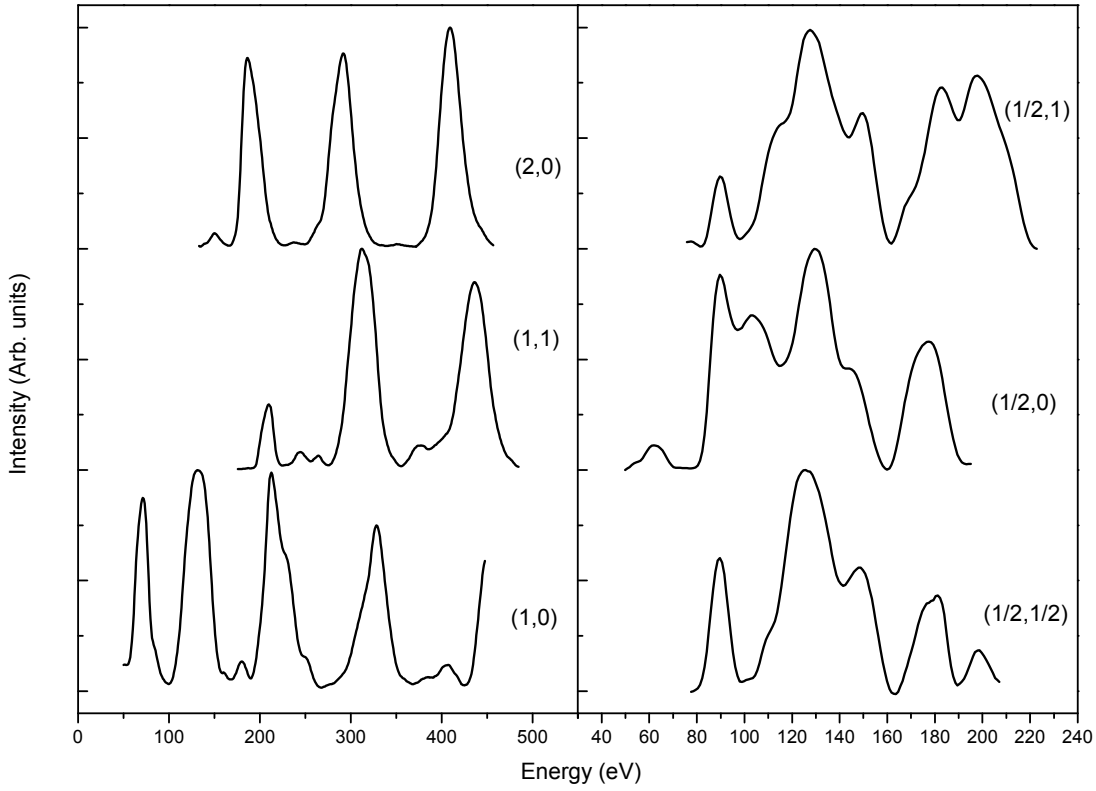

Figure 3.9: Integral and fractional order I(V) beam spectra of the Sn/Cu(100) Phase II LEED diffraction pattern, recorded at normal incidence.

3.3.3 STM Results

STM images of the Sn/Cu(100) Phase I surface recorded at room temperature are shown in Figure 3.10. Care must be taken when assigning the bright features in the STM images to atoms, as they only reflect variations in the electronic charge density, but for metals it is generally accepted that the maxima observed in an image correspond to the effective atomic positions [41]. Being mindful of this the p(2 × 2) arrangement of the Sn atoms is readily distinguished in these images.

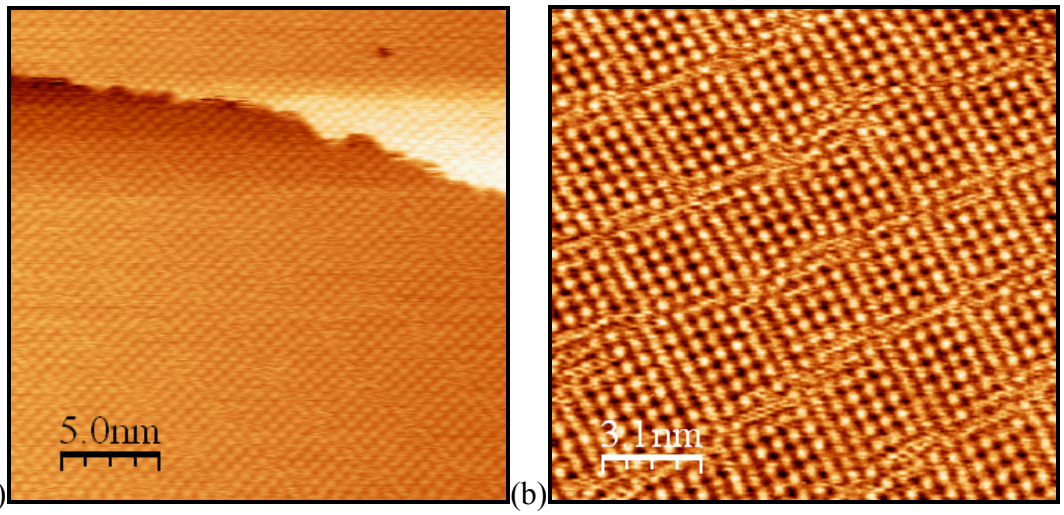

(a) (b)

Figure 3.10: STM images of the Sn/Cu(100) Phase I surface structure at θ_{Sn} =0.22 ± 0.02ML. (a) V_s = -0.005V, I_t = 3.0nA, 25nm^2. (b) V_s = -0.292V, I_t = 1.0nA, 15.5nm^2.

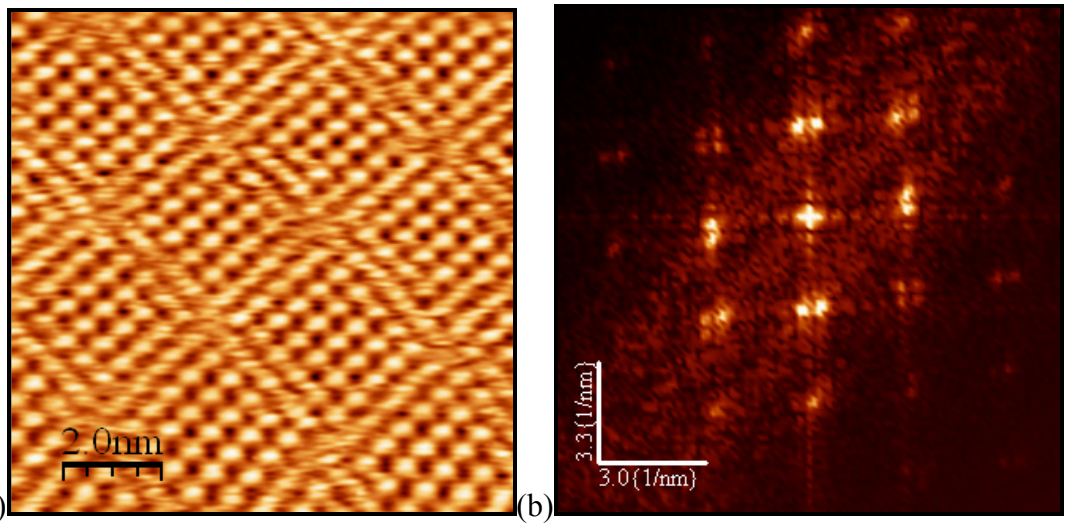

(a) (b)

Figure 3.11: (a) High resolution image STM image of the Sn/Cu(100) phase 1 surface structure at θ_{Sn} =0.22 ± 0.02ML, V_s = -0.005V, I_t = 3.0nA, 10nm^2 and corresponding Fourier transform, 2.06 ± 0.05 nm^{-1} and 1.94 ± 0.05 nm^{-1} along the [011] and [01$\bar{1}$] directions.

Figure 3.10(a) displays an 25 nm^2 area of the Sn/Cu(100) surface, recorded at a sample bias of -0.005V and a high tunnelling current of 3.0 nA, after room temperature deposition of θ_{Sn} = 0.22 ± 0.02 ML. This coverage is slightly greater than that required for the formation of an optimal Phase I structure of θ_{Sn} = 0.21ML, as determined from line profiles of the diffraction spots in the LEED data. Figure 3.10(b) displays a 15.5

nm^2 area of the Sn/Cu(100) surface, recorded at a sample bias of -0.005V and a tunnelling current of 1.0nA.

Only the tin atoms in the p(2 × 2) regions and not the Cu atoms are readily discernable. The Fourier transforms of the STM images were calculated [27] to compare the periodicity observed in the LEED diffraction patterns. The Fourier transform (Figure 3.11(b)) exhibits a distorted unit cell as a consequence of the drift in the STM image. The reciprocal lengths of 2.06 ± 0.05 nm^{-1} and 1.94 ± 0.05 nm^{-1} are recorded along the [011] and [01$\bar{1}$] directions respectively. These reciprocal lengths correspond to substrate lattice spacings of 1.91 ± 0.2 and 2.03 ± 0.2 unit cell spacings respectively. These measurements compare favourably with the expected p(2 × 2) lattice spacing of the unit cell when STM drift is taken into consideration. The four split spots which represent the (1/2, 1/2) split spots of the LEED diffraction pattern have reciprocal lengths of 0.34 ± 0.05 nm^{-1} and 0.34 ± 0.05 nm^{-1} recorded along the [011] and [01$\bar{1}$] directions respectively. These reciprocal lengths correspond to substrate lattice spacings of 11.71 ± 0.2 and 11.67 ± 0.2 unit cell spacings. The discrepancy between these values and those of the $1/11^{th}$ spacings measured from the LEED diffraction pattern may be due to the slightly higher Sn coverage in the STM sample compared to the LEED sample.

The small p(2 × 2) domains observed contain between 3 and 6 atoms per side. These Sn domains are separated by domain walls made up of Cu atoms. The atomic structure within most of the domain walls remains unresolved. The three types of domain walls reported by Cafolla *et al.* [40] are all observed in this work. These domain walls were measured (by Sn–Sn separation) to be 0.56 ± 0.02 nm, 0.95 ± 0.02 nm and 1.47 ± 0.02 nm. With a Cu-Cu separation of 0.255nm in the Cu unit cell, these widths are in good agreement with 1, 3 and 5 copper rows respectively The p(2 × 2) domains are laterally shifted relative to each other in the [011] and [01$\bar{1}$] directions with the magnitude of the lateral shift corresponding to a unit lattice vector of the copper substrate (0.255 nm). This shift results in an anti-phase alignment of the Sn atoms in neighbouring domains. Figure 3.12 (a) shows a 16 nm^2 STM image of the Sn/Cu(100) Phase I surface structure recorded at a sample bias of -0.292V and a tunnelling current of 1 nm^2. Figure 3.12(b) displays a line profile measured along the white inset shown in Figure 3.12(a)

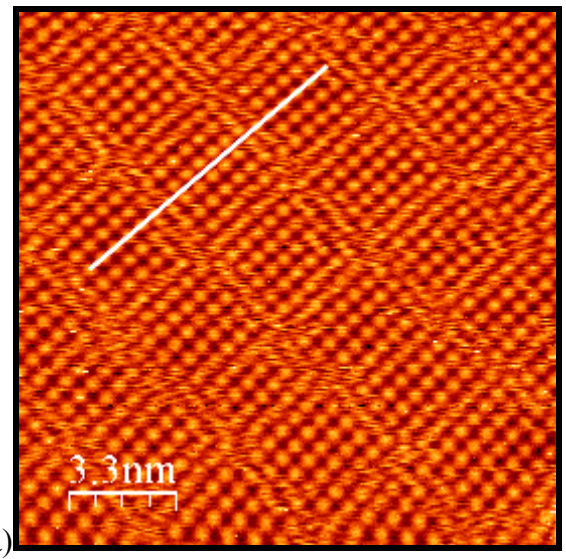

(a)

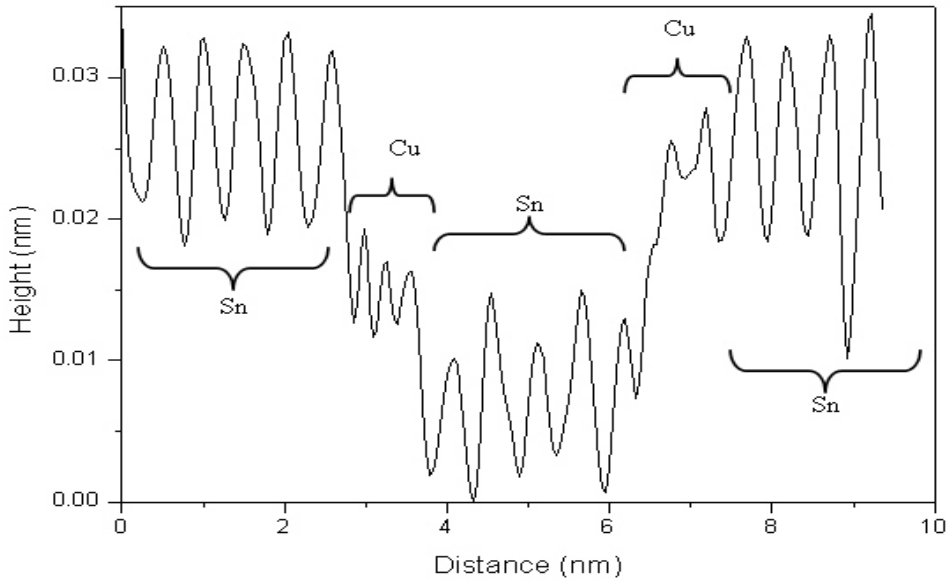

(b)

***Figure 3.12*:** (a) High resolution STM image of the Sn/Cu(100) Phase I surface structure at θ_{Sn} =0.22 ± 0.02ML. (a) V_s = -0.292V, I_t = 1nA, 16nm^2. (b) Line profile measured along the white inset shown in (a).

3.3.4 Conclusions

The model proposed here for Phase I is in agreement with the model proposed by Cafolla *et al.* [40]. The Sn atoms form a substitutional alloy with the Cu surface. Each Sn atom replaces a Cu atom from its original position. The Sn atoms form small domains of p(2 × 2) unit cell structure ideally containing 16 atoms in 4 x 4 square array,

however, arrays containing 3, 5 and 6 atoms are also observed. The different sized p(2 × 2) domains form a randomly ordered structure, where the Sn atoms within each domain are ordered but the anti-phase alignment of the domains with respect to each other is random. A consequence of this random ordering is that the width of the domain wall varies. A lateral and vertical displacement of the copper rows in the domain walls is observed. This is due to the elastic strain due to the accommodation of the larger metallic radii of the Sn atoms (1.64 Å) compared to the Cu atoms (1.275 Å). These domain walls were measured to be 0.562 ± 0.02 nm, 0.952 ± 0.02 nm and 1.47 ± 0.02 nm. These measurements are in good agreement with the width of 1, 3 and 5 rows of copper respectively with a slight vertical and lateral displacement.

A structure based solely on the domain wall structure of a single row of copper atoms separating the domains would have a Sn coverage of θ_{Sn} = 0.25 ML with 1 Sn atom for every 4 Cu atoms. The structures with domain walls consisting entirely of three or five copper have ideal coverages of θ_{Sn} = 0.11 ML and θ_{Sn} = 0.16 ML respectively. The LEED diffraction spots for Phase I are narrowest at a tin coverage of θ_{Sn} = 0.21 ± 0.02 ML. This indicates that the optimal structure predominantly consists of domain walls with three or five copper rows. Figure 3.13 shows the Sn/Cu(100) Phase I surface alloy model based on this study. Figure 3.14 shows the vertical and lateral displacement of Cu atoms in the domain walls of the Sn/Cu(100) Phase I surface alloy.

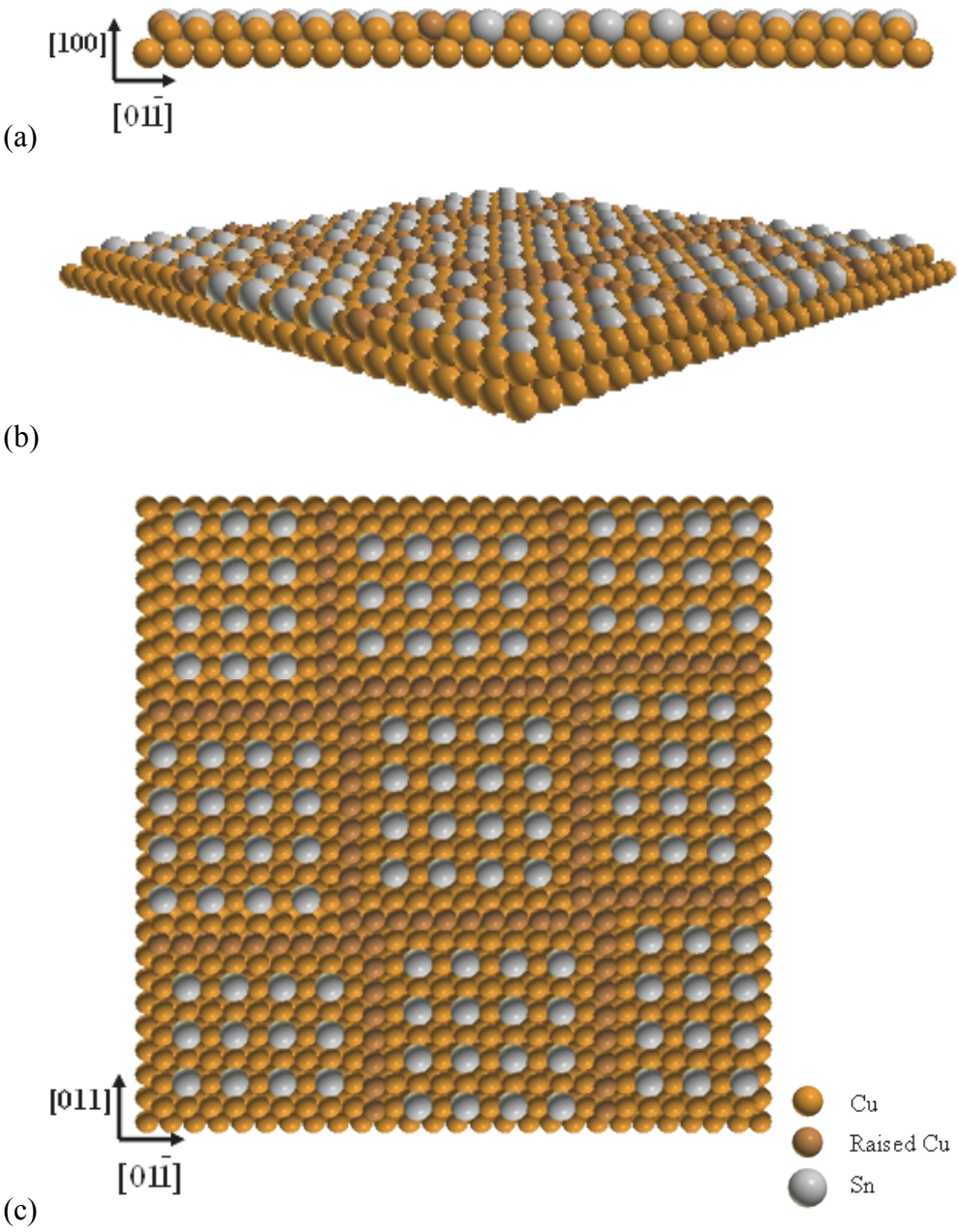

Figure 3.13: Sn/Cu(100) Phase I surface alloy model. (a) Front view (011) plane, (b) perspective view and (c) top view (100) plane.

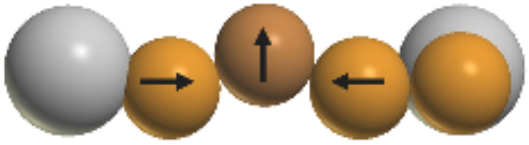

Figure 3.14: Model showing the lateral and vertical displacement of Cu atoms in the domain walls in the Sn/Cu(100) Phase I surface alloy model.

3.4 Sn/Cu(100) Phase II

3.4.1 Literature Review

The Phase II p(2 × 6) diffraction pattern is observed at a Sn coverage of ~ 0.4 ML. The Phase II diffraction pattern is simpler than the Phase I pattern, but an interpretation of the Phase II structure has proved to be difficult as explained below. Phase II was initially suggested by Argile and Rhead to consist of a p(2 × 6) structure with a rotated domain composed of a coincidence mesh with five Sn atoms occupying six copper interatomic spacings in the [01$\bar{1}$] direction This model, while consistent with the p(2 × 6) periodicity observed for Sn coverage of 0.42ML, when modelled by computer simulation [5] only produces weak (1/2, 1/2) beam intensities which is inconsistent with observation.

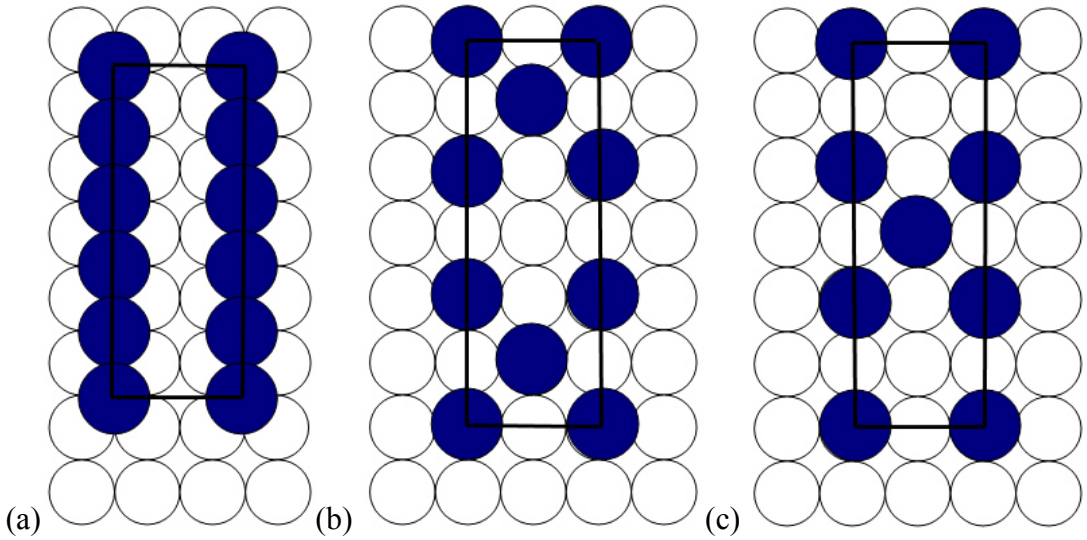

Figure 3.15: Sn/Cu(100) Phase II (a) Overlayer model by model Argile and Rhead (b) & (c) Surface alloy model by McLoughlin. Unit cells shown in black.

For this reason McLoughlin *et al.* [7] proposed alternative structures which reproduced the correct beam intensities in computer simulations. These models consisted of a mix of c(2 × 2)/p(2 × 2) structures, shown Figure 3.15. The first structure consists of domains of c(2 × 2) Sn/Cu(100) surface alloy of two unit cells width, separated by a p(2 × 2) unit cell, producing the required sixth order periodicity in the [011] and [01$\bar{1}$] directions for surface with two equivalent domains with a relative rotation of 90°. This model also predicts an Sn coverage of 0.42ML which however is

inconsistent with Auger studies [42] [7] which show Phase II forming at a lower Sn coverage. The second model is a p(2 × 6) unit cell consisting of a single c(2 × 2) unit cell with two p(2 × 2) unit cells on either side, yielding a coverage of 0.33ML, which offers a more reasonable explanation for the transition from Phase I, with a Sn coverage of 0.18ML, to Phase II at a Sn coverage of 0.33ML.

Recently Lallo *et al.* [9] reported the presence of a p2mg symmetry in the LEED pattern of this phase. Three models were proposed by Lallo *et al.* [9] (Figure 3.16) but were not confirmed using STM due to difficulty imaging the surface structure.

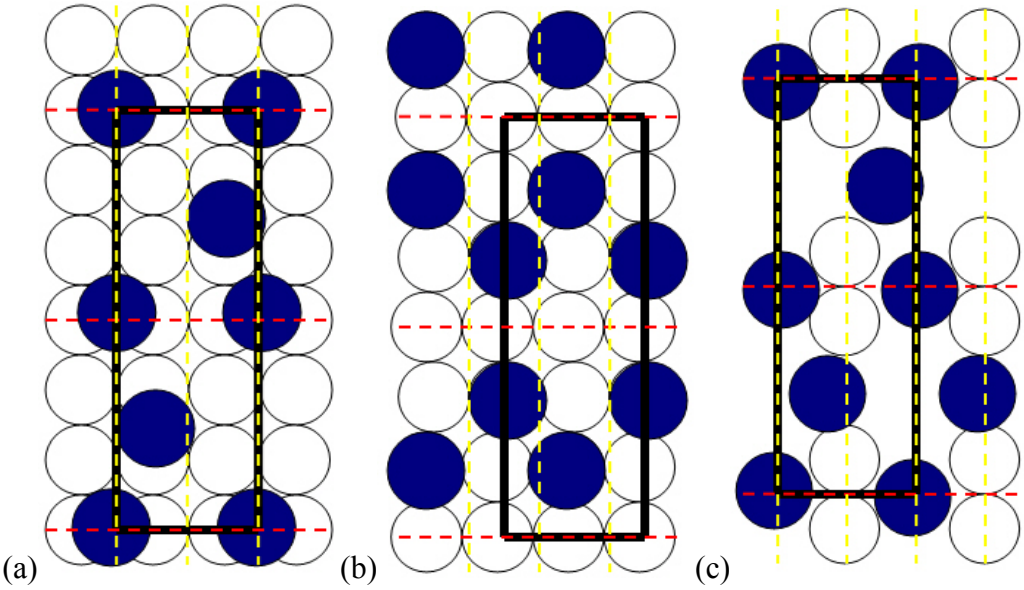

Figure 3.16:Sn/Cu(100) Phase II surface structure models proposed by Lallo *et al.* (a) Overlayer structure, (b) & (c) surface alloy. Unit cells shown in black, mirror and glide planes represented by the dashed red and yellow lines respectively.

3.4.2 LEED Results

LEED diffraction patterns taken of Phase II at 90 eV and 105 eV beam energy are shown in Figure 3.17. A higher intensity is observed in the (2/3, 1/2) and equivalent symmetry beams at 90 eV beam energy. The absence of the (0, 5/6) (0,-5/6) (5/6, 0) (-5/6, 0) Bragg spots is also noted. These reflections are absent over an energy range from 40 eV to 200 eV, outside of which the spots are either off screen or too close to be resolved. Missing Bragg spots in diffraction patterns are usually attributed to the presence of glide-reflection symmetry [14].

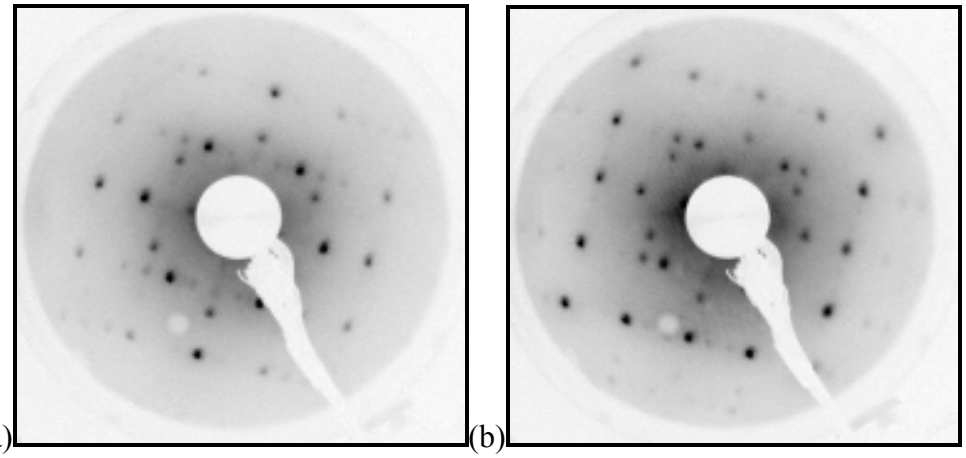

Figure 3.17: LEED diffraction pattern for Sn/Cu(100) Phase II taken at (a) 90eV and (b) 105eV. The absent Bragg reflections are noted.

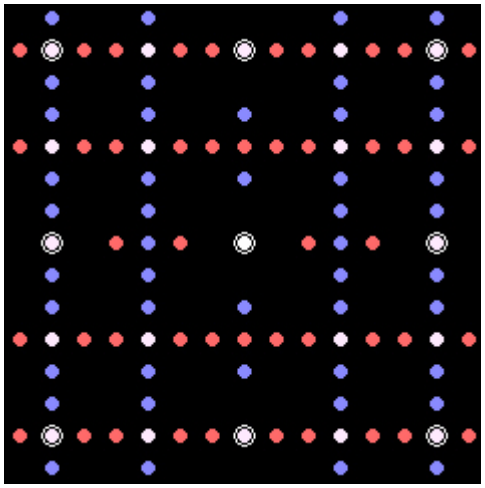

Figure 3.18: LEEDpat simulation of the Phase II diffraction pattern. Two unique domains are indicated in red and blue. The absent reflections are attributed to the presence of glide reflection symmetry.

Glide-reflection symmetry requires both reflection and translation along a mirror plane to be combined to bring the unit cell into coincidence with an initial geometrical configuration of the unit cell. The LEEDpat program [17] was used to confirm the presence of these glide-reflection symmetries, Figure 3.18 shows the LEEDpat simulation of the Phase II diffraction pattern. The program simulates the substrate symmetry constrained glide and mirror planes. There are two different glide plane space groups possible for the square p4mm substrate; p2gg and p2mg. The p2mg space group was found to be in agreement with the experimental results, showing systematic absences of the Bragg spots in the (0, 5/6) (0,-5/6) (5/6, 0) (-5/6, 0) and (0, 1/6) (0,-1/6) (1/6, 0) (-1/6, 0) positions. The p2gg space group revealed additional absences in the (0,

1/2) (0,-1/2) (1/2, 0) (-1/2, 0) which is inconsistent with the experimental diffraction pattern and so dismissed.

The integral and fractional order I(V) beam spectra for Phase II are shown in Figure 3.19. The I(V) spectra recorded at normal incidence are collected for comparison with known spectra and theoretical models. A total of six fractional order beams and three integral order beams were recorded.

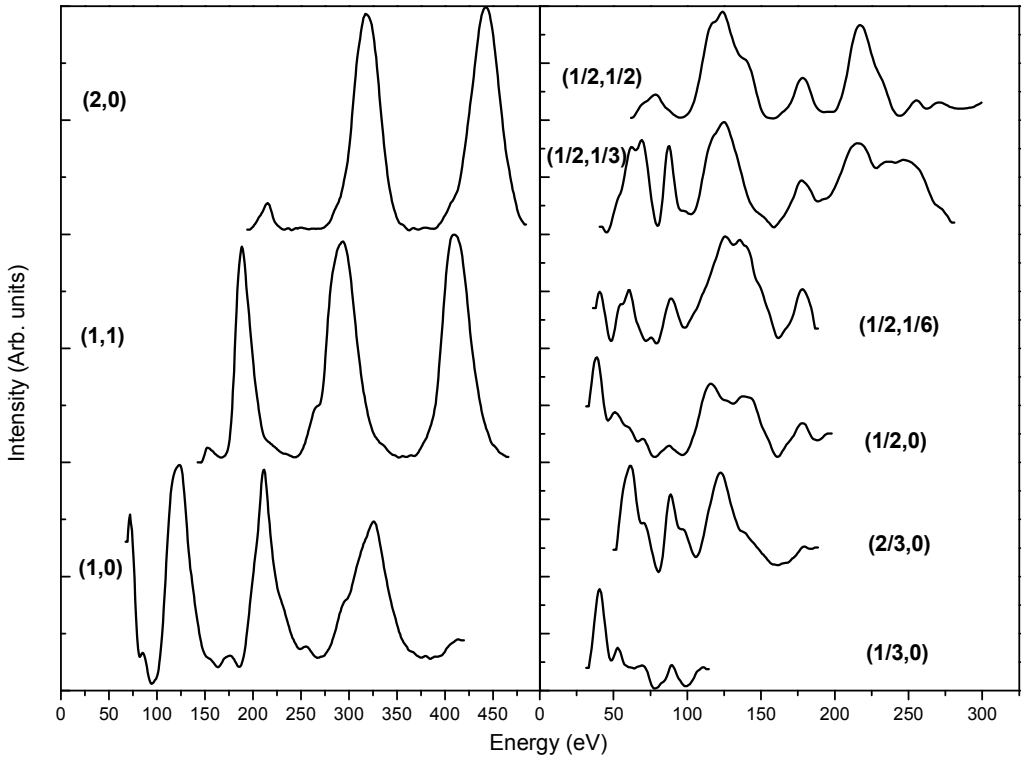

Figure 3.19: Integral and fractional order I(V) beam spectra for Sn/Cu(100) Phase II LEED diffraction pattern, recorded at normal incidence.

3.4.3 STM Results

As additional Sn is deposited onto the Phase I surface, sites in the copper domain walls are occupied by Sn atoms and the p(2 × 2) domains begin to extend in either the $[01\bar{1}]$ or the [011] direction and join up along domain walls. In STM images this new phase appears as double rows of Sn atoms with a dark spacing between each double row. Neighbouring double rows form a misaligned chevron structure and exhibit a p(2 × 6) unit cell as shown in Figure 3.20.

(a) 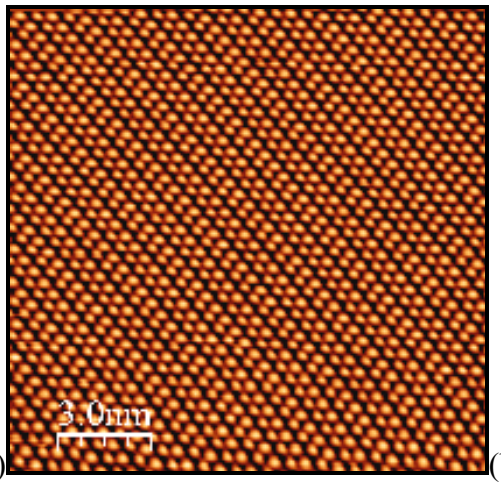

(b) 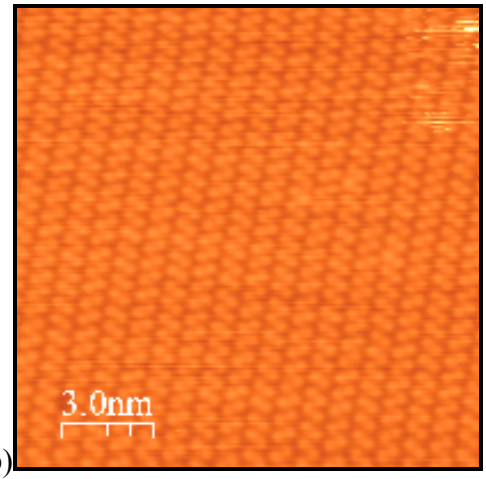

***Figure 3.20*:** STM images of the Sn/Cu(100) Phase II surface structure at θ_{Sn} = 0.33 ± 0.02 ML. (a) V_s = +0.1V, I_t = 1nA, 15nm^2. (b) V_s = +0.094V, I_t = 1.6nA, 15nm^2.

Surface structures imaged at different tunnel currents can often appear quite different as evident in Figure 3.20.

To understand the origin of the p(2 × 6) periodicity observed in the LEED diffraction patterns, the Fourier transforms of the STM images were computed [27]. Figure 3.21(a) shows an 8nm x 8nm STM image recorded at a sample bias of +0.094 V and a tunnel current of 1.60 nA. The corresponding Fourier transform is shown in Figure 3.21(b). The Fourier transform exhibits a distorted unit cell as a consequence of the drift in the STM image. Reciprocal lattice lengths of 0.64 ± 0.05 nm^{-1} and 1.96 ± 0.05 nm^{-1} are recorded along the [011] and [01$\bar{1}$] directions respectively. These reciprocal lengths correspond to substrate lattice spacings of 6.118 ± 0.2 and 2.003 ± 0.2. These measurements compare favourably to the expected 2 and 6 lattice spacing of the unit cell when drift is taken into consideration.

(a) 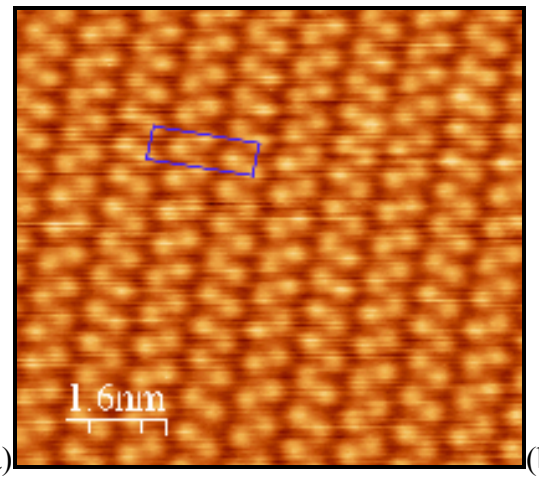

(b) 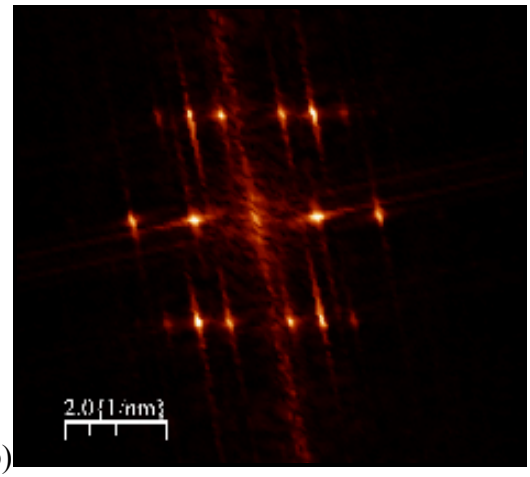

***Figure 3.21*:** Magnified STM image of the Sn/Cu(100) Phase II surface, θ_{Sn} =0.33 ± 0.02ML. (a) V_s = 0.094V, I_t = 1.6nA, 8nm^2 and the corresponding (b) Fourier transform, 0.64 ± 0.05 nm^{-1} and 1.96 ± 0.05 nm^{-1} recorded along the [011] and [01$\bar{1}$] directions.

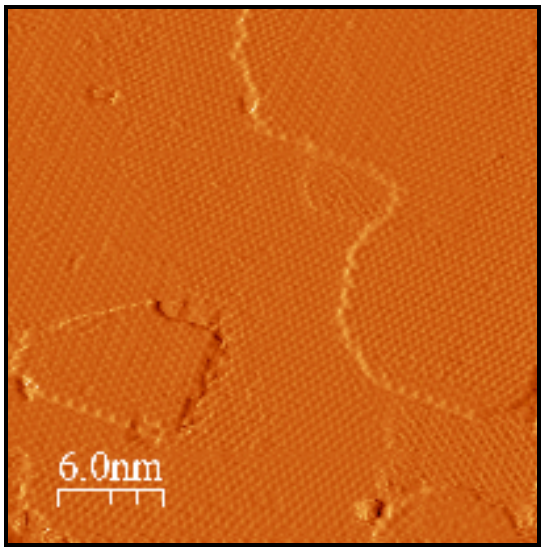

Figure 3.22: Derivative enhanced STM image, showing occasional island formation, V_s = -0.1V, I_t = 1.0nA, 30nm^2

The presence of occasional islands is noted on the surface in this phase, as shown Figure 3.22, and these island formations are not well ordered. These islands indicate the possibility that the Cu atoms displaced by Sn deposition can diffuse across the surface to add to the either the step edges or provide the additional Cu to form these islands [43].

3.4.4 Conclusion

The STM images reveal the Sn atoms forming a p(2 × 6) unit cell. The LEED data is consistent with a p2mg space group. The glide plane symmetries are distinguished by the missing Bragg spots at 1/6 and 5/6 positions in the LEED diffraction pattern. A new model is proposed for this structure and is shown in Figure 3.23. The p2mg space group restricts the positions of the Sn atoms in this model to conform to the mirror and glide plane symmetry which is indicated on the model by the broken lines. These restrictions were not applied to previous models and provide an explanation as to why they were unsuccessful in modelling the experimental LEED I(V)

data [44]. The optimum coverage for this phase is reached at θ_{Sn} = 0:33 ML, with 4 Sn atoms per 12 Cu atoms in the unit cell.

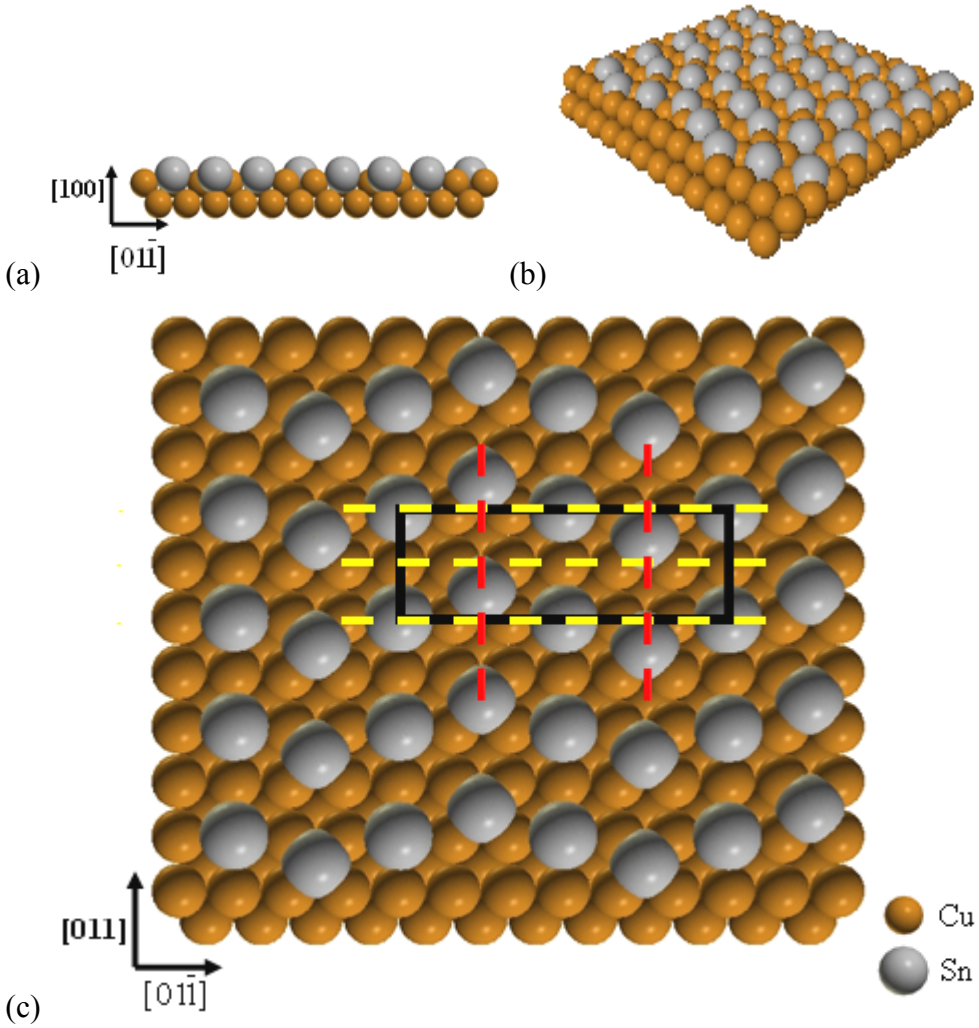

***Figure 3.23*:** Sn/Cu(100) Phase II surface alloy model. (a) Front view (011) plane, (b) perspective view and (c) top view (100) plane. Unit cell shown in black, mirror and glide planes represented by the dashed red and yellow lines respectively.

A uniform Cu substrate top layer is shown in this model. It is noted however that not all the Sn atoms occupy substitutional alloy sites in this model. Previous normal incidence X-ray standing wave (NIXSW) analysis [45] indicated only slightly different bonding environments for the Sn atoms. STM images did not indicate any height difference between the rows of Sn atoms. The formation of occasional islands on the surface in this phase, suggests further adjustment in the top layer of Cu atoms occurs to allow the Sn atoms to be accommodated into substitutional surface alloy sites at these positions.

3.5 Phase I – Phase II transition

3.5.1 LEED Results

LEED diffraction patterns taken for Sn coverage ~ 0.29ML ± 0.02ML are shown in Figure 3.24. These images show the existence of both Phase I and Phase II. The four split (1/2, 1/2) spots and the split (0, 1/2) spots, characteristic of the Phase I diffraction pattern are observed. The (0, 1/3), (0, 2/3), (1/2, 1/3) and (1/2, 2/3) spots and the absence of the (0, 1/6) and (0, 5/6) spots, characteristic of the Phase II diffraction pattern are noted. This confirms the coexistence of large domains of both phases on the crystal surface.

(a) 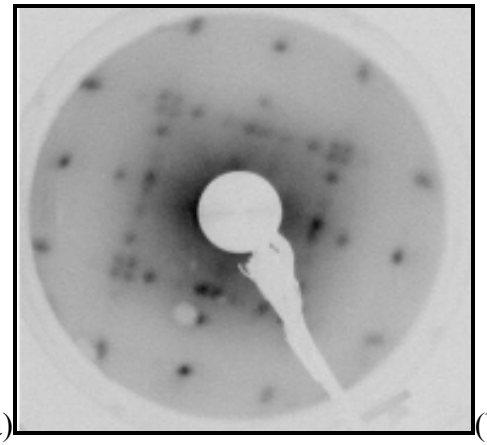 (b) 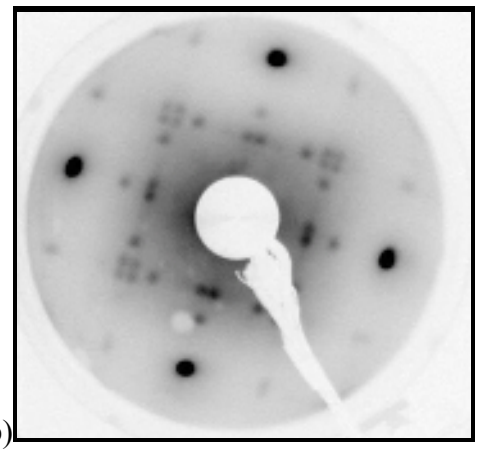

Figure 3.24: LEED diffraction patterns for the transition between Sn/Cu(100) Phase I and Phase II θ_{Sn} =0.29 ± 0.02ML, taken at (a) 57 eV and (b) 64 eV

3.5.2 STM Results

As additional Sn is deposited onto the Phase I surface, sites in the copper domain walls are occupied by Sn atoms. The domains begin to extend in the [01$\bar{1}$] and the [011] direction and join up along domain walls. This is shown in Figure 3.25 and Figure 3.26.

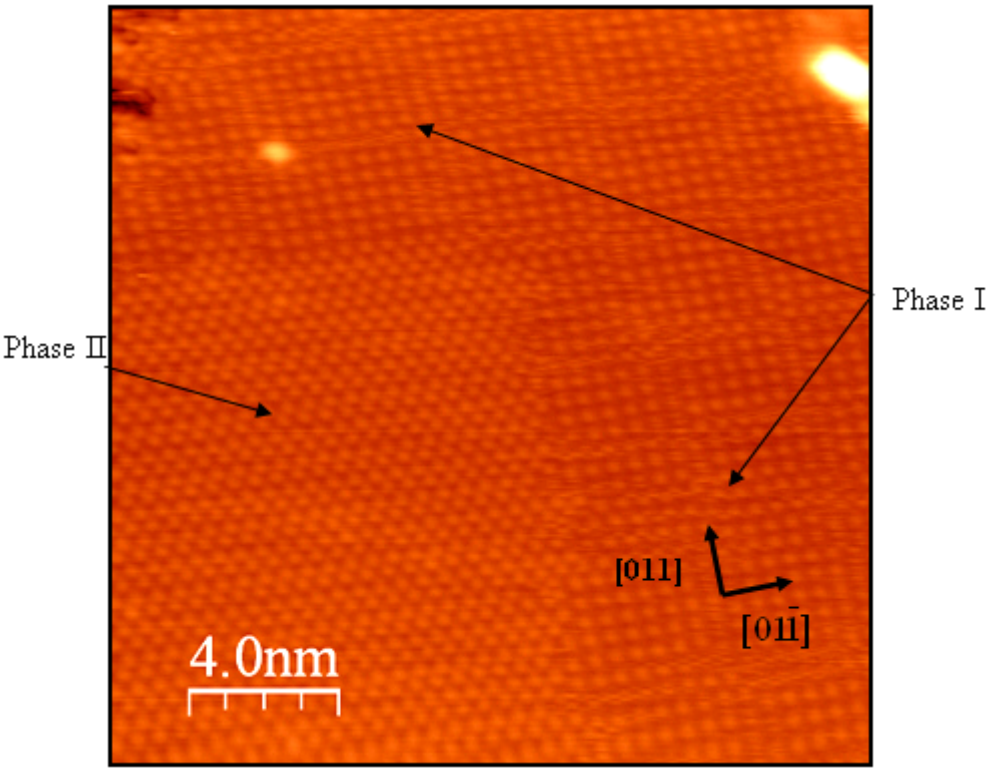

Figure 3.25: STM image of the transition from Phase I to Phase II at θ_{Sn} =0.29 ± 0.02ML. V_s = +1.0V, I_t = 1.0nA, 20nm^2.

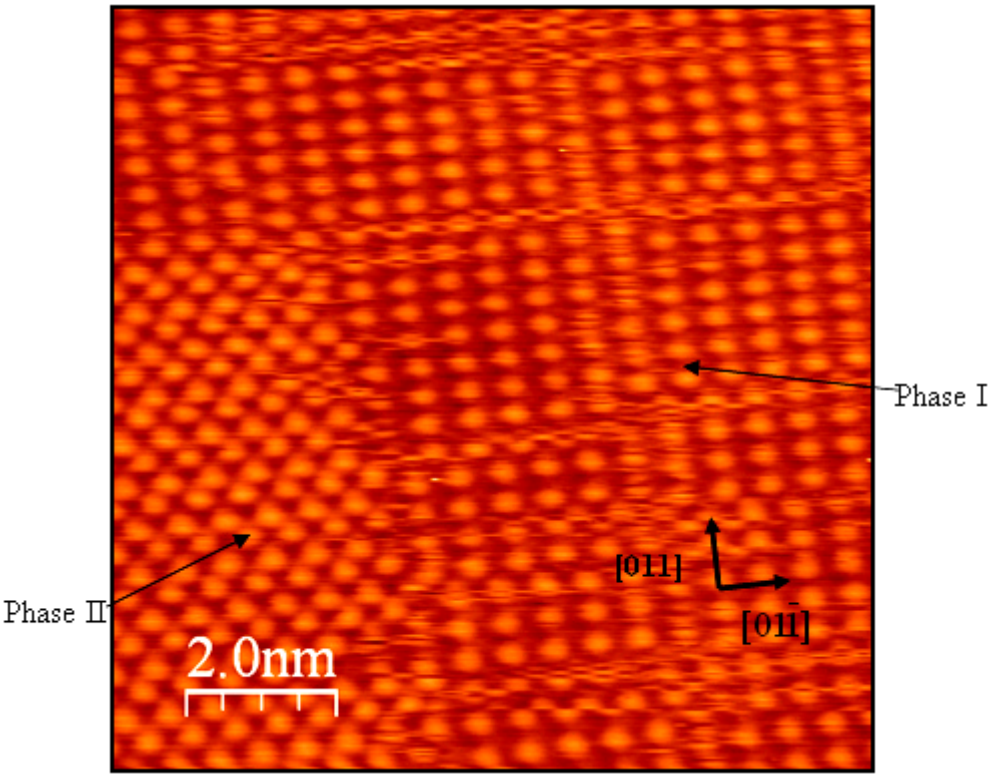

Figure 3.26: Magnified STM image of the transition from Phase I to Phase II at θ_{Sn} =0.29 ± 0.02ML. V_s = +1.0V, I_t = 1.0nA, 10nm^2.

Small islands are observed on the surface in Figure 3.27. There is a possibility that the Cu atoms displaced by Sn deposition can diffuse across the surface to add to the

step edges and provide the additional Cu to form theses islands [43]. Further evidence of this may be shown in Figure 3.28, where it is observed that the step edges are the last areas of the surface to make the transition to next phase following the deposition of additional Sn to the surface.

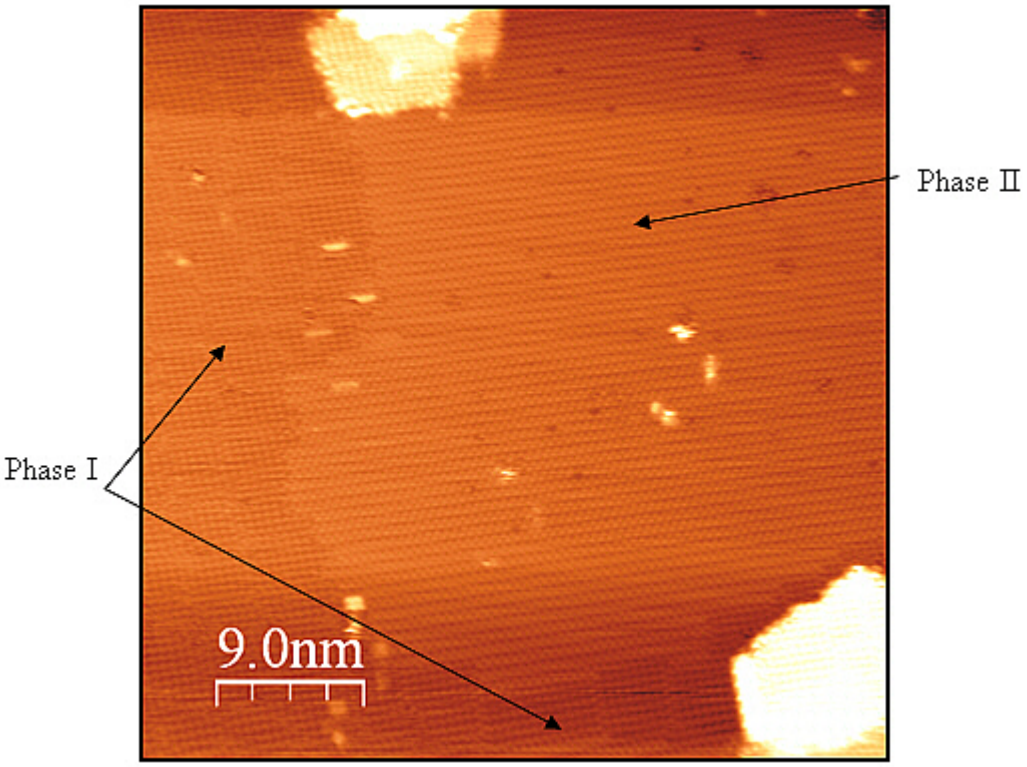

Figure 3.27: STM image of the transition from Phase I to Phase II at θ_{Sn} =0.29 ± 0.02ML. V_s = -0.076V, I_t = 1.94nA, 45nm^2. Island formation on the surface is noted.

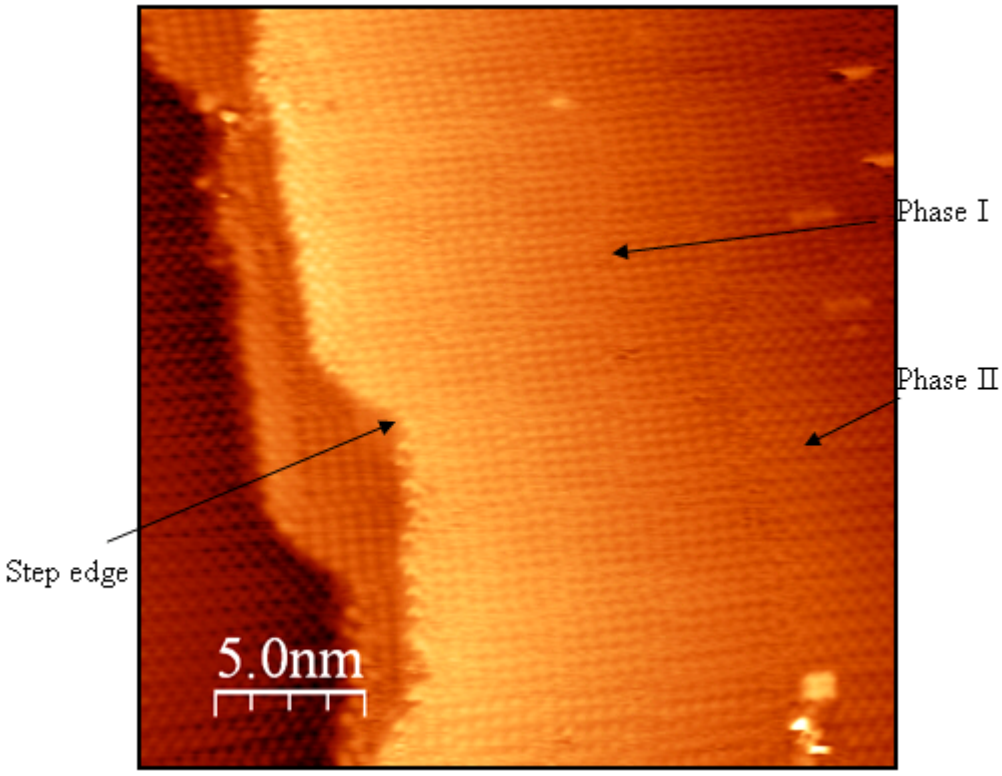

Figure 3.28: STM image of the transition from Phase I to Phase II at θ_{Sn} =0.29 ± 0.02ML. V_s = -0.076V, I_t = 1.94nA, 25nm^2. The step edges are the last areas of the surface to complete the transition to the nest phase.

3.6 Sn/Cu(100) Phase IIH

3.6.1 Literature Review

A new phase appearing between Phase II and Phase III was recently reported by Martinez-Blanco *et al.* [8] based on LEED measurements. This new phase is observed over a very narrow range of Sn coverage at ~0.45 ML and produces a LEED diffraction pattern with a $\begin{pmatrix} -4 & 2 \\ 0 & 4 \end{pmatrix}$ structure. The LEED images exhibit diffracted beams which are not consistent with diffraction spots present in either Phase II or Phase III. This new phase has been designated as Phase IIH or higher Phase II. This phase has not been observed in isolation from either Phase II or Phase III but always appears as a mixed phase, which may explain why it was not reported earlier. Yuki Nara *et al.* [46] published STM studies of this surface structure in late 2007 followed by Lallo *et al.* [9] in 2008. The LEED and STM work reported in this thesis was performed before these papers were published. The surface structure models of Sn/Cu(100) Phase IIH proposed by Yuki Nara *et al*. and Lallo *et al.* are shown in Figure 3.29

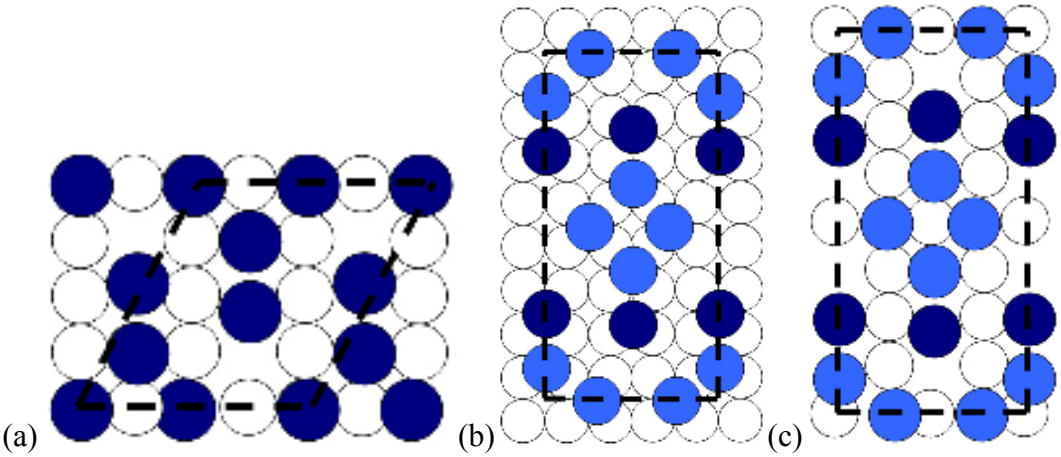

Figure 3.29: Surface structure models of Sn/Cu(100) Phase IIH (a) surface alloy Yuki Nara *et al.*, (b) & (c) Lallo *et al.* overlayer and surface alloy structure respectively. Unit cells shown in black. Dark blue circles represent Sn atoms vertically displaced (~ 0.05 Å) compared to the lower light blue circles.

3.6.2 LEED Results

Diffraction patterns showing evidence for the new phase recorded for Sn coverages between those of Phase II and III are shown in Figure 3.30 and Figure 3.32. The new Phase IIH co-exists with both Phase II and Phase III in a Sn coverage range of approximately 0.42 – 0.48 ML.

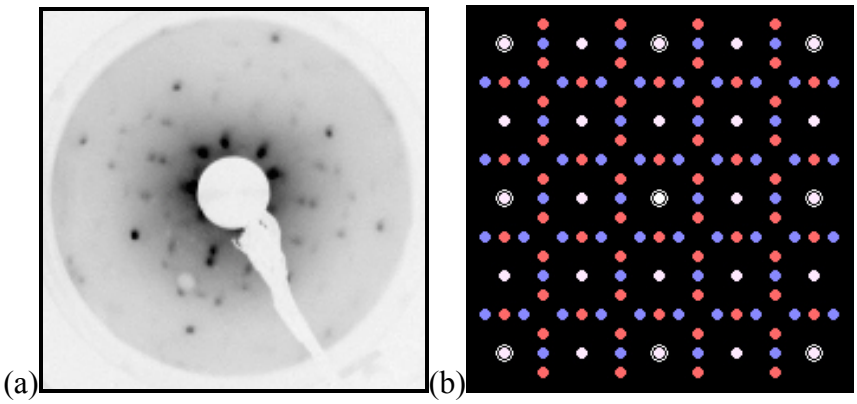

Figure 3.30**:** (a) LEED diffraction pattern of the Sn/Cu(100) Phase IIH surface recorded at 55eV. (b) LEEDpat simulated diffraction pattern. Two unique rotated domains indicated in red and blue.

The investigation of Phase IIH is hampered by the high background intensity and the concurrent formation of the Phase III. The three integral order I(V) beam spectra, measured in 0.5eV steps at normal incidence for Phase IIH are shown in Figure 3.31. The I(V) data is collected for further comparison with simulations of the surface

structure. The fractional order beams proved too weak compared to the high background intensity to be measured.

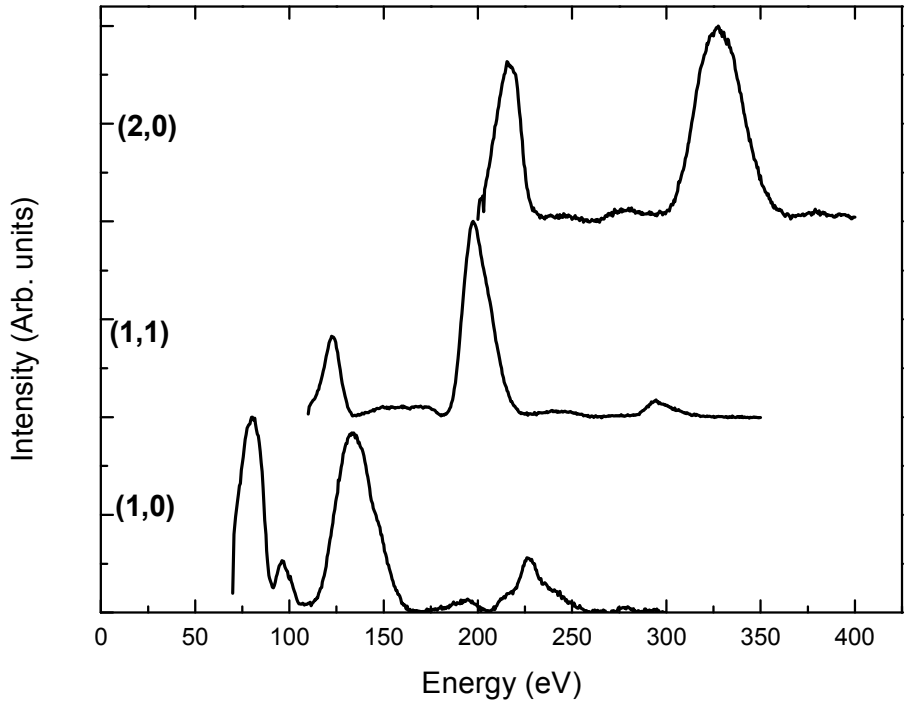

Figure 3.31: Integral order I(V) spectra for Phase IIH recorded at normal incidence.

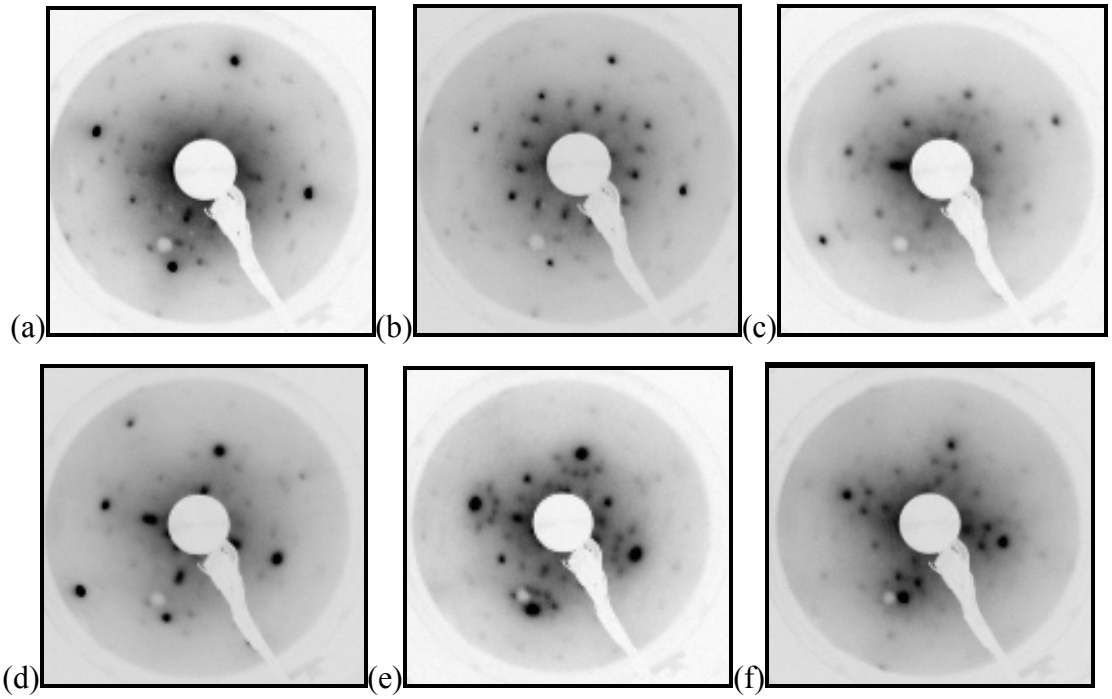

Figure 3.32**:** Further LEED diffraction patterns for the Sn/Cu(100) Phase IIH surface structure, recorded at (a) 80eV, (b) 88eV, (c) 107eV, (d) 117eV, (e) 128eV and (f) 142eV.

Further LEED diffraction images, Figure 3.32, show that fractional order beams are observed over a wide range of energies (50-200eV). However due to the coexisting diffraction patterns, high density of spots and high background intensity no useful I(V) data was measured for the fractional order beams of this phase.

3.6.3 STM Results

This new phase is designated phase IIH, or higher phase II because it co-exists between phase II and phase III. This co-existence is the reason it was overlooked in previous LEED studies. The unit cell of the Phase IIH structure maintains the same alignment relative to the bulk Cu lattice as that of Phase II as seen by the alignment of the Bragg spots in the LEED images. As the Phase III begins to form, narrow striped regions are observed in the STM images. The striped regions are observed to form between domains of lower coverage Phase II and Phase IIH structures and also between domains of the phase IIH structure. The unit cell of structure in these striped regions is rotated by 45° relative to the unit cell of the Phase II and IIH unit cell. Figure 3.33 and Figure 3.34 show STM images where the three surface phases are imaged simultaneously.

The three phases II, IIH and III are imaged in Figure 3.33 and Figure 3.35, co-existing in areas as small as $15nm^2$ which is well within the coherence length of the electrons from the LEED [12].

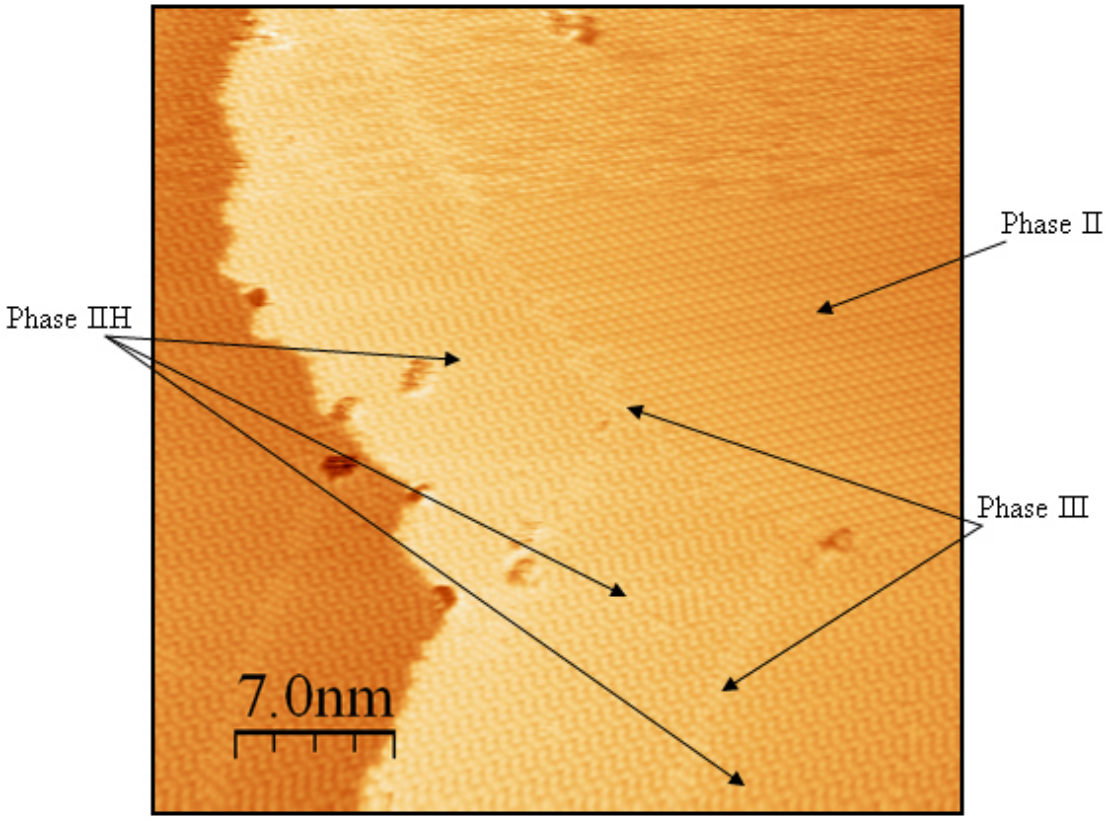

Figure 3.33: STM image of the Sn/Cu(100) Phase IIH surface structure at θ_{Sn} =0.37 ± 0.02ML. V_s = -0.052V, I_t = 0.717nA, 35nm^2. Large domains of both Phase II and Phase IIH are observed as well as the formation of Phase III at the boundaries of these domains.

Reciprocal lattice lengths of 1.699 ± 0.05 nm^{-1} and 4.284 ± 0.05 nm^{-1} are recorded along the [011] and [01$\bar{1}$] directions respectively from the Fourier transform (Figure 3.36) of the STM image. These reciprocal lengths correspond to substrate lattice spacings of 4.616 ± 0.2 and 1.83 ± 0.2. These measurements compare favourably to the expected $\begin{pmatrix} -4 & 2 \\ 0 & 4 \end{pmatrix}$ structure lattice spacing of the unit cell when drift is taken into consideration.

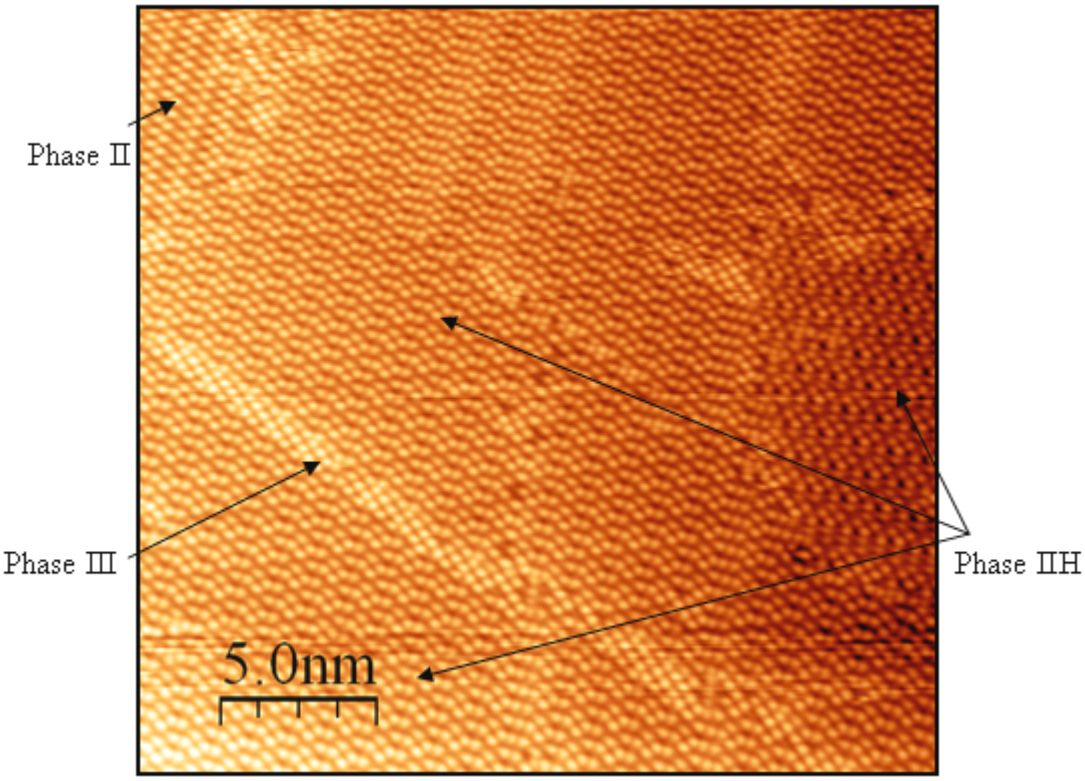

Figure 3.34: STM image showing large domains of Phase IIH, θ_{Sn} =0.37 ± 0.02ML taken at V_s = -0.052V, I_t = 0.778nA, 25nm^2. To the right of the image two Phase IIH domains have formed rotated 90° with respect to each other. Again Phase II and Phase III structure can be observed in this image.

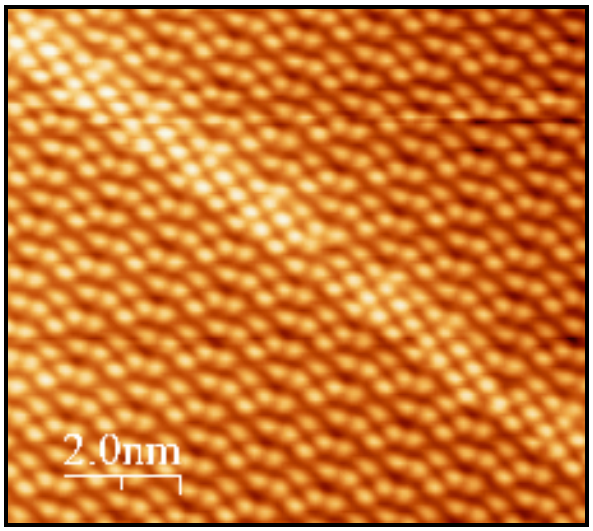

Figure 3.35: Magnified STM image showing Phase III formation at the boundary between two Phase IIH domains. V_s = -0.052V, I_t = 0.778nA. The Phase III unit cell is rotated 45° relative to the lower Phase IIH unit cell.

(a) 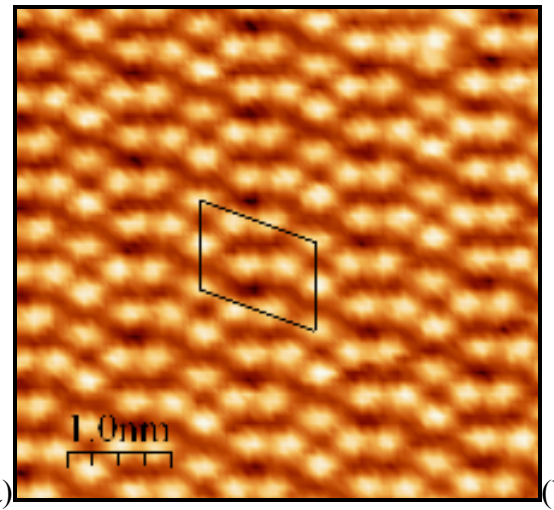

(b) 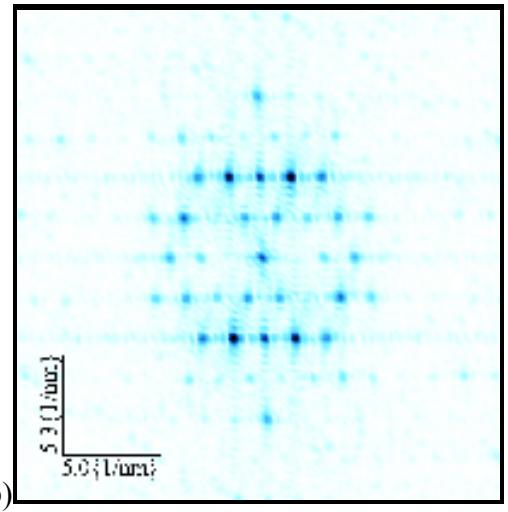

Figure 3.36: (a)High resolution STM image showing the $\begin{pmatrix} -4 & 2 \\ 0 & 4 \end{pmatrix}$ unit cell for Phase IIH, taken at V_s = -0.052V, I_t = 0.778nA and (b) the corresponding Fourier transform.

The presence of islands is again noted on the surface in this phase as shown in Figure 3.37. The formation of these islands is not well ordered, the sides and corners of the islands are rough and rounded. Multiple domains rotated 90° with respect to each other are formed on the island surface. There is a possibility that the Cu atoms displaced by Sn atoms forming a surface alloy can diffuse across the surface to add to the step edges and provide the additional Cu to form theses islands [43].

(a) 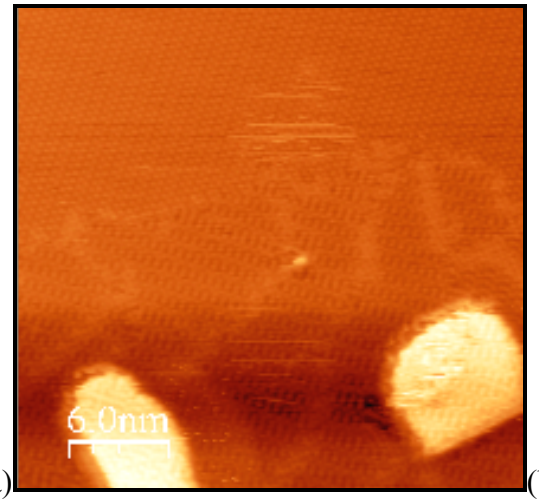

(b) 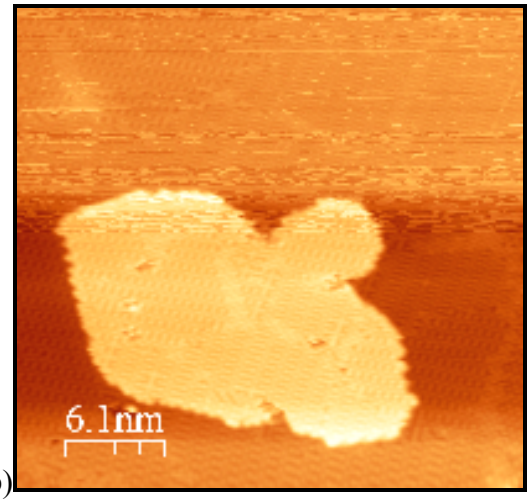

***Figure 3.37*:** STM images showing coexisting areas of Phase II, IIH and III, taken at θ_{Sn} =0.37 ± 0.02ML, (a) V_s = -0.09V, I_t = 2.0nA 30nm^2 and (b) V_s = -0.1V, I_t = 1.076nA 30nm^2. The presence of islands is also noted.

3.6.4 Conclusions

As shown in the previous section this new phase forms for a narrow range of Sn coverage between phase II and phase III. It was not possible to prepare a surface exhibiting only the Phase IIH structure; at best domains of Phase IIH, with dimensions of approximately 25 nm, could be formed. Annealing these surfaces to ~450K and cooling back to room temperature did not increase the domain size. A model of the IIH structure based on an interpretation of the LEED and STM data is presented in Figure 3.38. Measurements from LEED images indicate a $\begin{pmatrix} -4 & 2 \\ 0 & 4 \end{pmatrix}$ unit cell and this is confirmed by the unit cell dimensions measured in the STM images.

The optimal coverage for the formation of phase II has been reported in the literature at θ_{Sn} = 0.37 ML [7] and θ_{Sn} = 0.42 ML [5] [6] [42]. This inconsistency can be attributed to the coexistence of this new phase. Optimum coverage for the phase IIH structure based on the model proposed in Figure 3.38 is θ_{Sn} = 0.375ML, with 6 Sn atoms per 16 Cu atoms in the unit cell as compared to θ_{Sn} = 0.45ML [8] proposed in the literature. The early formation of phase III coexisting between bordering phase II domains, phase IIH domains and between different domains of phase II and phase IIH explains the short coverage range over which phase IIH is observed. The early appearance of phase III coexisting with the phase IIH domains can be explained by low packing efficiency of the phase IIH structure where the need to accommodate the additional Sn is best served in the stable phase III modified c(2 x 2) reconstruction.

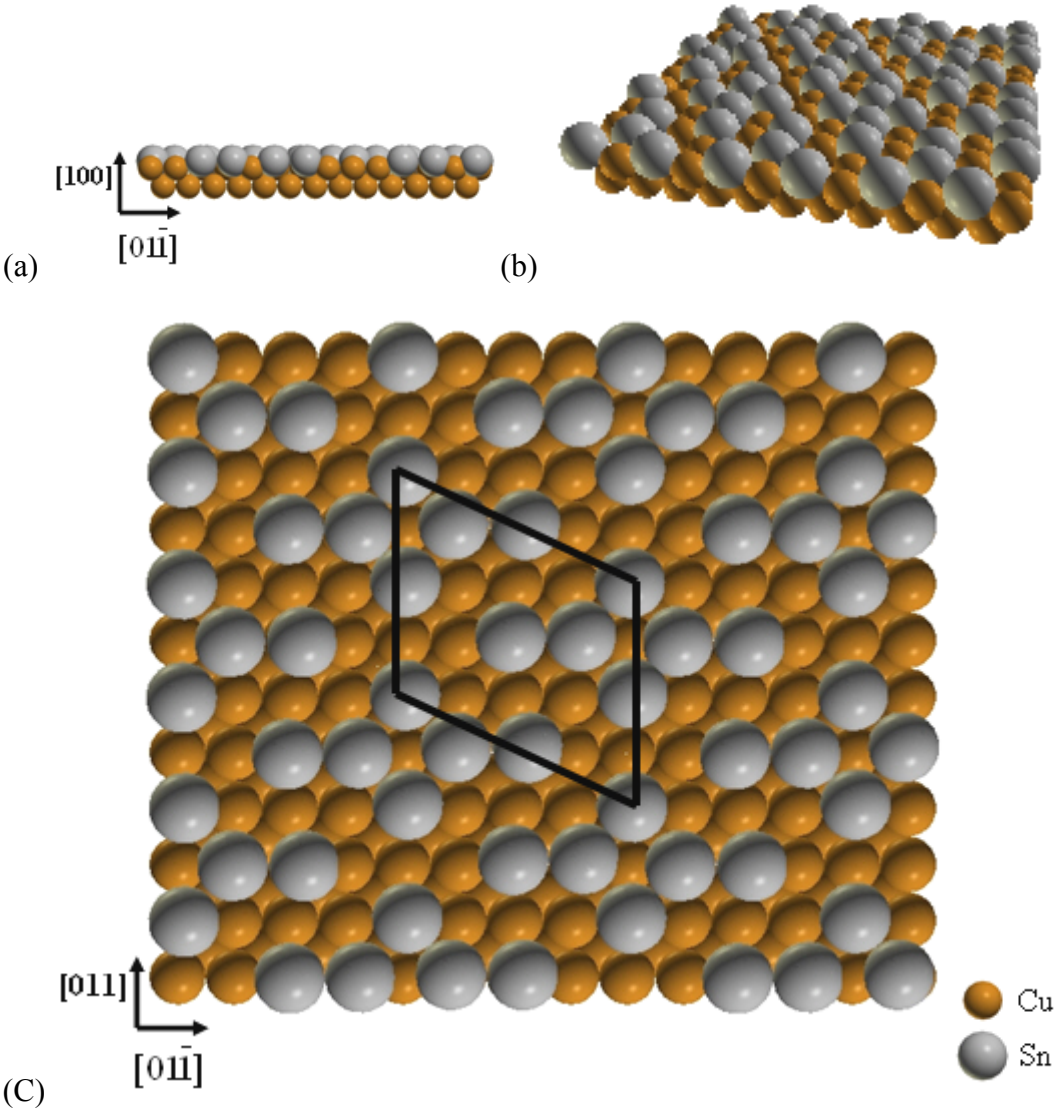

Figure 3.38: Proposed model for the new Sn/Cu(100) Phase IIH surface alloy. (a) Front view (011) plane, (b) perspective view and (c) top view (100) plane. Unit cell shown in black.

3.7 Sn/Cu(100) Phase III

3.7.1 Literature Review

Phase III is described in all publications as a rotated p($3\sqrt{2}$ x $\sqrt{2}$)R45° double domain structure with intense (1/2, 1/2) beams. Argile and Rhead [6] proposed a model that provided the correct symmetry and periodicity but did not produce the higher

intensity of the (1/2, 1/2) beams. McLoughlin *et al.* [7] proposed a structure for Phase III that is produced by the addition of Sn atoms to their phase II structure. The additional Sn atoms fill the vacancy in the centre of the p(2 × 2) cell to form a complete c(2 x 2) surface. This however leads to significant strain along the [010] direction due to the larger metallic radius of the Sn atoms compared to the copper atoms (Sn/Cu ~ 1.27). This strain can be relieved by a buckling and/or small lateral displacement of the Sn and Cu atoms. If every second and third Sn rows of the ideal c(2 × 2) structure are compressed as shown in Figure 3.39, then higher intensity (1/2, 1/2) beams are observed in the simulated LEED pattern. This theory was tested by K. Pussi *et al.* [47] using dynamical LEED calculations prepared using the Barbieri/Von Hove Symmetrized Automated Tensor LEED package [48]. Pendry reliability factors were used to evaluate the agreement between the model and the experimental data. It was concluded that the strain in the topmost layers was released by both lateral relaxation and buckling within the Cu layers. The favoured structure was a surface alloy model that included a missing Cu row and a buckled Sn-Sn atoms spacing of 0.31 ± 0.01 nm as shown in Figure 3.39.

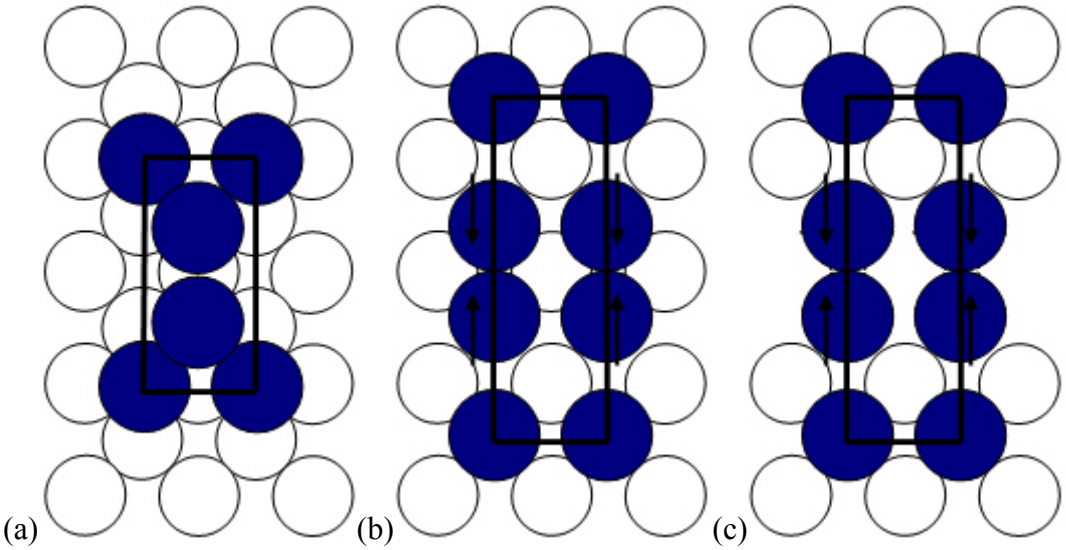

Figure 3.39: Sn/Cu(100) Phase III (a) overlayer model Argile and Rhead, (b) surface alloy model McLoughlin and (c) missing row model Pussi.

3.7.2 LEED Results

Upon further depositions of Sn onto the Phase II surface the rotated domain p(3√2 × √2)R45° with intense (1/2, 1/2) beams forms, as shown in Figure 3.40. A higher intensity in the (1/3, 1/3) and equivalent beams is also noted, these results are in excellent agreement with all previous publications [5] [6] [42] showing this surface

structure. The LEEDpat simulation is included in Figure 3.40 as a confirmation of the p(3√2 × √2)R45° structure.

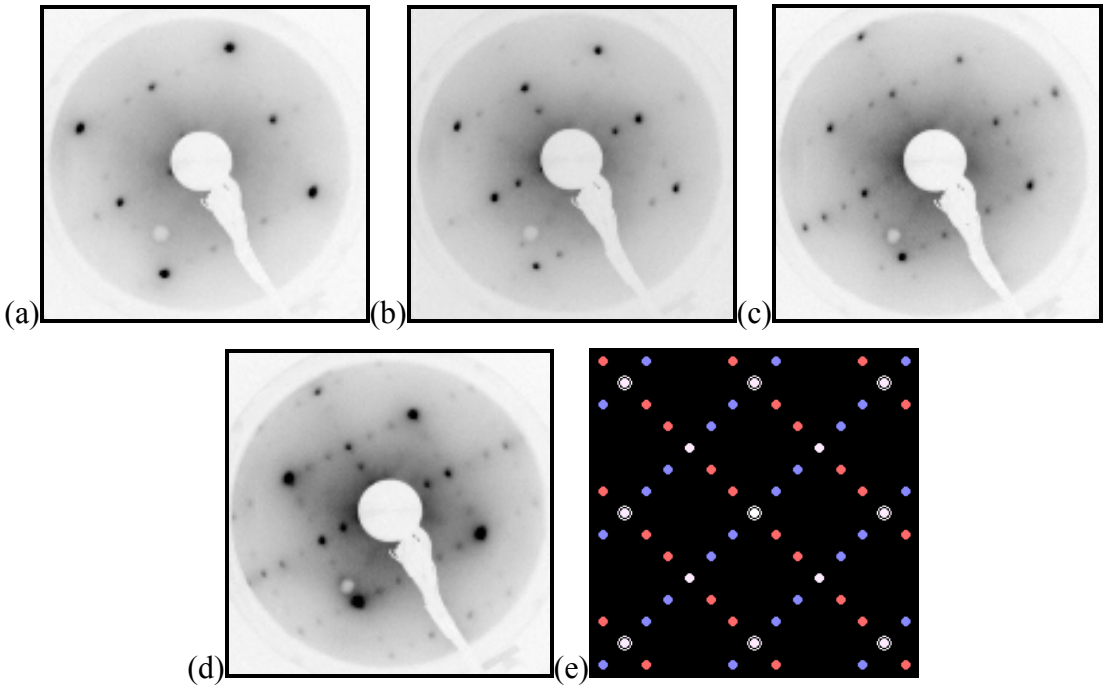

Figure 3.40: LEED diffraction patterns of the Sn/Cu(100) Phase III recorded at (a) 76eV, (b) 88eV, (c) 110eV and (d) 124eV. The higher intensity of the (1/2, 1/2) beams is noted. Also shown is a model of the image produced using the LEEDpat simulation (e).

Figure 3.41 shows the I(V) spectra for the integral order and the fractional order beams obtained from this surface. A total of three integral order and six fractional order beam intensities were recorded at normal incidence.

.

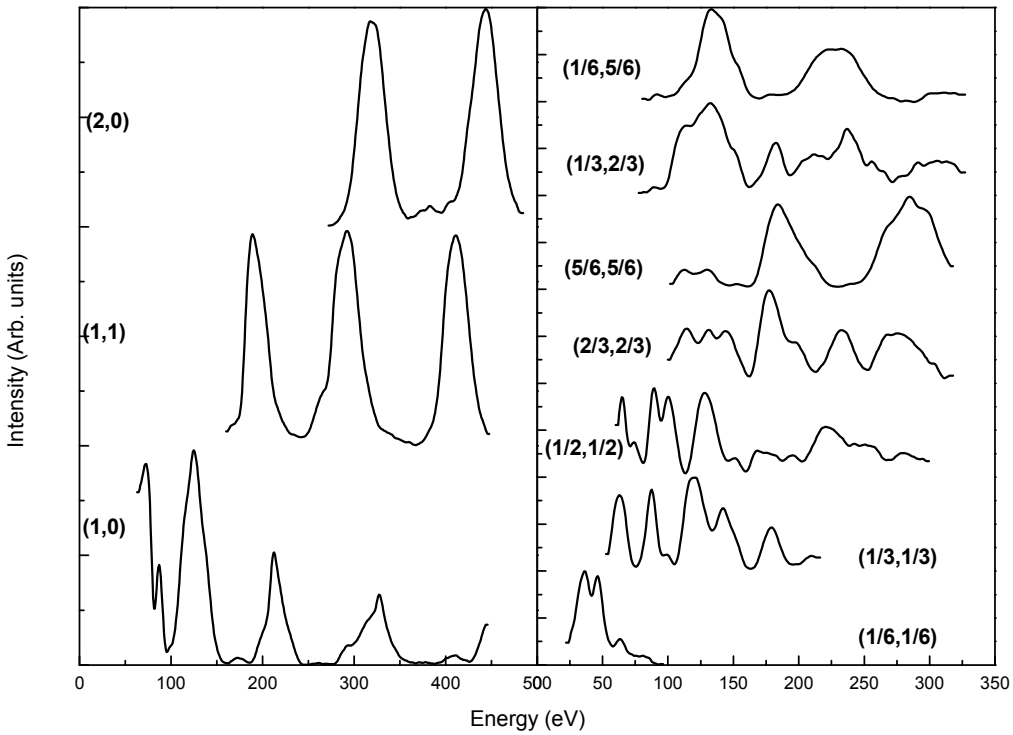

***Figure 3.41*:** Integral and fractional order I(V) beam spectra for Sn/Cu(100) Phase III LEED diffraction pattern, recorded at normal incidence.

3.7.3 STM Results

A Sn deposition of θ_{Sn} = 0.5 ML at room temperature on the Cu (100) surface results in a distorted c(2 × 2) structure. This distortion is due to the significant strain induced by accommodating the larger metallic radius of Sn (1.64 Å) within a layer of Cu atoms (atomic radius = 1.275 Å). The presence of many islands on the surface is noted in this phase, Figure 3.42. It is proposed that these islands form due to the row of Cu displaced by the Sn atoms as proposed in the model of Pussi *et al.* [47]. The islands are then formed by surface diffusion of the displaced Cu atoms. The displaced Cu atoms may also attach to the step edges. It is noted in all STM images that the step edges are always the last areas on the surface to complete the transition to the next phase when additional Sn is added to the surface. Every island is a single domain of phase III. These well ordered rectangular shaped islands are aligned parallel to the [001] or [010] directions. Using the flooding process in the WSxM program [27] the area of the surface covered by islands is measured to be ~ 30%. This is in excellent agreement with model proposed by Pussi *et al.* [47].

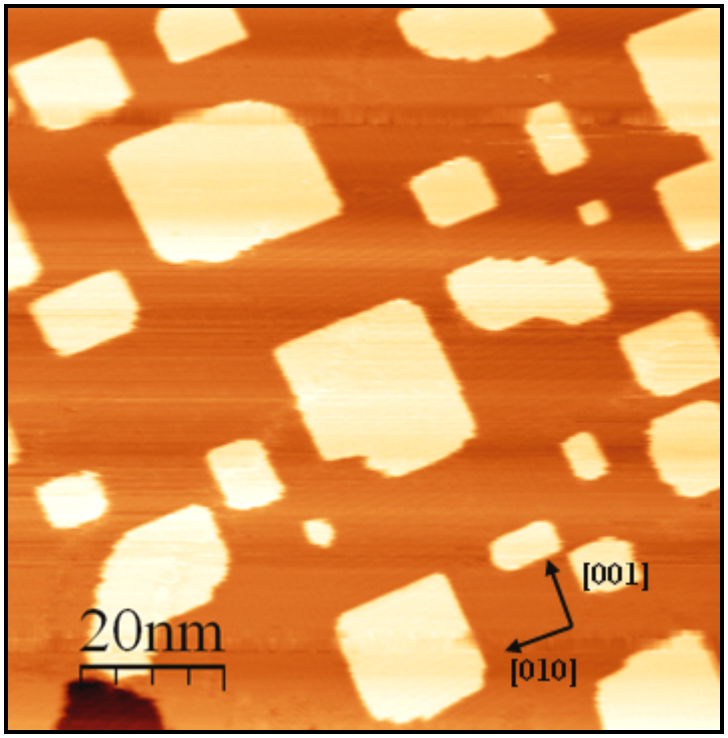

***Figure 3.42*:** STM images of the Sn/Cu(100) Phase III surface structure showing multiple island formations, , taken at V_s = -0.01V, I_t = 3.0nA, 100nm^2.

The surface consists of two domains of p(3√2 × √2)R45° structure, rotated by 90° relative to each other and orientated along the [001] and [010] directions, as seen in Figure 3.43. Vertical and horizontal corrugations of the surface are observed and can be accounted for by the surface strain in the [010] direction. Figure 3.44(c) shows a "Y-average" line profile of a single domain of the Phase III structure. The "Y-average" line profile is a function of the WSxM program [27] which averages all horizontal lines of the image and displays a single curve. The surface modulation is clearly visible It is observed that every third tin row is higher and the two tin rows in between are compressed laterally. Measurements from this and similar profiles determine a distance of 0.344 ± 0.02 nm between the atoms of the compressed rows. This result is in excellent agreement with the separation of 0.32 nm proposed in the model based on the previous LEED studies [7] and the 0.31 ± 0.01 nm spacing determined from I(V) LEED calculations [47]. The vertical corrugation of 0.009 ± 0.002 nm measured from the STM images compared favourable with 0.012 ± 0.007 nm from the same I(V) LEED study [47].

(a) 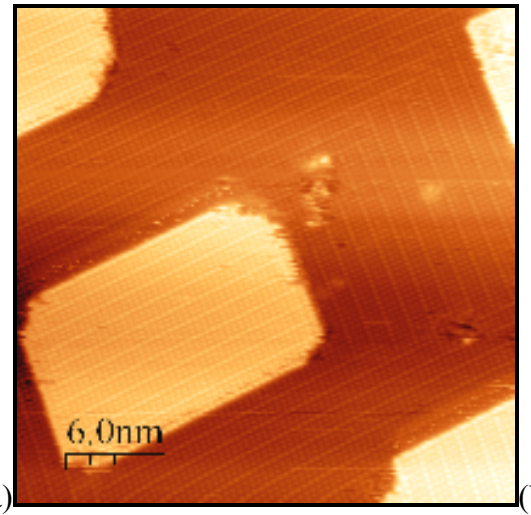

(b) 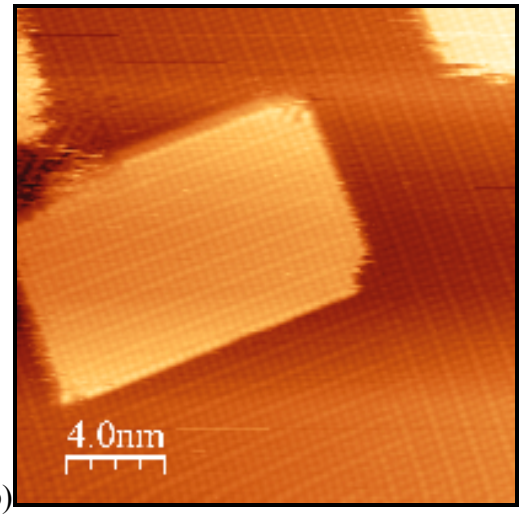

Figure 3.43: STM images of the Sn/Cu(100) Phase III surface, showing well ordered island formation. The top surface of each island is a single domain of Phase III. Also shown are double domains rotated by 90° to one another, orientated in the [001] and [010] directions. (a) V_s = -0.10V, I_t = 31.0nA, 30nm^2 and (b) V_s = -0.01V, I_t = 3.0nA, 50nm^2.

A Fourier transform of the single domain of Phase III is shown in Figure 3.44(b). The Fourier transform exhibits a distorted unit cell as a consequence of the drift in the STM image. The reciprocal lengths of 0.804 ± 0.005 nm^{-1} and 2.483 ± 0.005 nm^{-1} are recorded along the [010] and [001] directions respectively. These reciprocal lengths correspond to substrate lattice spacings of 4.877 and 1.579 which are in good agreement with the expected p(3√2 × √2)R45° lattice spacing lattice spacing of the unit cell when drift of the local structure is taken into consideration (3√2 = 4.243 and √2 = 1.414).

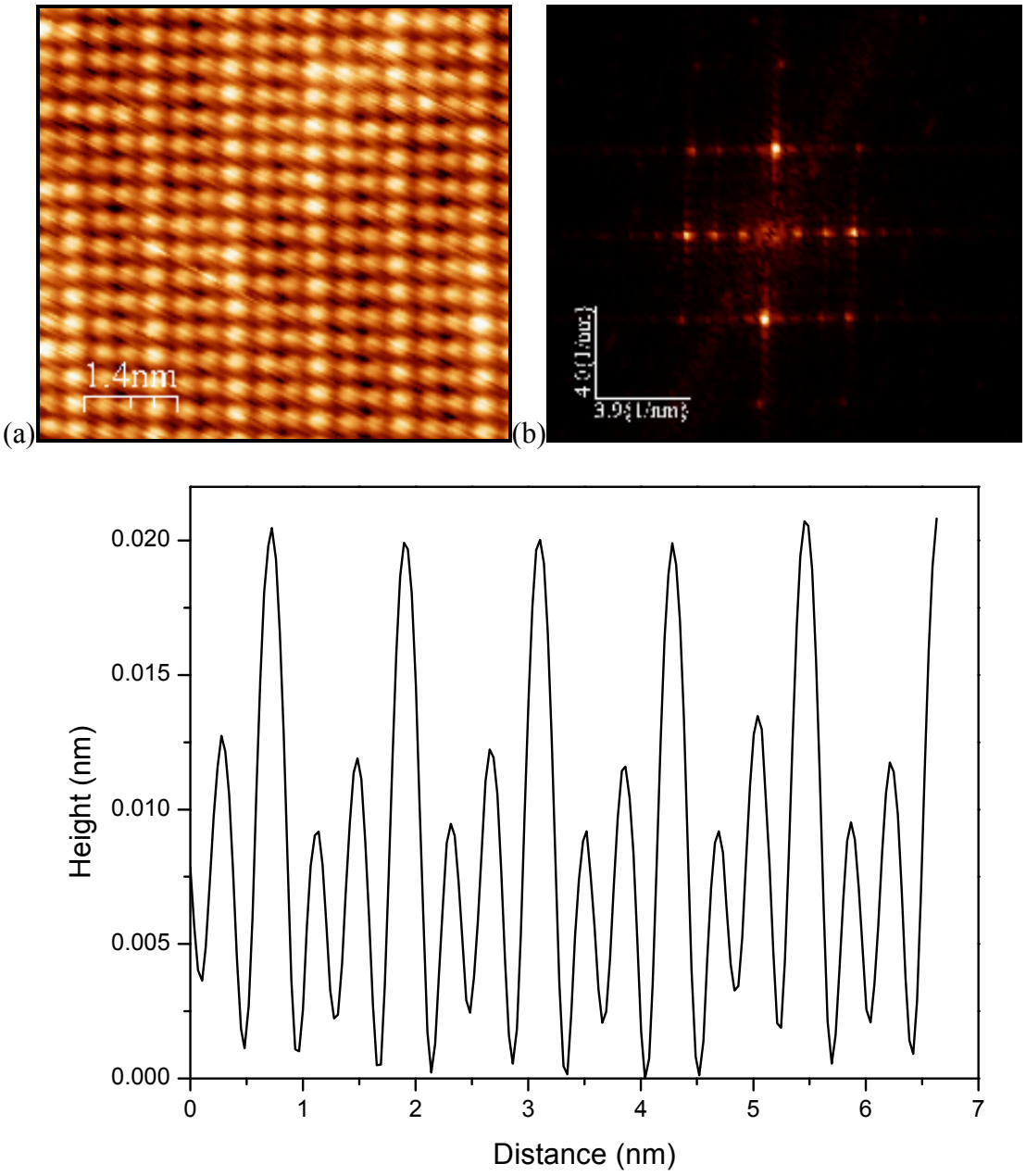

(a) (b) (c)

Figure 3.44: Magnified STM image of the Sn/Cu(100) Phase III surface, V_s = -0.685V, I_t = 2.739nA, 9nm^2 ,the corresponding (b)Fourier transform and (c) "Y-average" profile.

3.7.4 Conclusion

The recorded STM and LEED results gave excellent agreement with the surface alloy model proposed for Phase III by McLoughlin *et al*. [7] and further developed through I(V) LEED calculations by Pussi *et al.* [47]. The distance of 0.344 ± 0.02 nm between the centres of the compressed rows of Sn atoms as measured from the STM

images compares well to the value of 0.32 nm proposed in the model based on the previous LEED studies [7] and the 0.31 ± 0.01 nm based on the I(V) LEED study of Phase III [47]. The vertical corrugation of the Sn rows Δ_{Sn} = 0.009 ± 0.002 nm taken from STM measurements also compares favourably to the Δ_{Sn} = 0:012 ± 0:007 nm obtained from the I(V) LEED study [47].

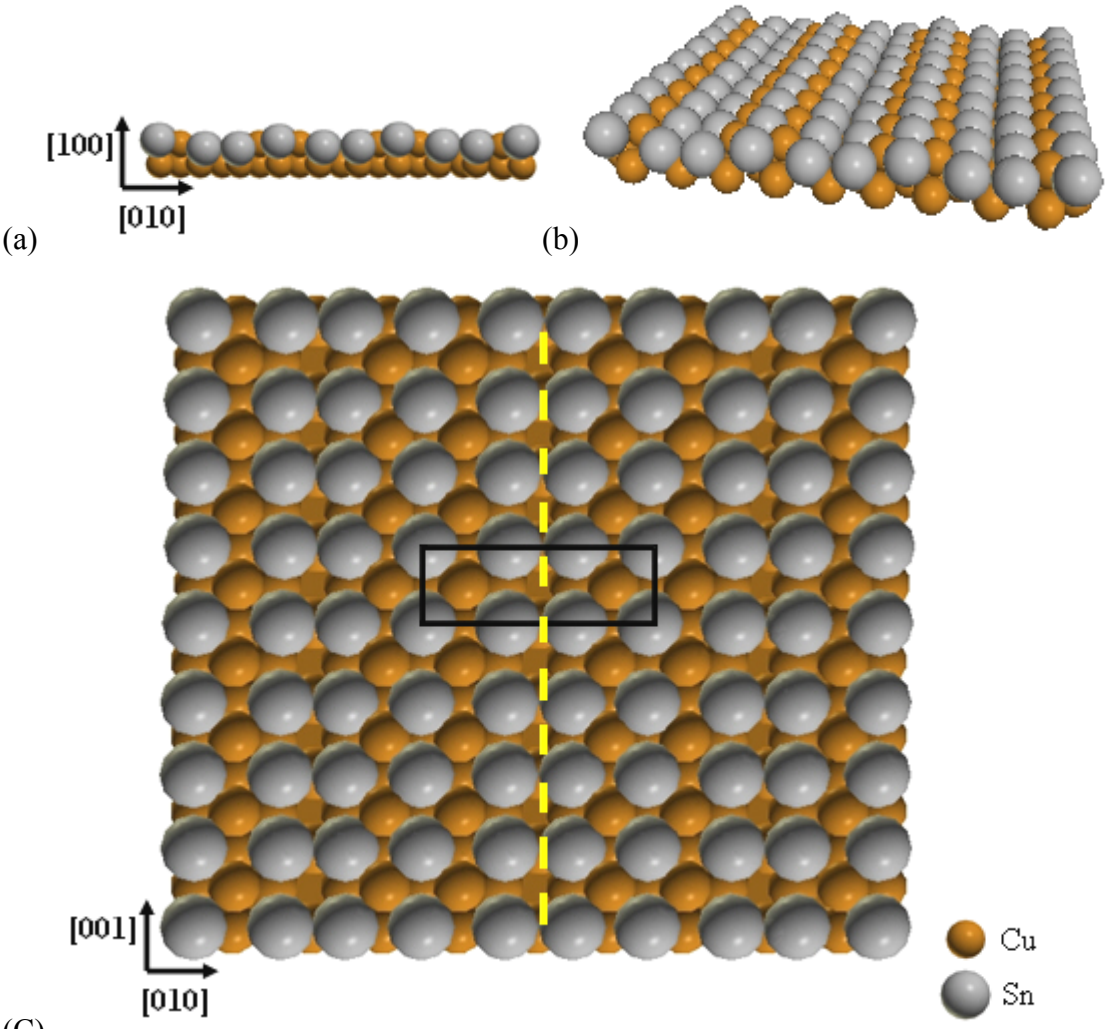

Figure 3.45: Proposed model for the new Sn/Cu(100) Phase III surface alloy. (a) Front view (011) plane, (b) perspective view and (c) top view (100) plane. The unit cell is shown in black and the missing row of Cu atoms is shown with the dashed yellow line.

The presence of islands in this phase and the lateral and vertical compression of the Sn rows give weight to the missing row model for Phase III. The Cu atoms displaced from between the lower rows of Sn atoms diffuse across the surface to provide the additional Cu to form these islands [43] and add to the step edges. Figure

3.45 shows the model proposed for the Sn/Cu(100) Phase III surface. Figure 3.46 shows the missing row surface alloy model developed by Pussi et al.[47].

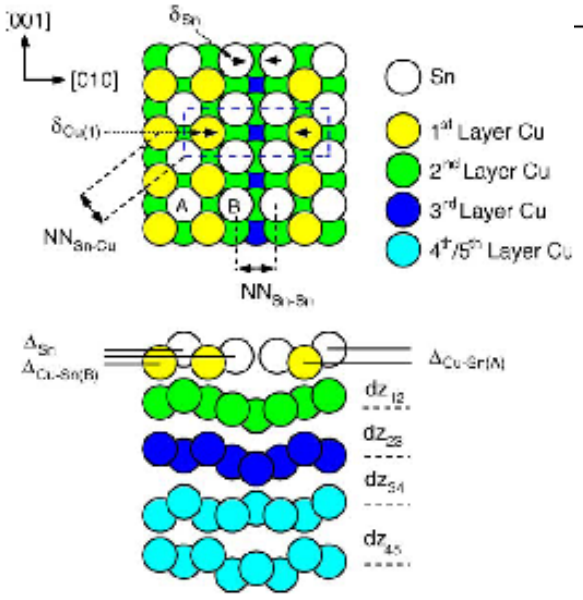

Parameter	Value [Å]
Δ_{Sn}	0.12 ± 0.08
$NN_{Sn\ Sn}$	3.10 ± 0.10
$NN_{Sn\ Cu}$	2.59 ± 0.07
$\Delta_{Cu-Sn(A)}$	0.39 ± 0.07
$\Delta_{Cu-Sn(B)}$	0.27 ± 0.07
δ_{Sn}	0.26 ± 0.10
$\delta_{Cu(1)}$	0.01 ± 0.04
$\delta_{Cu(2)}^{average}$	0.04 ± 0.04
dz_{12}	1.87 ± 0.04
dz_{23}	1.82 ± 0.04
dz_{34}	1.80 ± 0.07
dz_{45}	1.80 ± 0.10
dz_{56}	1.79 ± 0.11
$\Delta_{Cu(2)}^{average}$	0.06 ± 0.04
$\Delta_{Cu(3)}^{average}$	0.04 ± 0.05
$\Delta_{Cu(4)}^{average}$	0.02 ± 0.09
$\Delta_{Cu(5)}^{average}$	0.02 ± 0.11

Figure 3.46: Sn/Cu(100) Phase III missing row surface alloy model developed by Pussi *et al*. [47] included with permission.

3.8 Sn/Cu(100) Phase IV

3.8.1 Literature Review

Phase IV has a p(2√2 × 2√2)R45° structure and forms a complete monolayer. Structural models suggested by Argile and Rhead [6] and McLoughlin [7] are illustrated in Figure 3.47. It is observed from the diffraction pattern that the (1/4, 1/4) beam is more intense than the (1/2, 1/2) beam. This is not reflected in any of the simulations of the three models. The model suggested by Argile and Rhead gives the best agreement between the observed diffraction pattern and the simulated pattern, but the difference between the intensity ratios would indicate that Phase IV is not correctly modelled and further strain relief must be considered.

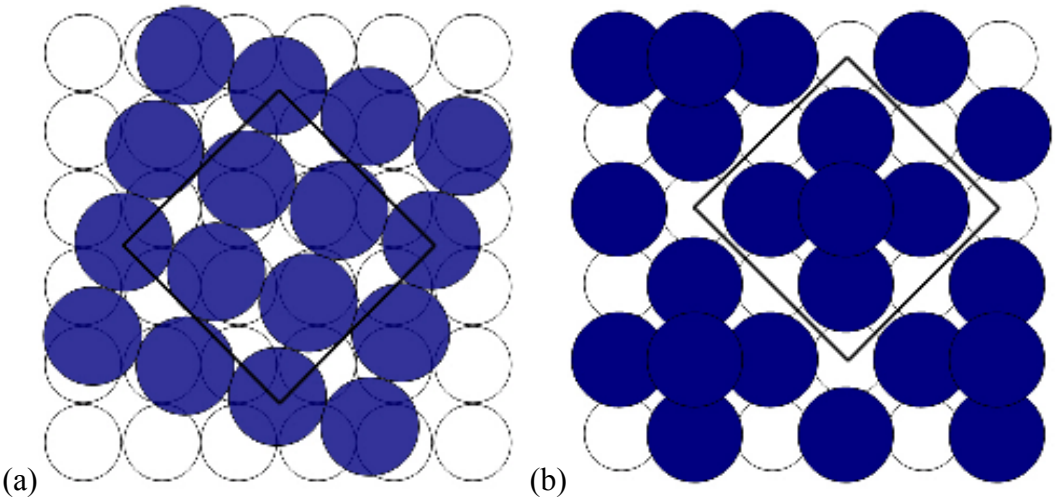

Figure 3.47: Surface structure models of Sn/Cu(100) Phase IV (a) Argile and Rhead overlayer model and (b) McLoughlin surface alloy model. Unit cells shown in black.

Lallo *et al.* [9] proposed a model for the Sn/Cu(100) Phase IV surface structure from STM investigations. This model consists of 5 Sn atoms for every 8 Cu atoms per unit cell, with four atoms forming an overlayer on the Cu(100) surface and one atom in a substitutional site in the top layer of Cu atoms, as shown in Figure 3.48.

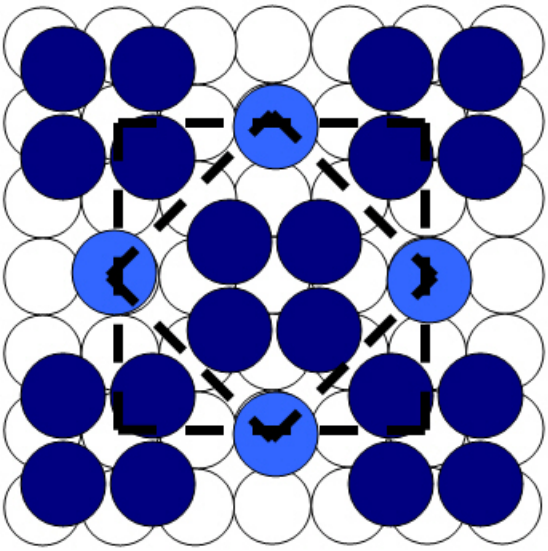

Figure 3.48: Sn/Cu(100) Phase IV model proposed by Lallo *et al.* Unit cell shown in black. Dark blue circles represent Sn atoms situated on the Cu(100) surface while light blue circles represent Sn atoms not present in STM images, situated in a lower layer.

3.8.2 LEED Results

After further deposition of Sn the p($2\sqrt{2} \times 2\sqrt{2}$)R45° diffraction pattern of Phase IV is formed, Figure 3.49, for Sn coverage ~ 0.625 ML. The LEEDpat simulation, Figure 3.50, is included as a guide. Increasing the Sn coverage on this surface results in an increase in the background intensity and loss of the diffraction pattern.

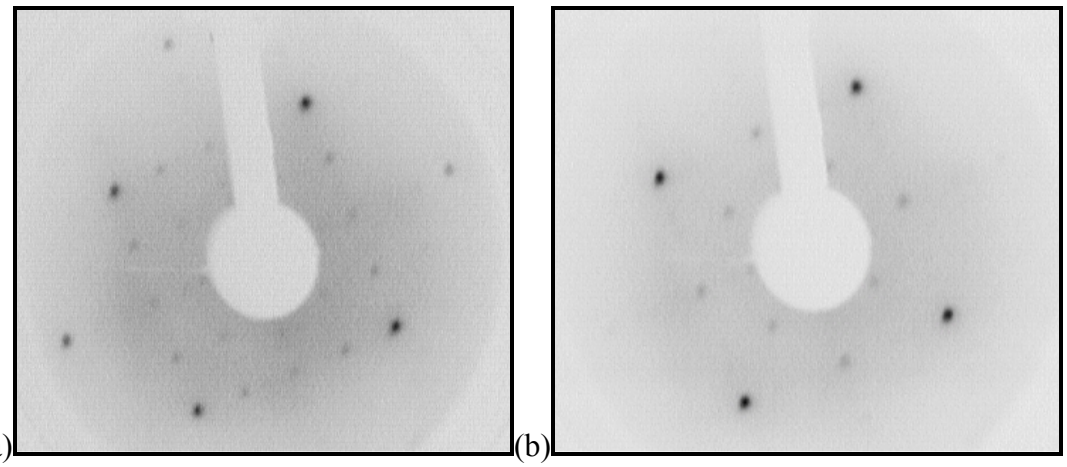

***Figure 3.49*:** LEED diffraction patterns for the Sn/Cu(100) Phase IV recorded at (a)116eV and (b)128 eV respectively.

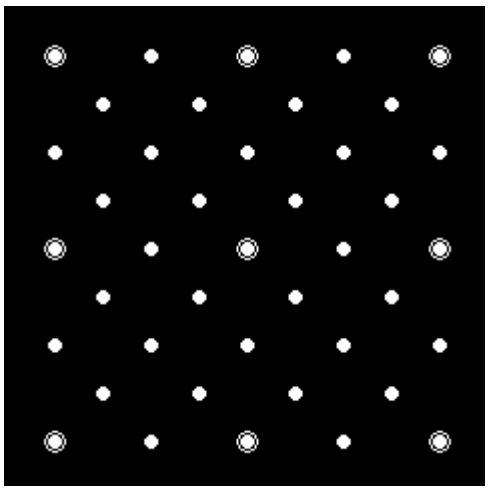

***Figure 3.50*:** LEEDpat simulation for the Sn/Cu(100) Phase IV diffraction pattern.

The measured I(V) spectra for three integral order and seven fractional order beams are shown in Figure 3.51.

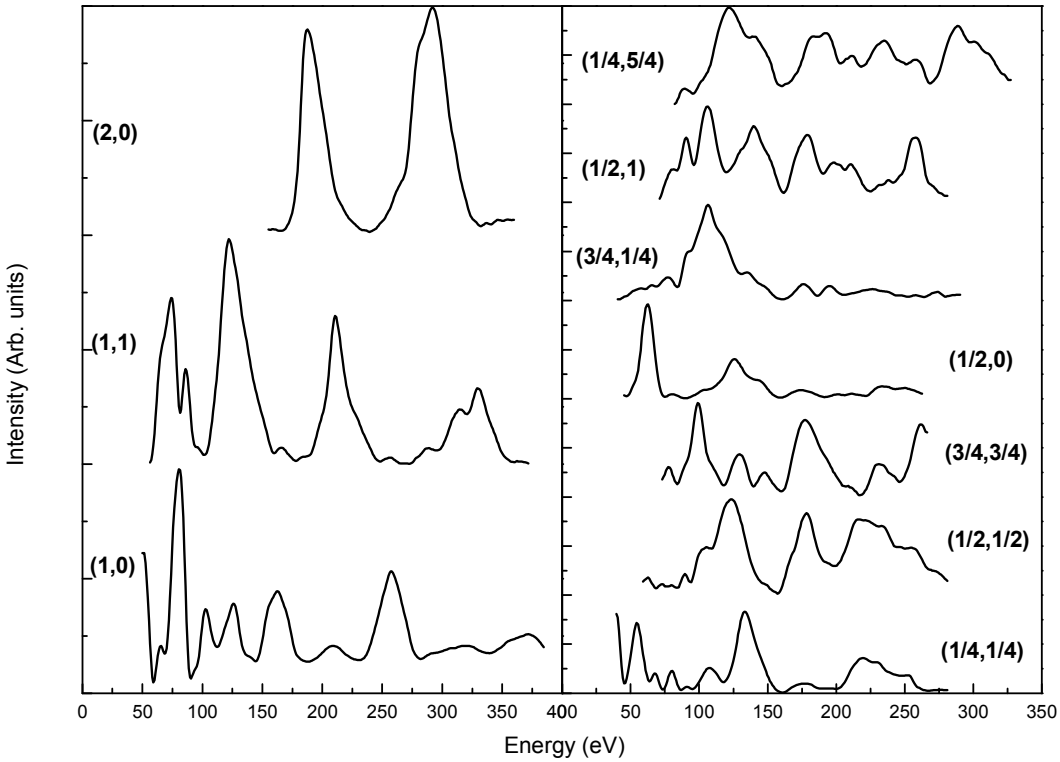

Figure 3.51: Integral and fractional order I(V) beam spectra for Sn/Cu(100) Phase IV LEED diffraction pattern, recorded at normal incidence.

3.8.3 STM Results

The Sn/Cu(100) Phase IV surface structure was the hardest of the phases to image using STM. The deposition of additional Sn onto this surface leads to the loss of any LEED diffraction pattern due to the lack of periodicity and order of the surface Sn. The additional Sn atoms are observed to be loosely bound and can easily be picked up by the STM tip as it scans across the surface. This causes a streaking of the STM image and a loss of resolution. This is shown in Figure 3.52, where large domains of Phase IV are present separated by areas containing loose Sn randomly sitting on the surface. This confirms the Stranski Krastanov growth mode predicted by the Auger signal versus time plots of Argile and Rhead [6] [42] in the higher Sn coverage areas.

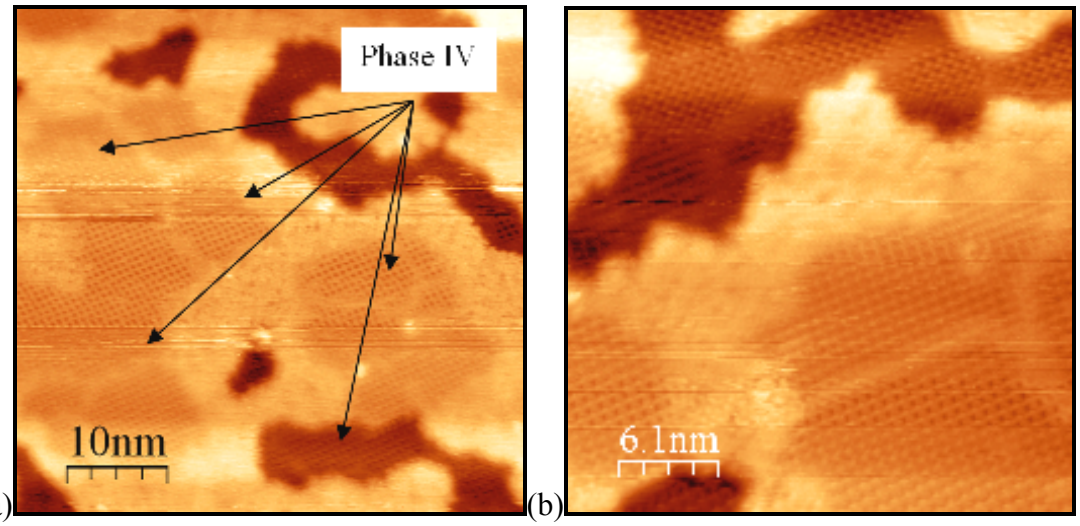

(a) (b)

***Figure 3.52*:** STM image of Sn/Cu(100) Phase IV surface structure (a) V_s = -0.50V, I_t = 1.0nA, 50nm^2, (b) V_s = -0.10V, I_t = 0.5nA, 30nm^2. Streaking in the image is attributed to the interaction of loosely bound Sn atoms with the STM tip.

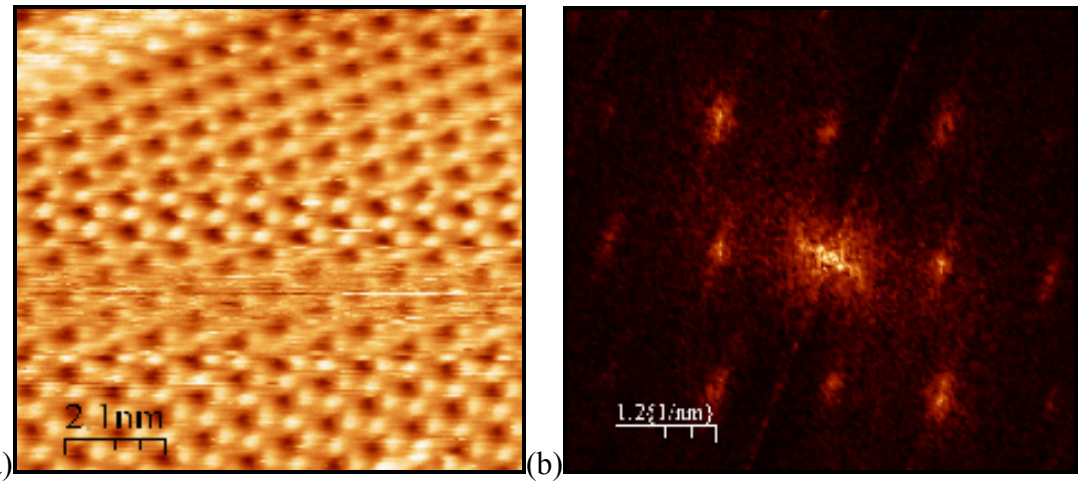

(a) (b)

Figure 3.53: STM image of Sn/Cu(100) Phase IV surface structure, V_s = -0.10V, I_t = 0.5nA, 10nm^2 and its corresponding Fourier transform.

Dark holes are observed in the reconstructed regions of the surface between crossing rows consisting of bright spots which are attributed to the Sn atom positions. A Fourier transform of the single domain of Phase IV is shown in Figure 3.53. The Fourier transform exhibits a distorted unit cell as a consequence of the drift in the STM image and the streaking due to loose Sn atoms interacting with the STM tip. The reciprocal lengths of 1.255 ± 0.005 nm^{-1} and 1.361 ± 0.005 nm^{-1} are measured. These reciprocal lengths correspond to substrate lattice spacings of 3.125 ± 0.002 and 2.882 ± 0.002.

These measurements are in good agreement with the expected p($2\sqrt{2} \times 2\sqrt{2}$)R45° lattice spacing of the unit cell ($2\sqrt{2} = 2.828$).

3.8.4 Conclusions

Fourier transforms of the STM images are in excellent agreement with a p($2\sqrt{2} \times 2\sqrt{2}$)R45° structure deduced from the LEED diffraction patterns. It is generally accepted for metals that the maxima observed in the STM images correspond effectively to the atomic positions [41]. Accepting this assumption it is possible to evaluate the three different models [6] [7] [9] proposed for this structure by comparing the position of the maximum intensity in the STM images with the Sn atom positions in the models. Best agreement was reached with the surface alloy model of McLoughlin [5], because the maximum intensity coincides with the Sn atom positions in the model and it can also account for the square dark holes noted in the STM images. This new model has an optimum Sn coverage for Phase IV of $\theta_{Sn} \sim 0.625$ ML, with 5 Sn atoms per 8 Cu atoms in the unit cell. Four of the Sn atoms occupy the first layer and are positioned at the four-fold hollow site in each unit cell. A single Sn atom occupies a second layer and is positioned between neighbouring Sn atoms of the first layer. The model for the Sn/Cu(100) Phase IV surface is shown in Figure 3.54.

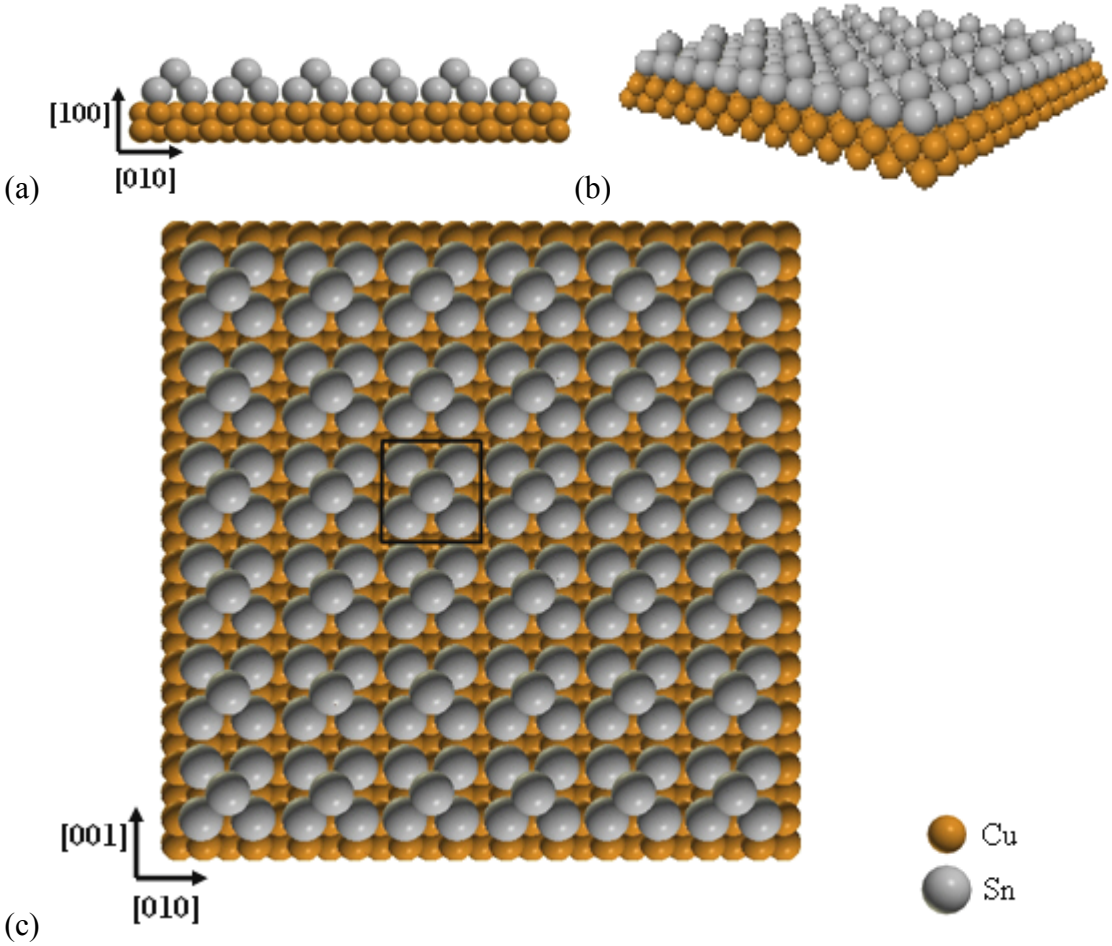

Figure 3.54: Proposed model for the new Sn/Cu(100) Phase IV surface structure. (a) Front view (011) plane, (b) perspective view and (c) top view (100) plane. The unit cell is shown in black.

Chapter 4: Photoemission Spectroscopy

4.1 Introduction

This chapter presents the results of a synchrotron based photoemission spectroscopy (PES) study of the five submonolayer surface phases of the Sn/Cu(100) surface alloy. The results reported in this chapter are the first reported PES study of this surface alloy system. Four submonolayer phases of the Sn/Cu(100) system were originally reported by Argile and Rhead [6]: Phase I with Sn coverage ~ 0.18ML, Phase II with Sn coverage ~ 0.33ML, Phase III with Sn coverage ~ 0.5ML and Phase IV with Sn coverage ~ 0.625ML. These results were revised by McLoughlin [5] using Auger electron spectroscopy (AES), monitoring the LEED spot profiles as a function of evaporation time and double scattering LEED pattern simulations. This analysis indicated that Phases I-IV reached maximal perfection at Sn coverages of ~ 0.21, 0.37, 0.5 and 0.70 ML respectively. A new phase appearing between Phase II and Phase III was recently reported by Martinez-Blanco *et al.* [8] based on LEED measurements. This new phase is observed over a very narrow Sn coverage range of ~ 0.6 ML of a monolayer centred at ~0.40 ± 0.02 ML [9]. This new phase has been designated as Phase IIH or higher Phase II.

The Cu 3p and Sn 4d core levels for all the surface phases are investigated using high resolution core-level spectroscopy (HRCLS). A comparative study of the valence bands photoemission spectra for each phase over a range of photon energies was also carried out.

4.2 Experimental Details

The experimental details of these photoemission experiments are detailed in chapter 2.4.

The width of the Gaussian lineshape can be approximated from the instrumental broadening, which is a combination of the photon energy broadening and the broadening in the Scienta electron energy analyser. From Figure 2.15 the resolution of the SGM 1 beamline at the photon energies required are used. The SCIENTA analyzer has a resolution of approximately 200 meV. The equation for calculating the total Gaussian width is

$$E = \sqrt{\Delta E^2_{SCIENTA} + \Delta E^2_{SGM1}} \qquad 4.1$$

therefore the approximate Gaussian width needed to fit the Sn 4d peaks is

$$E = \sqrt{(200\text{meV})^2 + (130\text{meV})^2} \quad 4.2$$

$$E = 0.24 \text{ eV} \quad 4.3$$

This is an approximate value since there are other factors which can influence the broadening, but these values may be used as good start values to begin the fitting process.

4.3 Photoemission Results

4.3.1 Cu 3p HRCLS Analysis

The Cu 3p core level peaks were measured for the five submonolayer surface alloy phases of the Sn/Cu(100) system. Additionally, these peaks were measured after the further deposition of two Sn layers of increasing thickness, designated T1 and T2 in the following spectra. These thick layers do not form an ordered structure, this is evidenced by the complete loss of the p(2√2 × 2√2)R45° LEED pattern of Phase IV. Figure 4.1 shows scans of the Cu 3p peaks at each stage of the experiment normalised to the photon intensity and the number of scans. Each Cu 3p peak is fitted with two component peaks due to the different bonding environments of the outermost layer of Cu atoms compared to the bulk Cu atoms [49].

Figure 4.2 shows the reduction in the substrate signal with increasing phase coverage of Sn. The increase in intensity of the Cu 3p peaks for Phase III coverage compared to the lower Sn coverage of Phase IIH is unexpected. The STM study of phase III in section 3.7.3 showed the formation of ordered islands on the Sn/Cu(100) Phase III surface. These islands were measured to cover ~ 30% of the surface. This is evidence of the missing row model developed by Pussi *et al.* [47], where every third row of copper atoms is displaced. These displaced atoms diffuse across the surface of the crystal to form the islands. The STM images show these islands to be completely covered with Sn, forming a single Phase III domain on each island. Thus this reconstructing of the crystal surface should not produce an increase in the intensity of the Cu 3p peaks. No evidence of areas of uncovered copper was found, that could account for the increase in intensity of the Cu 3p peaks. This photoemission result suggests the formation of a surface alloy in Phase III, with the formation of overlayer structures in the other phases of both high and lower Sn coverage. This transition from an overlayer to an alloy and back to an overlayer model for the Sn/Cu(100) surface

system seems unlikely and is not consistent with the findings of HAS, I(V) LEED, LEED image, NIXSW and STM studies in either this thesis or in the literature [5] [7] [9] [40] [45].

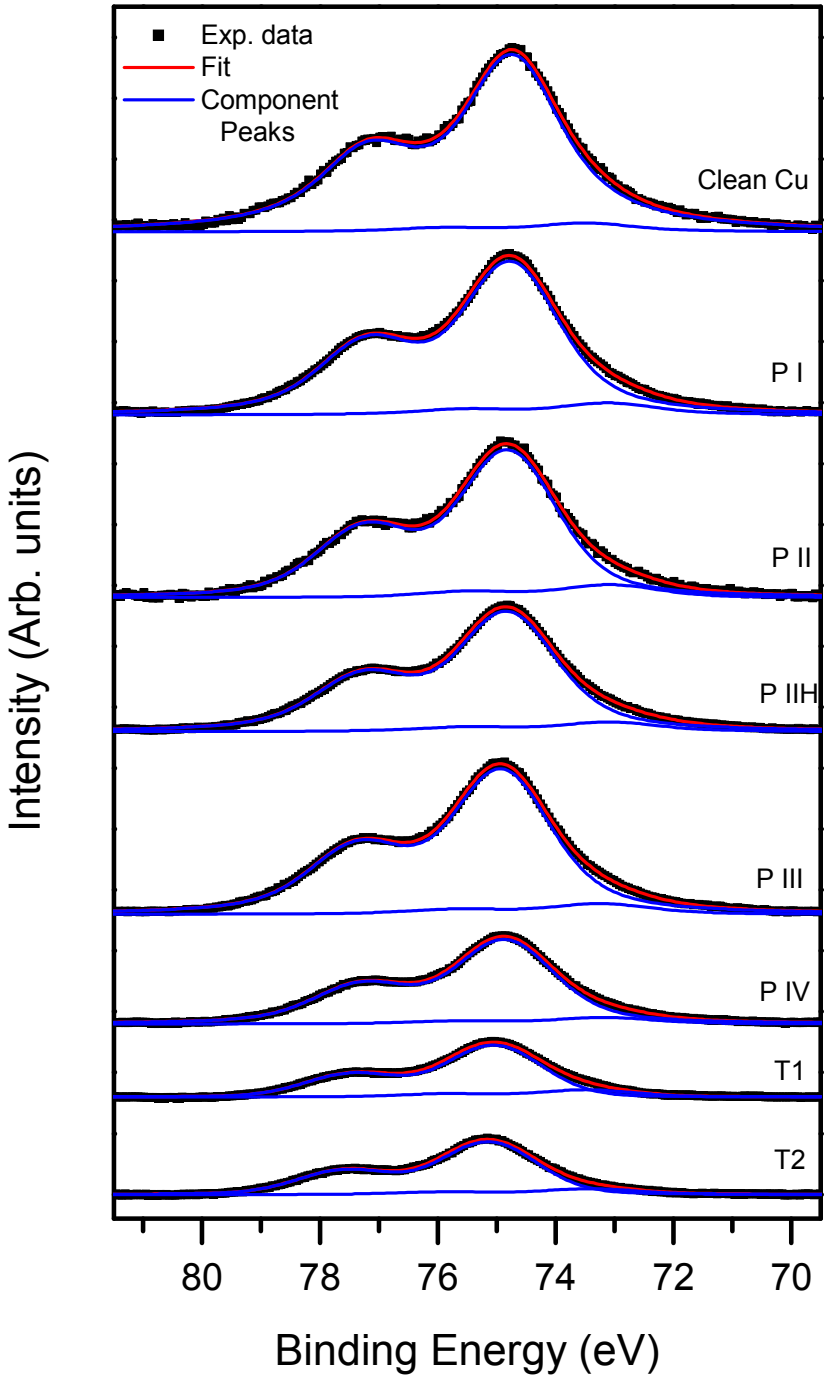

Figure 4.1: Normalised Cu 3p core level peaks (hν = 150 eV) with increasing Sn coverage from top to bottom. A Shirley type background has been removed from all spectra.

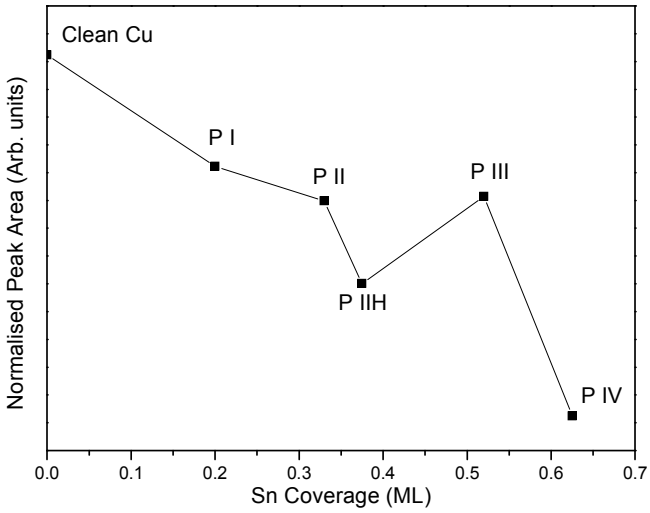

Figure 4.2: Normalised peak area of the Cu 3p substrate peak (hν = 150 eV) plotted for increasing Sn coverage.

Coverage	Peak	Peak area	Peak position	Line width	Spin-Orbit Splitting	Branching ratio
Clean Cu	1	552.58	74.718	1.836	2.457	0.4165
	2	28.451	73.476			
Phase I	1	446.06	74.751	1.6848	2.432	0.4509
	2	34.628	73.091			
Phase II	1	413.74	74.795	1.680	2.436	0.4546
	2	35.871	73.061			
Phase IIH	1	347.93	74.811	1.699	2.441	0.4449
	2	27.31	73.065			
Phase III	1	422.51	74.906	1.706	2.441	0.4424
	2	31.018	73.221			
Phase IV	1	238.28	74.849	1.697	2.427	0.4449
	2	17.899	73.149			
Thick 1	1	127.84	75.033	1.778	2.399	0.4472
	2	17.507	73.462			
Thick 2	1	133.08	75.126	1.776	2.43	0.4577
	2	14.025	73.398			

Table 4-1: Fitting data acquired for the Cu 3p peaks at hν = 150 eV using AAnalyzer [32]

This anomalous result may be caused by an error in the slit setting or alignment of the sample and merits further investigation in the future. Sn 4d peak and valence band scans taken for the Phase III surface show no unusual results which would aid an explanation.

The surface component of the Cu 3p peak has a lower binding energy than the bulk component. With increasing Sn coverage the binding energy of the surface component of the Cu3p peak decreases, showing that there is a charge transfer from the Sn atoms to the outermost layer of Cu atoms.

The binding energy of the bulk Cu 3p peak of 74.8 ± 0.2 eV and the spin-orbit splitting of 2.4 ± 0.2 eV are similar to the values quoted in the literature for Cu, E_B = 75.1 eV and 2.2 eV [50]. Table 4-1 shows the fitting data acquired for the Cu 3p peaks (hν = 150 eV) using AAnalyzer [32].

4.3.2 Sn 4d HRCLS Analysis

The Sn 4d core level peaks were measured for the five submonolayer surface alloy phases of the Sn/Cu(100) system. Additionally these peaks were measured after the further deposition of two thick layers Sn (T1and T2) on the crystal surface. Figure 4.3 shows the increasing (a) Sn 4d signal with increasing phase coverage of Sn compared to the decreasing Cu 3p substrate peak (b).

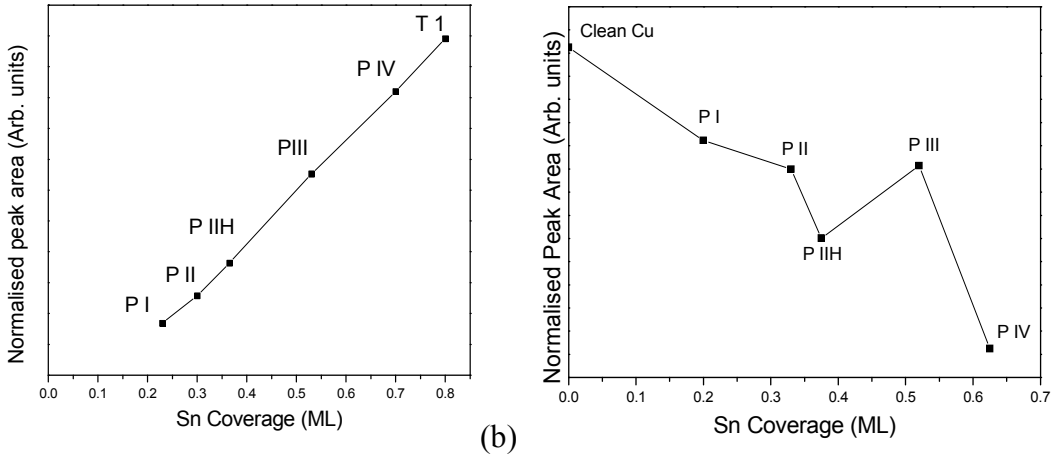

(a) (b)

Figure 4.3: (a) Sn 4d peak area (hν = 85 eV) as function of increasing Sn coverage and (b) Cu 3p substrate peak area (hν = 150 eV) as a function of increasing Sn coverage.

The Sn 4d peak shows the expected steady increase in the intensity and does not exhibit any deviation correlated with that observed in the intensity of the Cu 3p peak for Phase III.

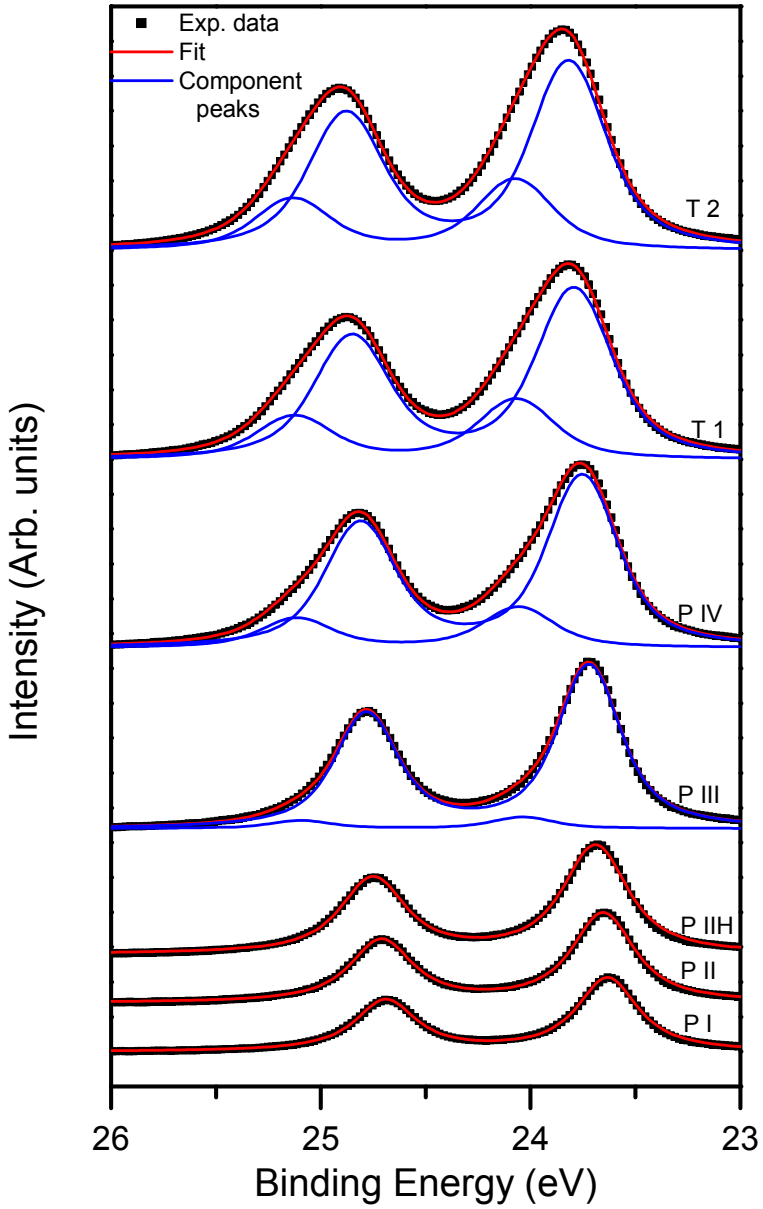

***Figure 4.4**:* Sn 4d peaks for increasing Sn coverage of Cu (100) taken at hν = 85 eV. A Shirley type background has been removed from all spectra.

Due to the greater atomic radii of Sn atoms compared to Cu atoms (Sn/Cu ~ 1.27) full surface coverage is achieved at theoretical value of 0.79 ML of Sn. As shown in chapter 3 the first monolayer coverage of Sn atoms on the Cu(100) crystal surface form a substitutional alloy with the top layer of Cu atoms. Between Phase III (0.5ML) and Phase IV (0.625ML) the formation of a second layer of Sn atoms on the crystal surface occurs. These Sn atoms in the outermost layer have a different bonding configuration to those in the initial monolayer and as a result the charge state of these Sn atoms could be different to those in the initial layer. An additional component is

evident in the photoemission spectra of the Sn 4d core level recorded at higher Sn coverage. Figure 4.4 shows normalised scans of the Sn 4d peaks taken at hν = 85 eV. The Sn 4d peaks were also measured at hν = 50 eV and produced similar results. The first three phases (Phases I-IIH) can all be fitted using a single spin-orbit split peak. These phases consist of a single species of Sn atom although the coordination of the Sn atoms changes for each reconstruction, and therefore a single component would be expected, as observed. The photoemission spectra for Phase III are measured at a Sn coverage ~ 0.52 ± 0.02 ML, slightly above the value of 0.50 ML coverage expected for the formation of a perfect Phase III surface, In these spectra a second peak is required in order to obtain a consistent fit to the measured spectra. Phase IV and the two thick layers, T1 and T2 consist of two layers of Sn atoms deposited on the Cu(100) crystal surface and are fitted with two spin-orbit split peaks.

The initial layer of Sn atoms produces a Sn 4d peak with a binding energy E_B = 23.72 ± 0.07 eV. The second layer Sn atoms have a higher binding energy, E_B = 24.01 ± 0.07 eV. With increasing Sn coverage the binding energy of the initial layer of Sn atoms increases, showing there is a charge transfer from the Sn atoms to the outermost layer of Cu atoms. The binding energy of the electrons in the Sn atoms of the outermost layer are similar to the values quoted in the literature for bulk Sn, E_B = 23.9 eV [50].

The binding energy of the initial layer of Sn atoms shifts by ~ 0.125 ± 0.02 eV to a higher binding energy as the Sn coverage increases as shown in Figure 4.5.

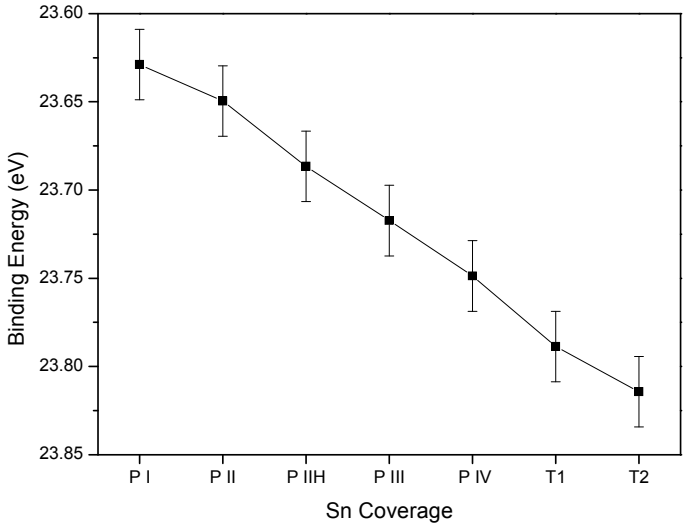

Figure 4.5: Binding energy of the initial layer of Sn atoms as function of Sn/Cu(100) surface phases.

The average spin orbit splitting between the $4d_{3/2}$ $4d_{5/2}$ orbitals is measured as 1.06 ± 0.01 eV. The branching ratio was determined as ~ 0.7 ± 0.2 at hν = 85 eV and ~ 0.59 ± 0.2 at hν = 50 eV. The theoretical value of 0.666 for the Sn 4d orbital is not expected, since relativistic effects are important for high Z atoms such as Sn. Table 4-2 shows the fitting data acquired for the Sn 4d peaks at hν = 85 eV using AAnalyzer [32].

Coverage	Peak	Peak Area	Peak Position	Line Width	Spin-Orbit Splitting	Branching Ratio
Phase I	1	921.13	23.628	0.332	1.057	0.6948
Phase II	1	1144.3	23.649	0.337	1.057	0.6969
Phase IIH	1	1409.1	23.686	0.341	1.06	0.6987
Phase III	1	1990.6	23.717	0.317	1.061	0.7028
	2	140.95	24.033			
Phase IV	1	2265.7	23.748	0.343	1.058	0.7212
	2	533.18	24.052			
Thick 1	1	2385	23.788	0.367	1.059	0.7166
	2	843.25	24.063			
Thick 2	1	2642.4	23.814	0.366	1.061	0.7219
	2	999.35	24.069			

Table 4-2: Fitting data acquired for the Sn 4d peaks at hν = 85 eV using AAnalyzer [32].

Figure 4.6 shows normalised scans of the Sn 4d peaks taken at hν = 50 after successive anneals of the sample at temperatures of 420K, 470K and 520K for 5 minutes each. Figure 4.7(a) shows the decreasing area of the Sn 4d peak after each anneal. This is consistent with Martinez-Blanco *et al.* [8], work on the temperature stability range for the Sn/Cu(100) submonolayer surface alloy system. They found that coverages in excess of 0.5ML did not exhibit temperature induced reversible phase transitions. When the Sn/Cu(100) Phase IV (0.625 ML) c(4 × 4) surface was heated to > 360 K and cooled the surface structure reverted to the (3√2 × √2)R45º pattern of Phase III. Thus suggesting that Sn atoms in excess of 0.5 ML have a lower desorption or interdiffusion temperature.

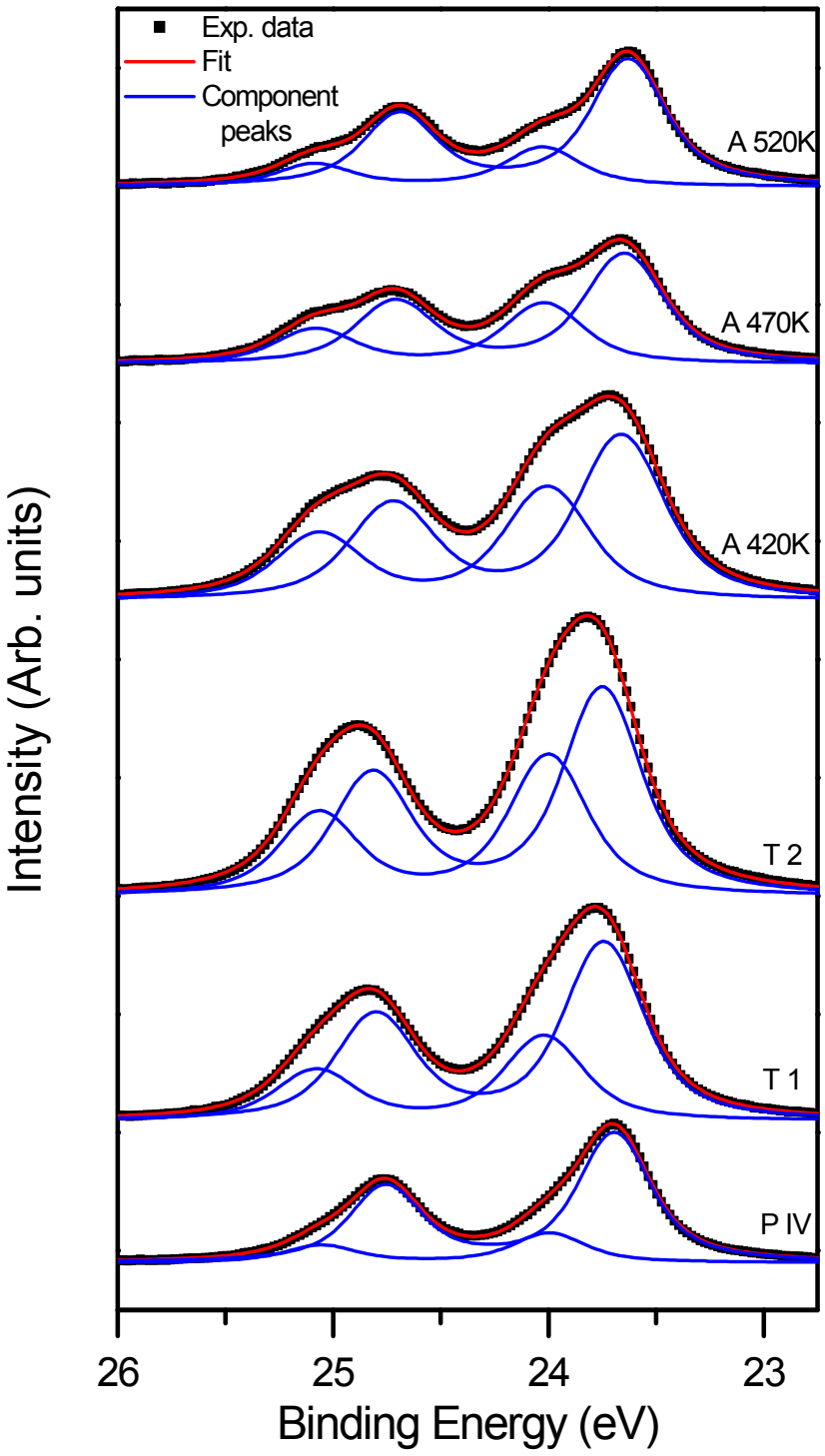

Figure 4.6: Stacked Sn 4d peaks (hν = 50 eV) showing the effects of successive anneals of the sample at 420K, 470 K and 520K for five minutes each. A Shirley type background has been removed from all spectra.

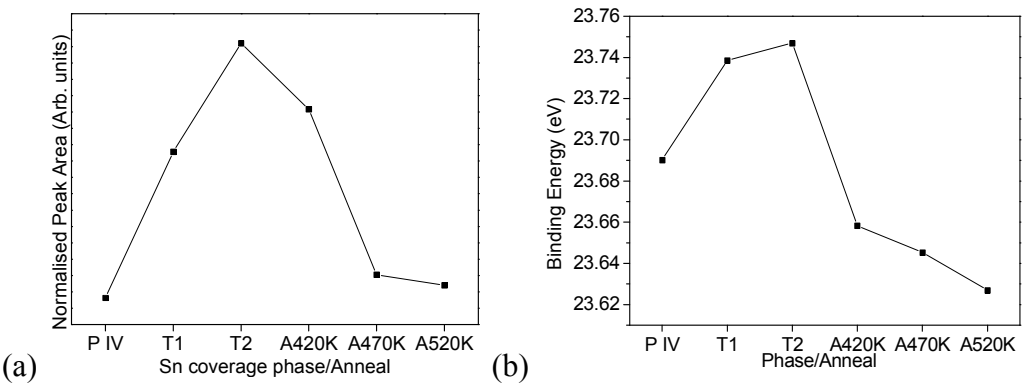

***Figure 4.7*:** (a) Sn 4d peak area and (b) Sn 4d binding energy at hν = 50 eV after successive anneals of the sample at temperatures of 420K, 470K and 520K for 5 minutes each.

Figure 4.7(b) shows the decrease in binding energy of the initial layer of Sn atoms after annealing the sample. Table 4-3 shows the fitting data acquired for the Sn 4d peaks at hν = 50 eV using AAnalyzer [32].

Coverage	Peak	Peak Area	Peak Position	Line Width	Spin-Orbit Splitting	Branching Ratio
Phase IV	1	946.17	23.690	0.352	1.062	0.5808
	2	217.25	23.987			
T1	1	1386.5	23.738	0.379	1.06	0.5874
	2	670.37	24.013			
T2	1	1619.6	23.746	0.378	1.067	0.5854
	2	1100.2	23.996			
A420K	1	1373.1	23.658	0.409	1.062	0.5809
	2	943.76	24.001			
A470K	1	839.86	23.64	0.376	1.063	0.5665
	2	464.77	24.018			
A520K	1	948.34	23.627	0.364	1.061	0.5664
	2	293.02	24.023			

Table 4-3: Fitting data acquired for the Sn 4d peaks at hν = 50 eV using AAnalyzer [32].

4.3.3 Valence Band Photoemission Analysis

Figure 4.8 shows the valence bands for all the phases of the Sn/Cu(100) submonolayer surface alloy system taken at hν = 35 eV and hν = 50eV. The large peak at ~3 eV binding energy is due to photoemission from the Cu 3d orbital. The Cu signal is shown to be attenuated considerably when the Sn coverage reaches approximately 1.0ML. This is consistent with other work on Cu(100) by Onsgaard *et al.* [51] which shows the Cu substrate signal being considerably attenuated by coverage of 0.48 ML of potassium. Valence band scans were taken for binding energies between 0 and 11eV however the energy scales on all graphs have been shortened since no features were found between BE = 6.5 eV and 11 eV.

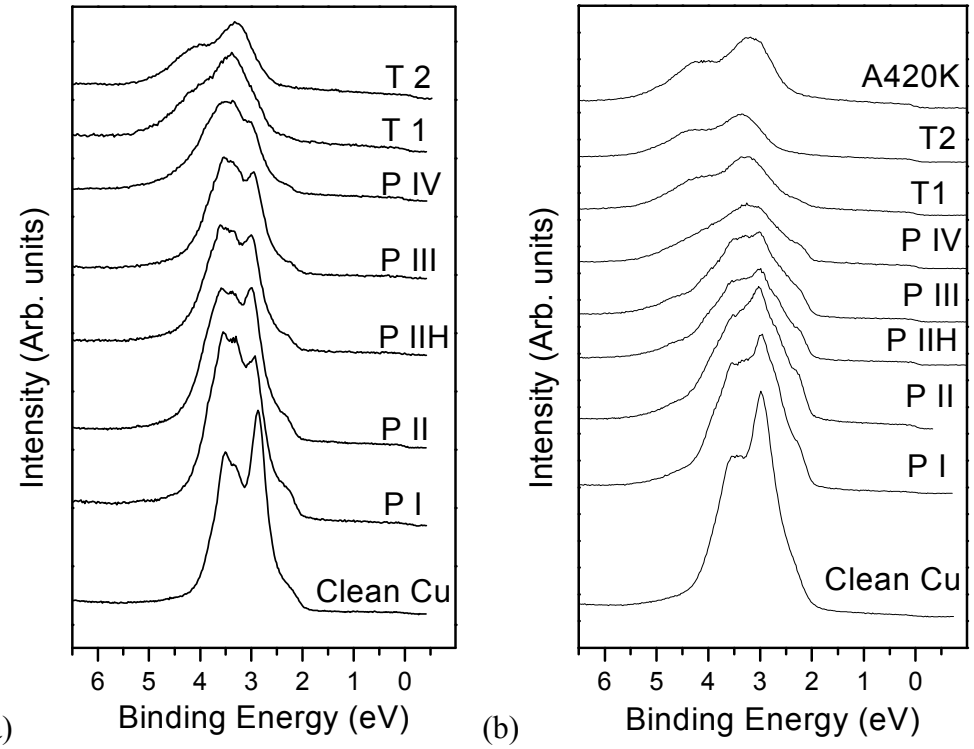

Figure 4.8: Valence band spectra taken at (a) 35 eV and (b) 50 eV for the Sn/Cu(100) system.

4.3.4 Work Function Analysis

The evolution of the work function for increasing Sn coverages is shown in Figure 4.9. The work function of the surface is shown to decrease with increasing Sn coverage.

The work function of the sample surface decreases by ~ 0.125 ± 0.02 eV which is equal to the shift in binding energy of the Sn 4d peaks observed in the spectra

presented in section 4.3.2. After annealing the sample at 420K for 5 minutes the work function increases and returns to the value observed for the Phase III structure. This is consistent with the LEED observations of Martinez-Blanco *et al.* [8]

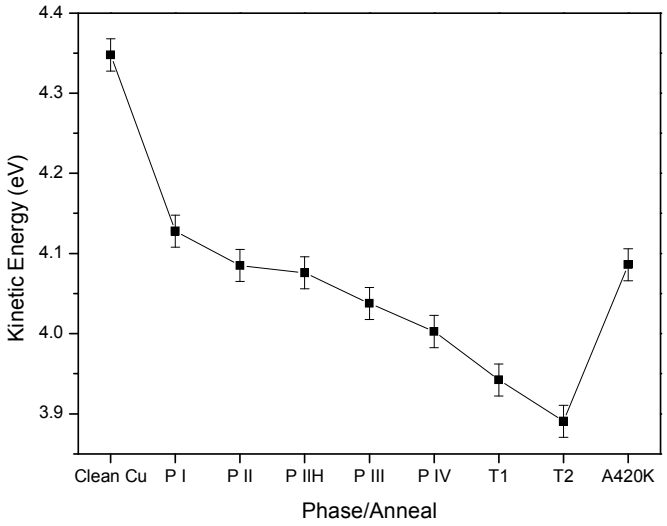

Figure 4.9: Work function as a function of the Sn/Cu(100) surface phases.

Chapter 5: Conclusions and Future Work

This thesis presents a detailed investigation of the five submonolayer surface phases of the Sn/Cu(100) surface system using I(V) LEED, STM and photoemission techniques. Four surface phases were originally reported by Argile and Rhead [6] in the early 1980's and a fifth phase was reported by Martinez-Blanco *et al.* [8] in 2006. This thesis has been motivated by this recent report of a fifth submonolayer phase of the Sn/Cu(100) surface system.

The purpose of this work was to investigate the structure of the new surface using the I(V) LEED, LEED images, STM and PES techniques. The four Sn/Cu(100) surface phases originally reported by Argile and Rhead [6] and studied using AES, I(V) LEED and LEED patterns by McLoughlin *et al.* [7] have been have been reviewed and complimented by the further studies in this thesis. The most recently reported phase is studied for the first time using the above experimental techniques.

In chapter 2 the different experimental techniques, specifically LEED, STM and PES, and their theoretical bases were presented. The equipment associated with the different techniques and the operating procedures involved are discussed in detail.

In chapter 3 results of the detailed studies of the five submonolayer phases of the Sn/Cu(100) surface system using I(V) LEED, LEED pattern and STM were presented. The relevant previous studies of each surface phase are reviewed, including recent publications by Yuki Nara et al. [46] and Lallo et al. [9]. It is noted that these STM studies were published after the detailed STM investigation presented in this thesis were concluded.

Structural models were proposed for each phase from the results the investigations presented. It is concluded that Phase I, Phase II, Phase IIH and Phase III all form surface alloys while Phase IV is best described by an overlayer model. In most cases STM images do not differentiate between surface alloy formation and overlayer structures. Only the position of the atoms and the surface symmetry is evident from STM study. Evidence of stress relief mechanisms in the Cu(100) surface due to the larger atomic radii of the Sn atoms compared to the Cu atoms (Sn/Cu = 1.27) may indicate alloy formation rather than overlayer. In Phase I the stress relief is shown in the Cu domain walls between the Sn p(2 × 2) domains. Small lateral and vertical displacements of the Cu atoms in the domain wall boundaries are measured. In Phases II

and IIH small islands form on the surface of the crystal. Cu atoms displaced by Sn atoms diffuse across the crystal surface to form islands. In Phase III every third row of Cu atoms is displaced by Sn atoms. These displaced Cu atoms from large well-ordered islands across the sample surface and each island is covered by a single domain of Phase III formation. Phase IV forms an overlayer structure with four atoms occupying the first layer and a single Sn atom forming the second layer per unit cell.

In chapter 4 synchrotron radiation based photoemission spectroscopy was used to examine the Cu 3p and Sn 4d core levels as a function of the different phases. Valence band spectra of each phase were compared at photon energies between 30 and 150 eV. The work function of the sample surface was measured for each phase and was found to be consistent with shifts observed in the Sn 4d core level peaks.

Scanning tunnelling spectroscopy (STS) was used to probe the local density of states (LDOS) of the five submonolayer phases of Sn/Cu(100). The height of the STM tip above the sample surface is maintained and a small, high frequency sinusoidal modulation voltage is superimposed on the d.c. tip-sample bias. The a.c. component of the tunneling current is recorded using a lock-in amplifier (LIA), and the component in-phase with the tip-sample bias modulation is measured. This work is not shown in this thesis due to difficulties achieving consistent reproducible results. The inherent capacitance of the STM tip when switching the tunnelling conductance causes the overloading of the lock-in amplifier. Results in which this problem did not occur showed interesting features which would certainly merit future study.

The anomalous results in the HRCLS study of the Cu 3p peak for Phase III and the inconsistent results for the branching ratio between the Sn 4d3/2 4d5/2 orbitals also merit future study. Finally it would also be interesting to calculate energy band structures for all five phases as these would assist with the interpretation of the valence band spectra.

References

1 K. Kishi, A. Oka, N. Takagi, M. Nishijima, T. Aruga. Surf. Sci. vol. 460, p. 264–276, 2000.

2 J. E. Garces, H. O. Mosca, G. H. Bozzolo. Surf. Sci. vol. 459, p. 365–389, 2000.

3 J. Tersoff, Phys. Rev. Lett., vol. 74, p. 434, 1995.

4 J. A. Venables, Surf. Sci., vol. 299/300, p. 798, 1994.

5 E. McLoughlin, “Structural investigations of metal and semiconductor interfaces," Ph.D. dissertation, Dublin City University, 2000

6 C. Argile and G. E. Rhead, Thin Solid Films, vol. 87, p. 265, 1982.

7 E. McLoughlin, A. A. Cafolla, E. AlShamaileh, and C. J. Barnes. Surf. Sci., vol. 482-485, pp. 1431-1439, 2001.

8 J. Martinez-Blanco, V. Joco, P. Segovia, T. Balasubramanian and E.G. Michel. App. Surf. Sci., vol. 252, pp. 5331-5334, 2006.

9 J. Lallo, L. V. Goncharova, B. J. Hinch, S. Rangan, R. A. Bartynski, D. R. Strongin. Surf. Sci., vol. 602, pp. 2348–2357, 2008.

10 A. Zangwill, *Physics at Surfaces*, Cambridge University Press, 1996

11 C. Davidson and L.H. Germer. Phys. Rev. B, vol. 30, p. 705, 1927

12 J.C. Vickerman (Editor), *Surface Analysis – The Principle Techniques*, J. Wiley and Sons, 1998

13 L. J. Clarke, Surface *Crystallography, An Introduction to Low Energy Electron Diffraction*. Wiley, 1985.

14 M. A. V. Hove, W. H.Weinberg, and C. M. Chan, *Low-Energy Electron Diffraction*. Springer Verlag Berlin Heidelberg, 1986.

15 Omicron NanoTechnology GmbH, Users manual, 2002 [Online]. Available: http://omicron.de

16 M. F. Opheys, EE2000, Softwareentwicklung fùr Wissenschaft und Industrie. 2004

17 K. Hermann and M. A. Van Hove, LEEDpat Version 2.1 2006 [Online]. Available: http://electtron.lbl.gov/software/intsoftware.html

18 G. Binnig, H. Rohrer, Ch. Gerber, E. Weidel, Phys. Rev. Lett. Vol. 49, p. 57, 1982

19 G. Binnig, H. Rohrer, Helv. Phys. Acta., vol. 55, p. 726, 1982.

20 G. Binnig, H. Rohrer, C. Gerber and E. Weibel, Appl. Phys. Lett., vol. 40, p. 178, 1982.

21 H. C. O'Hanian, *Modern Physics*, Second Edition, Prentice Hall International, 1987

22 A. Rae, *Quantum Mechanics*, Third Edition. Institute of Physics Publishing, 1992.

23 R. Wiesendanger, *Scanning Probe Microscopy and Spectroscopy Methods and Applications*. Cambridge University Press, 1998.

24 J. Tersoff and D. R. Hamann, Phys. Rev. Lett., vol. 50, p. 1998, 1983.

25 J. Tersoff and D. R. Hamann, Phys. Rev. B., vol. 31, p. 805, 1985.

26 W. A. Hofer, Prog. Surf. Sci., vol. 71, p. 147, 2003.

27 Nanotec Electronica, 2008. [Online]. Available: http//www.nanotec.es

28 K. Siegbahn, Science, vol. 217, (1982), p. 111-121.

29 D. Briggs, M. P. Seah, *Practical Surface Analysis by Auger and X-ray Photoelectron Spectroscopy*, John Wiley & Sons, 1983.

30 S. Doniach and M. Sunjic, J.Phys. C., vol. 3, p. 285, 1970

31 B.H Armstrong. J. Quant. Spectrosc. and Radiat. Transfer., vol. 7, p 61-88, 1967

32 A Analyzer ver. 1.02, Centro de Investigación y de Estudios Avanzados, Cinvestav Querétaro. Mexico. 2002. [Online] http://www.qro.cinvestav.mx/~aanalyzer/

33 W inSpec ver. 2.08, Laboratoire Interdisciplineaire de Spectroscopie Electronique, Facultes Universitaires Notre-Dame de la Paris, Belgium, 1999.

34 R. G. Egdell, J. Rebane, T. J. Walker, D. S. L. Law. Phy Rev B, vol. **59** (3), p. 1792-1799, 1999

35 K. Horn, F. H. Frank, J.A. Wilder, Phys. Rev. Lett., vol. 57, p. 1064, 1986.

36 Institute for Storage Ring Facilities in Aarhus (ISA), Aarhus Storage Ring In Denmark (ASTRID), http://www.isa.au.dk/astrid/astrid.html

37 F. Jona, R. Mayer, C.S. Zhang. K.G. Lynn, W.E. Frieze and P.M. Marcus. Phys. Rev. B 35, 3102 (1987).

38 P. J. Jennings, S. M. Thurgate. Surf. Sci.Vol. 104, pp. L210-L212 1981.

39 H. L. Davis, J. R. Noonan. Surf. Sci., vol. 115, p. L75-80, 1982

40 A.A. Cafolla, E. McLoughlin, E. AlShamaileh, Ph. Guaino,G. Sheerin, D. Carty, T. McEvoy, C. Barnes, V. Dhanak and A. Santoni. Surf. Sci., vol. 544, p.121-133, 2003.

41 F. Besenbacher. Rep. Prog. Phys., vol. 59, p. 1737, 1996.

42 G. E. Rhead, C. Argile, and M. G. Barthes. Surf. Interf. Anal., vol. 3, p. 165, 1981.

43 D. Ghaleb and B. Perraillon. Surf. Sci, vol. 162, p. 103, 1985.

44 K. Pussi, 2004. Private communication.

45 G. Sheerin, “Ordering of Organic Molecules on Templated Surfaces," Ph.D. dissertation, Dublin City University, 2006.

46 Yuki Nara, Koichiro Yaji, Takushi Iimori, Kan Nakatsuji and Fumio Komori. Surf. Sci., vol. 601, pp. 5170-5172, 2007.

47 K. Pussi, E. McLoughlin, E. AlShamaileh, A. A. Cafolla, and M. Lindroos. Surf. Sci., vol. 549, pp. 24{30, 2004.

48 M. A. Hove, W. Mortiz, H. Over, P. J. Rous, A. Wander, A. Barbieri, N. Materer, U. Starke, and G. A. Somorjai. Surf. Sci. Rep., vol. 19, p. 191, 1993.

49 P.S. Bagus, G.Pacchioni, F. Parmigiani. Phys. Rev. B. vol. 43, p. 5172-5175, 1991.

50 J. C. Fuggle and N. Martensson. J.Elect. Spec. Relat. Phenom. 21, 275, 1980.

51 J. Onsgaard, L Thomsen, S. V. Hoffmann, P. J. Godowski. Vac., vol. 81, p. 25-31. 2006